ABSTRACT

PEGAHAN, SAEED. Many-body Physics in a Weakly Interacting Fermi Gas. (Under the direction of John Thomas).

This dissertation presents a rigorous study of a very weakly interacting degenerate cloud of ^{6}Li, confined in a spin-dependent harmonic potential. We measure complex, time-dependent spin-density profiles, varying on length scales much smaller than the cloud size, and show that a one-dimensional mean-field model, without additional simplifying approximations, quantitatively predicts the observed spatial fine structure. The measurements provide a precise quantitative test of the underlying energy-space spin lattice model and energy-dependent long-range couplings. We measure the magnetic fields where the scattering lengths vanish for three different hyperfine state mixtures to provide constraints on the collisional (Feshbach) resonance parameters.

In addition to investigating the collective spin evolution of a many-body system, weakly interacting Fermi gases offer a rich platform for investigating information spreading and spin coherence in a large many-body quantum system. We show that inverse Abel-transformation of the spin density profiles determines the collective spin vector as a function of energy, enabling general energy-space resolved protocols. For an application, we measure out-of-time-order correlation functions in different energy sectors to reveal the energy dependence of the many-body coherence. The observation justifies the existence of the higher-order coherence and out-of-time order correlation functions at the microscopic level hidden in macroscopic measurements.

Many-body Physics in a Weakly Interacting Fermi Gas

by
Saeed Pegahan

A dissertation submitted to the Graduate Faculty of
North Carolina State University
in partial fulfillment of the
requirements for the Degree of
Doctor of Philosophy

Physics

Raleigh, North Carolina

2020

APPROVED BY:

Alexander Kemper	Keith Weninger
Lubos Mitas	John Thomas Chair of Advisory Committee

DEDICATION

For Rebeca and Jasper

BIOGRAPHY

Saeed Pegahan was born on January 19, 1989, in Isfahan, Iran. He grew up in Isfahan and graduated from Norouzi High School in 2006. In 2007, he majored in physics at the University of Isfahan, Iran. He graduated with his B.Sc. with honors in Fall 2011. He obtained his first Master's degree with a minor in atomic physics at the University of Isfahan and graduated in 2013. For the second Master's, he focused on quantum error prevention and leakage elimination for semiconductor quantum dots at Southern Illinois University, Carbondale, and graduating in 2015. After joining John Thomas research group in August 2015, he got involved in different experiments on degenerate weakly interacting quantum gases. His research at NC State University focused on engineering energy-space lattice for collective quantum dynamics and investigating information scrambling in many-body systems. He received the Sigma XI Research award at NC State and the 5-Sigma Physicist award from the American Physical Society. He earned his Ph.D. in December 2020.

ACKNOWLEDGEMENTS

Looking back in time, I feel truly blessed for having been surrounded by people who always believed in me and encouraged me to follow my passion and interests in life. Without the support and help of my parents, I could never make it this far. I will always be thankful for the time and effort my mom made to nurture my curiosity. I'm also thankful for my dad's continual support and encouragement to follow my passion and achieve my goals. I want to acknowledge my older sister for all of her support all these years that I have been studying abroad, and I am looking forward to the day that I see you and my grown up nephew again.

I am also grateful to my science middle school teachers, Rahmani and Mozaffari, who discovered my interest in science at early years. In addition, thank you to my high school physics teacher, Nourozi, who through his lectures on optical science to thermodynamics, motivated me to choose physics as a field of study.

I want to thank my undergraduate advisor S. Javad Akhtarshenas and my Master's mentor Morteza Soltani who guided me on my first research project in atomic physics. I will never forget your support and mentorship throughout my bachelor's and Master's studies.

I am forever indebted to my Ph.D. advisor, John Thomas; without a doubt, I am a better researcher now because of him. Your passion for physics and constant guidance inspired me to give my best every day. And even through difficulties due to the Covid-19 pandemic, he lifted our group's spirit and encouraged us to keep going. Without his dedication and constant feedback, this dissertation would not have been possible. His kind, caring nature and down-to-earth attitude made my life as a Ph.D. student a delightful one. John, I have been lucky to be part of your group and I am forever grateful for your dedication and commitment to my success.

Next, I want to express my gratitude to our postdoc Ilya. His knowledge about every optical element in the lab always fascinated me. Ilya, I consider myself very fortunate to have worked with you; I appreciate all the insight you gave me on technical issues and research in general. I want to thank Stetson, our previous postdoc. Even though we did not work in the same laboratory, I enjoyed our conversations from atomic noise to Bourbon beers. I also want to acknowledge Lorin (Ric). I enjoyed working right next to you in the office, sharing different lab equipment, and learning how to make banana bread and Apple Pie. I want to acknowledge Xin with his unpretentious personality and calmness.

I want to thank my senior student Kan for training me to get familiar with the atom cooling system and for his willingness to discuss at a time when he was very busy. I am happy that I could work shoulder-to-shoulder with him and collaborate on different projects. I admire his work ethic and enthusiasm in the lab and talking about our favorite scenes in Breaking-Bad.

My special thanks to the graduate program coordinator, Rhonda, for her promptness and discipline in caring so much about graduate students and finding answers to our questions.

I want to thank my girlfriend, Rebeca. Without you, I do not think I could have come this far. Being both Ph.D. students, we faced many challenges, but you always had my back. I am grateful that we got to share this journey together. Thank you for your patience and sacrifices.

Lastly, I want to thank Jasper, my Border collie. You have brought so much joy to my life over the past three years. I do not know how I would go through the stressful days without your companionship.

A debt of gratitude is owed to Alexander (Lex) Kemper, Lubos Mitas, Keith Weninger, and Jaime Collazo for graciously serving on my dissertation committee.

TABLE OF CONTENTS

LIST OF FIGURES

LIST OF TABLES

Chapter 1

Introduction

Degenerate Fermi gases are ideal systems for studying many-body phenomena that can sometimes be challenging, if not impossible, to access experimentally in solid-state systems. Through controllable atomic interaction strength, atoms densities, and geometry of the trapped atomic gas, ultracold Fermi gases not only provide an excellent choice to strongly interacting systems [O'Hara et al., 2002, Zwierlein et al., 2005] but also opportunities to study weakly interacting many-body systems for quantum simulation and quantum information applications [Bloch, 2012, Du et al., 2009, Pegahan et al., 2019].

Weakly interacting degenerate Fermi gases offer a pristine testbed for simulating various phenomena ranging from out-of-equilibrium spin-lattice dynamics [Eisert et al., 2015, Koller et al., 2016] to spin segregation [Du et al., 2008, Lewandowski et al., 2002, Pegahan et al., 2019] and information scrambling (spreading) in a large quantum gas containing 10^5 neutral atoms [Gärttner et al., 2018, Gärttner et al., 2017, Landsman et al., 2019, Pegahan et al., 2020]. Before elaborating more on these concepts, I want to remind the reader about some of a cold Fermi gas's properties, which makes their system a rich candidate to probe weakly interacting regimes. First, an ultra-cold Fermi gas is composed of fermions, which must have a total wave function that is anti-symmetric. Second, due to the extremely low kinetic energy of the colliding atoms in the ultracold gas, the dominant quantum scattering process is the s-wave, where the orbital angular momentum is ($l = 0$), s-wave. Thus atoms with opposite spin can have the s-wave interaction, which is not Paul blocked, as their spin-wave function is anti-symmetric.

Since we are working in a low energy limit, two atoms collisions can be simplified further by the low energy limit assumption. In a sample of ^{6}Li in our laboratory, the two-body s-wave collision cross section is specified by a single parameter known as the scattering length. By tuning a bias magnetic field in our laboratory, the s-wave scattering length of the colliding atoms can be adjusted to nearly vanish with $a = 0$ where we can study a collisionless regimes. If we consider scattering length to be $a = 4.24\ a_0$, the corresponding classical collision rate

[Gehm et al., 2003] (without Pauli blocking) is,

$$\gamma_c = \frac{N_{\downarrow} m_{^6Li}(\omega_{\perp}^2 \omega_x) 4\pi a_s^2}{4\pi^2 k_B T_F} \simeq 0.002. \tag{1.1}$$

Thus, the single particle energy of the system at this scattering length is conserved. Since s-wave scattering in Fermi gases is allowed only for antisymmetric spin states, two-component clouds exhibit an effective exchange interaction. From first order perturbation theory, one can model the interaction as an effective contact potential,

$$V(\vec{r} - \vec{r}') = \frac{4\pi\hbar^2 a}{m} \delta(\vec{r} - \vec{r}') \tag{1.2}$$

where $\vec{r}$ and $\vec{r}'$ specify the location of the two atoms and m is the mass of the atom. Note that for attractive interactions $a < 0$ whereas for repulsive interactions $a > 0$.

To show the ultracold atom properties more quantitatively, the range of the interatomic potential between colliding ^{6}Li atoms is roughly $r_0 \approx 20$ Bohr $\approx 1\ nm$, and the temperature of the gas is on the order of 1 μK corresponding to a thermal de Broglie wavelength of approximately $\lambda_T = 700$ nm. The wavelength is significantly larger than the range of the potential, so that if we quantize the angular momentum l of the gas via the relation $l\hbar = r_0 p = r_0(h/\lambda_T)$, then l is given by:

$$l = \frac{2\pi r}{\lambda_T} \approx 0.001 \tag{1.3}$$

Thus, the only relevant value for l is zero for scattering processes of ultracold Fermi gases.

Weakly interacting two-component Fermi gases [Du et al., 2009], with tunable, nearly vanishing s-wave scattering lengths a [Pegahan et al., 2019], offer a pristine platform for exploring the interplay between spin, motion, and statistics in many-body systems. As shown in Eq. 1.1, the atomic collision rate $\propto |a|^2$ is negligible, so that single atom energies are conserved over the evolution time scale set by the mean-field frequency $\propto |a|$, see Ch. 3. In this system, the conserved single-particle energies label the “sites” of an effective energy-space lattice. Throughout this dissertation, we will denote lattice “sites” with Roman letters n, representing the trap mode index, unless otherwise stated.

1.0.1 Lattice in an Energy Space

As I mentioned earlier, ultra-cold quantum gases provide a unique platform to simulate lattice structure using counter-propagating beams [Köhl et al., 2005]. While optical lattices are perfect candidates to study fundamental physics, their implementation in a many-body system impose different challenges. For example, the optical lattice’s periodicity is limited by the wavelength of the laser or the relative angle between the laser beams. In contrast to optical lattices in

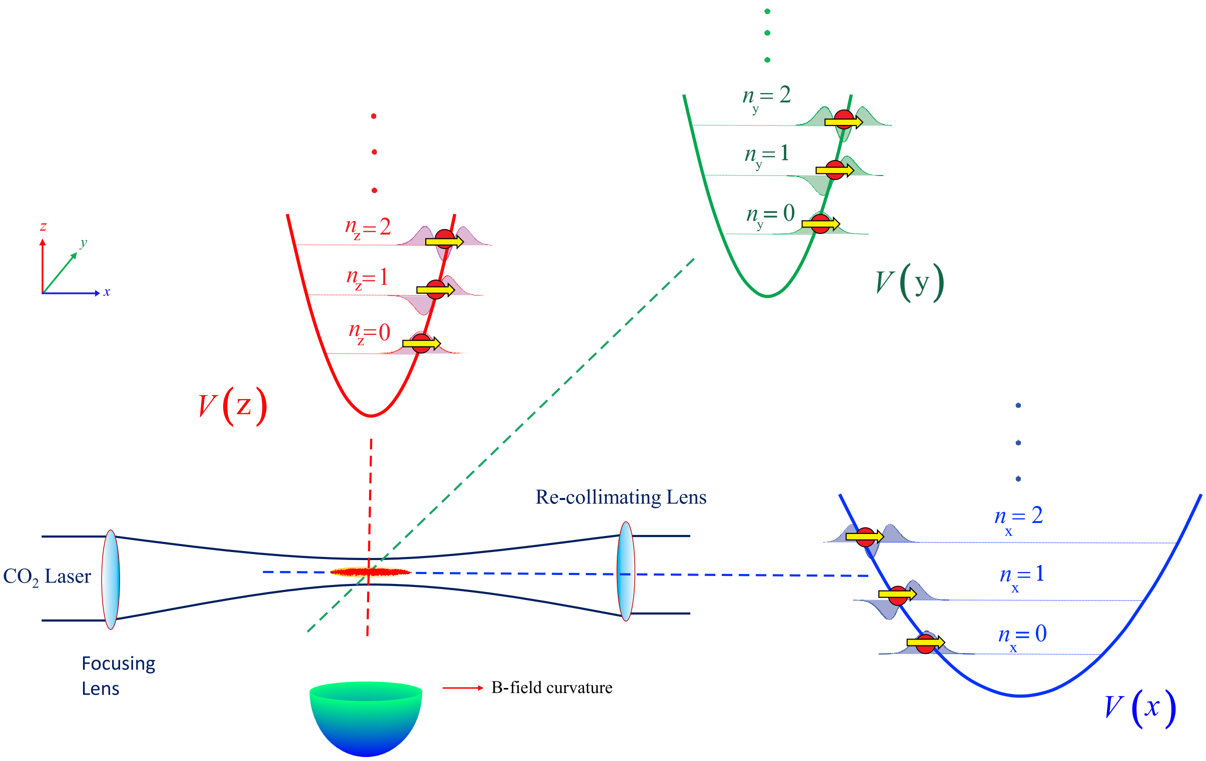

Figure 1.1: Harmonic cigar-shaped optical dipole trap in the presence of a magnetic field gradient. Trapped atoms in the dipole trap oscillate with a frequency of 23 Hz along the cigar x-axis and 27 times faster, with a frequency of 625 Hz, along the transverse directions y, z. In the weakly interacting regime, the single atoms energies, $E_i = (n_i + 1/2)h\nu_i$, are conserved, forming a 3-dimensional spin-lattice, Fig. 1.2 in an energy space.

real space, engineered energy-space lattice, with controlled energy landscapes and site-to-site interactions, offer broad prospects for simulating quantum systems, without limiting to any optical lattice geometry.

Weakly interacting spin states of ^{6}Li Fermi gases, in the presence of magnetic field curvature, shown in Fig. 1.1, offer an outstanding opportunity to investigate the emergence of an effective spin-lattice in energy space. In this type of lattice, we are working in a collisionless regime, and the energy of particles is conserved, as are the harmonic oscillator quantum numbers, shown in Fig. 1.1. Thus, we can use the particles with an energy E_i, to label lattice site ith in the energy space, providing a precise quantitative test of the underlying spin lattice model with energy-dependent long-range, $\propto 1/\sqrt{E_i - E'_j}$ couplings between different "sites", Ch. 3. For the degenerate Fermi gas that we work with as $k_BT_F/h\omega_x = n_x \simeq 650$, the average number of atoms at each site is $N/650 = 100$.

The effect of this long-range coupling between atoms in energy space, which is a result of vibration motion of atoms in the harmonic trap with opposite spins, for the first time was observed in spin-segregation of thermal (Boltzmann) gas of ^{6}Li [Du et al., 2008]. However, the initial implementation of the energy-dependent collective spin-rotation model [Du et al., 2009] yielded only semiquantitative agreement with the observed spin-density profiles, which were measured at high temperatures, suggesting that the model was incomplete.

The key idea in our approach, whose validity we investigate in detail in Ch. 3, is that the single-particle motional states are not changed by interactions, but the long-range spin interaction, shown with green arrows in Fig. 1.2, can influence the spin dynamics. As I mentioned above, in this picture, the single-particle energies are suitable for exploring a wide variety of spin-lattice models that are difficult to realize using optical lattice techniques. We use a mean-field treatment to describe the collective spin dynamics due to long-range spin coupling, and for that, we assume there is no coherence between spins with a different energy.

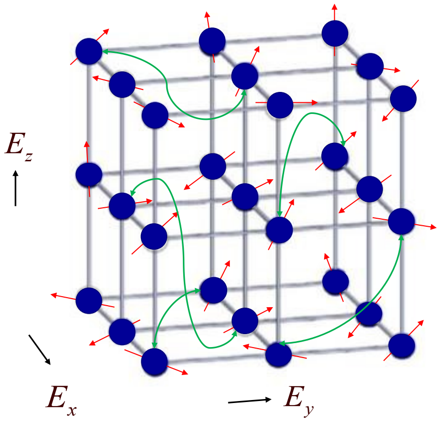

Figure 1.2: Simulating a many-body system in an energy-space lattice. Each site in the energy space experiences a local magnetic field that causes long-range spin exchange, illustrated by the green arrows, between different sites.

In the weakly inteacting Fermi gas that we study, the magnetic field gradient effect on the atoms is negligible for the tightly confined radial directions of the trap; therefore, by integrating over the transverse spin interactions, we can transform the energy lattice from three dimensional to a one-dimensional energy lattice, depicted in Fig 1.3. Further, using the one-dimensional energy-space lattice, we can access energy-resolved measurements for collective spins and study correlations between spin vectors in different energy-space sectors.

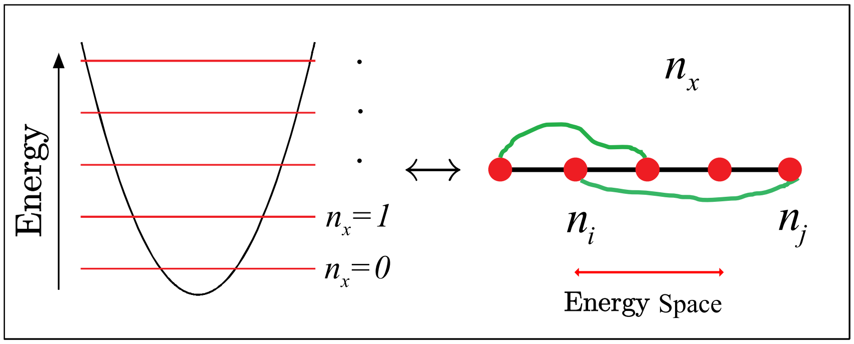

Figure 1.3: 1-Dimensional energy Lattice. The green lines shows the long range interaction between spins in the "lattice" site in energy space, where scale with $1/\sqrt{n_i - n_j}$.

In the next section, I will discuss how these measurements motivate new cold atom approaches to measure information scrambling in spin-lattice systems.

1.1 Significance of the Current Work

This dissertation describes experimental observations of collective dynamics for trapped, weakly interacting Fermi gases in of two hyperfine states. These observations provide a new paradigm for studying the many-body physics in a large quantum system containing N $\sim 10^5$ atoms with a tunable s-wave scattering, reversible Hamiltonian, and energy-resolved spin density measurement. This dissertation aims to thoroughly investigate collective spin dynamics and their application on spin-energy correlation and information scrambling through the following experiments.

For the first experiment, we use quantum-degenerate clouds of ^{6}Li, confined in a spin-dependent harmonic potential. Using a one-dimensional mean-field model, we provide a precise quantitative test of the underlying energy-space spin lattice model and energy-dependent long-range couplings in a system with N atoms. This study provides an essential benchmark for collective quantum dynamics and correlated spin current. For the second experiment, we exploit the weakly interacting Fermi gas to demonstrate a new protocol for the microscopic measurement of information spreading and scrambling by transforming spatial spin-densities to an energy-space lattice. The energy-resolved observations we made in the energy lattice, justifies the existence of higher-order coherence and out-of-time order correlators at the microscopic level hidden by the observation in macroscopic spin measurements.

1.1.1 Spin-Energy Correlation in a Weakly Interacting Fermi Gases

Weakly interacting two-component Fermi gases, with tunable, nearly vanishing, s-wave scattering lengths a, offer a pristine platform for exploring the interplay between spin, motion, and statistics in many-body systems [Koller et al., 2016, Pegahan et al., 2019]. In this dissertation we initially employ quantum degenerate samples, with a negligible collision rate, to minimize energy shifts of the scattering length that become significant at higher temperatures.

Because of the complexity of these phenomena, we need an approach that treats spin motion, interactions, and quantum statistics on a common footing. Through a collective mean-field model, described in Ch. 3, we explore long-range interacting systems, quantitatively describe the spin-density evolution in the collisionless regime, and precisely test the underlying energy-space spin-lattice model. In addition, we measure the magnetic fields where the scattering lengths vanishes ($a_s = 0$) for three different hyperfine state mixtures to provide constraints on the collisional (Feshbach) resonance parameters.

In general, in the mean-field collective model, the microscopic degrees of freedom in the many-body system can be ignored, and a new macroscopic parameter such as mean-field frequency emerges as the important degree of freedom for the system. The identification of this parameter can be made through experimental measurements such as s-wave scattering without knowing about the microscopic physics.

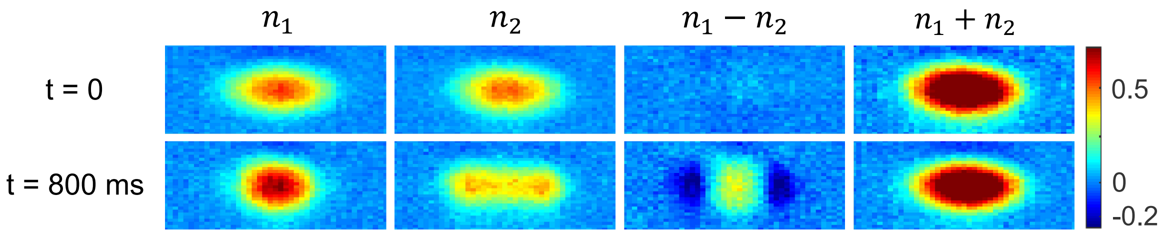

Figure 1.4: Spin-energy correlation produces spin segregation in a degenerate Fermi gas with an s-wave scattering length of 5.2 bohr. The palettes are $50 \times 950\,\mu$m. Left to right: n_1, n_2, $n_1 - n_2$, and $n_1 + n_2$ in units of $(n_1 + n_2)_{max}$ at $t = 0$ (upper) and $t = 800$ ms (lower) after coherent excitation of a $|1\rangle - |2\rangle$ superposition state. Note that $n_1 - n_2$ evolves in time while $n_1 + n_2$ remains constant, due to single particle energy conservation.

Fig. 1.4 shows spin-density evolution on the time scales set by the mean-field frequency $\Omega_{MF} \simeq 2\pi \times 1.0$ Hz. The first row of Fig. 1.4, shows the spin-density evolution for a coherent states of ^{6}Li atoms. Due to forward s-wave scattering, atoms in $|1\rangle$ state moves inward in the trap, and atoms at $|2\rangle$ state move outward. This behavior can be inverted simply by changing the sign of the s-wave scattering length from positive to negative.

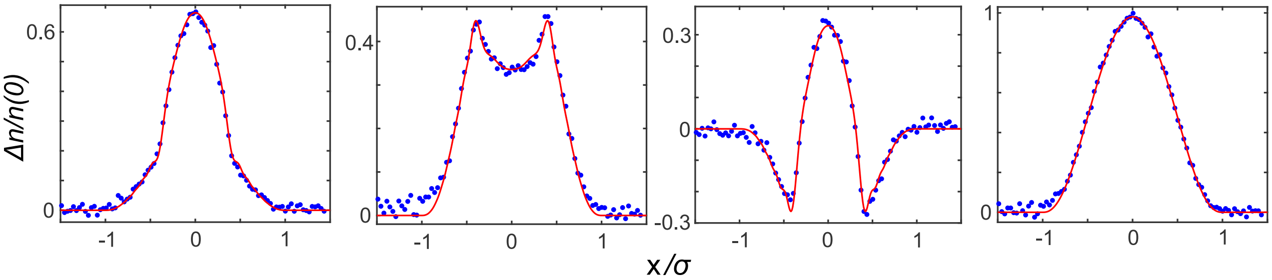

Figure 1.5: Spin-density profiles for a degenerate ($T/T_F = 0.35$) Fermi gas at $t = 800$ ms relative to coherent excitation. Data (blue dots) versus prediction (red curves) showing quantitative agreement. Left to right: n_1, n_2, $n_1 - n_2$, $n_1 + n_2$ in units of the peak total density. Each solid curve is the mean field model with a fixed scattering length of $a = 3.04$ bohr ($B = 528.147$ G) and a fitted cloud size $\sigma_{Fx} \equiv \sigma = 329\,\mu$m, obtained by fitting the total density $n_1 + n_2$ to a 1D Thomas-Fermi profile, see Eq. 3.46.

Using a mean-field model of Ch. 3, we can capture the one-dimensional spin density profile shown in Fig. 1.5. These profiles are integrated along the vertical (radial) direction of absorption images that are captured at 800 ms after coherent excitation, for a degenerate $|1\rangle - |2\rangle$ cloud with $a = 3.04\,a_0$. Note when we subtracted the first two profiles, $n_1 - n_2$ evolves in time while $n_1 + n_2$ remains constant. This justifies we are working in a collisionless regime and despite small scale spatial structure observed in the spin density $S_z(x)$, the sum of the spatial profiles for the two spin densities remains thermal (Thomas-Fermi profile).

The spin-density measurements provide an essential benchmark for future work on collective spin evolution with designer energy landscapes in the weakly interacting regime. Moreover, studying this regime paves the way for studies of beyond mean-field physics in weakly interacting gases, measurement of spatially correlated spin fluctuations [Koller et al., 2016], and measurement of correlated spin currents [Bender et al., 2019].

1.1.2 Energy-Resolved Information Scrambling

In addition to spin-energy correlation, weakly interacting Fermi gases offer a unique testbed for investigating information spreading and spin coherence in a large many-body quantum system. Here, I briefly discuss how we develop a general energy-resolved method, using an inverse able transformation of spatial spin-density profiles $\mathbf{S}(x)$, for measuring spin density $\mathbf{S}(E)$ in an energy-space lattice. For more in depth discussion, I refer a reader to Ch. 4.

The energy-dependent collective spin vector $\mathbf{S}(E)$, as shown in 1.6, is determined as the inverse-Abel transform of the measured spatial profile of the spin density $\mathbf{S}(x)$. In using this method, we assume that the measured axial spin density profiles $n_\sigma(x)$, with $\sigma = \uparrow_z, \downarrow_z$, are given in the continuum limit by,

$$n_\sigma(x) = \int dE\, |\phi_E(x)|^2\, n_\sigma(E), \tag{1.4}$$

where $\int dx\, n_\sigma(x) = \int dE\, n_\sigma(E)$ is the total number N_σ in each spin state σ. For our experimental parameters, where $E_F/h\nu_x \simeq 650$, the continuum approximation is justified. In addition to the continuum approximation, an important feature of Eq. 1.4 is the assumption that there is *neglible coherence* between single-atom energy states. This assumption is justified by the very small transition matrix elements $< 10^{-4}\,\hbar\omega_x$ between three dimensional harmonic oscillator states, which arise from short range interactions between two atoms. [Pegahan et al., 2020]

When trapped atoms interact, information stored on them gets distributed into many-body degrees of freedom. In general, this process leads to correlations in the subsystems. In the case of spin interactions, information stored (coherence) in the initial state, put in contact through s-wave interactions, is distributed over and therefore stored in local degrees of freedom of the system. As a result, if we were to look at only a local region (such as small energy regions), we would conclude that the interactions have caused initial information to be lost.

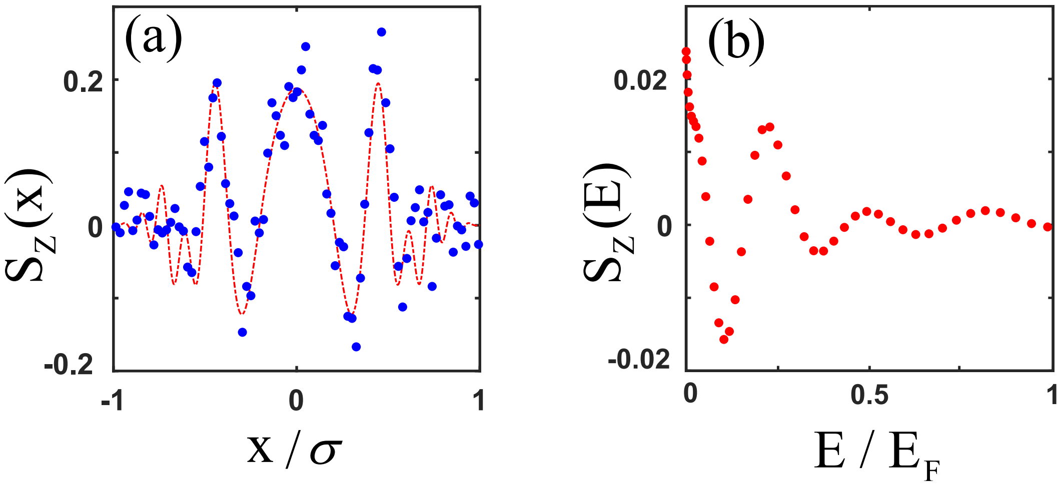

Figure 1.6: Energy-resolved out-of-time-order correlation measurement. (a) “single-shot” spin density profile $S_z(x)$ (blue dots). The red dashed curve is shown to guide the eye; (b) An inverse-Abel transform, see Ch. 4, of the spatial profile (blue dots) is used to extract the single-shot energy-resolved spin density $S_z(E)$ (red dots). The scattering length is measured at $a = 4.24\,a_0$.

Quantum information that spread between parts of a many-body system are intrinsically linked to the system’s evolution towards thermal equilibrium in a process called thermalization.

Measuring information scrambling is challenging, because of the need to resolve relevant information from the the whole system that is present, without the measurement being corrupted.

By exploiting energy-resolved measurements of the collective spin $\mathbf{S}(E)$, we extract out-of-time order correlation (OTOC) functions, Ch. 4, through a many-body pulse sequence on spins and observe OTOC functions, $\mathcal{F}(\phi)$, in energy-resolved sectors. Here, ϕ is a global rotation (perturbation) which we apply to the many-body system of spins to diagnose information scrambling in different energy partitions. The measurements of OTOC's in a spin-dependent harmonic trap, shown in the (right) Fig. 1.7, revealing complex energy-resolved OTOC structures that are hidden in measurements of the total collective spin vector, shown in the (left) Fig. 1.7.

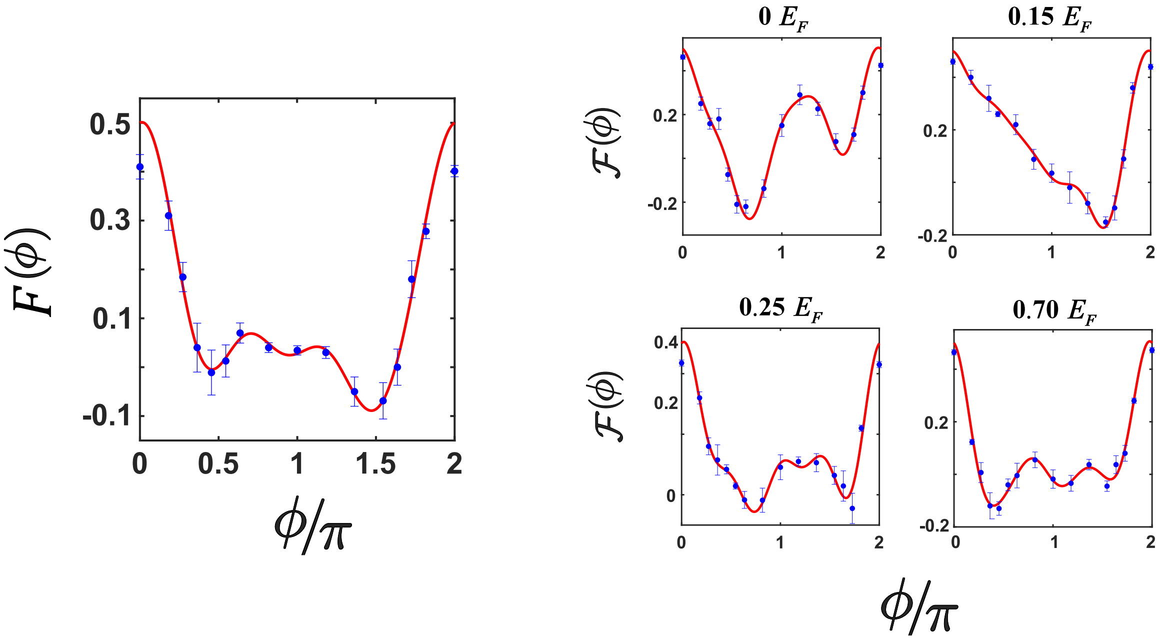

Figure 1.7: (Left) Total collective spin projection S_z versus rotation angle ϕ without energy restriction. $F(\phi) = \frac{1}{2}(N_\uparrow - N_\downarrow)/(N_\uparrow + N_\downarrow)$ (blue dots) for a scattering length $a = 4.24\,a_0$. The red curve is the fit from Eq. 6.23 to extract coherence coefficient. (Right) Energy-resolved collective spin projection $S_z(E)$ versus rotation angle ϕ for spins of selected energies (left to right) $E/E_F = 0, 0.15, 0.25, 0.5, 0.7$. Here, $\mathcal{F}(\phi) = \frac{1}{2}[n_\uparrow(E) - n_\downarrow(E)]/[n_\uparrow(E) + n_\downarrow(E)]$. The top row shows the data (blue dots) for a measured scattering length $a = 4.24\,a_0$.

1.2 Weakly-Interacting Fermi Gases

An important motivation to study the dynamics of ultracold atomic gases is their capacity to control interaction strength using Feshbach resonances and the possibility to study different interacting regimes such as strongly interacting Fermi gases. These strongly interacting Fermi gases have been extensively studied [O'Hara et al., 2002, Bloch, 2012, Zwierlein et al., 2005]. In contrast, the weakly interacting Fermi gases, which offer the necessary foundation for understanding the complex spin dynamics, induced by the interplay between spin interactions and motional effects, has received relatively little attention.

Despite the local character of the short range contact interactions in a weakly interacting system, collective and long-ranged phenomena were observed, including robust spin spatial separation of the spin densities [Du et al., 2008]. The use of AMO systems to better understand long-ranged interacting physics can boost our knowledge of fundamental quantum sciences and lead to important advances in exploring new regimes of magnetism and spintronics [Berger, 1996, Slonczewski et al., 1996].

When we decrease the s-wave scattering lengths for a Fermi cloud of ^{6}Li to nearly vanishing $a = 0$, drastic modifications of the single-particle dynamics [Du et al., 2009, Pegahan et al., 2019] are observed, as shown in a false-color Fig. 1.4. In the field of spintronics, similar phenomena give rise to spin transfer, where a spin current is used to excite or reverse a nanomagnet [Berger, 1996], a relevant concept for future magnetic memory applications.

In the case of spin-segregation, as the magnetic moments of two spin species are not identical, the finite curvature of the bias magnetic field, depicted in Fig. 1.1, introduces slightly different axial trapping frequencies between two spins, 14.7 mHz (the corresponding difference in the transverse oscillation frequencies in the optical trap is negligible, due to the tight transverse confinement). This small difference correlates the precession of an atomic spin in the horizontal axial plane with the energy of the atom, giving rise to a spin-wave, as illustrated in Fig. 1.4.

By subtracting the two spin densities at different times, we can see a distinct pattern known as spin segregation. However, when we add spin densities of two spins, the results are identical, shown in the last column in Fig. 1.4. This suggests that a total spin density remains thermal with the Thomas Fermi spatial distribution, shown in Fig. 1.8. The Fermi energy for a noninteracting Fermi gas confined in a harmonic trap with N particles per spin state is,

$$E_F = \hbar(6N\bar{\omega})^{1/3}. \tag{1.5}$$

The Fermi energy sets a characteristic energy scale which is of great importance when discussing both interacting and noninteracting Fermi gases. To provide the reader with a sense of energy, temperature and length scales of the experiment, we find a Fermi energy (Eq. 1.5) of

$k_B \times 0.73\,\mu$K and extract the corresponding Fermi radius(red fit in Fig. 1.8) for the x-direction by $\sigma_{Fx} = \sqrt{2k_BT_F/m}/(2\pi\nu_x) = 310\,\mu$m. As shown in Fig. 1.8, we fit a total spin density $n_{\uparrow_z}(x) + n_{\downarrow_z}(x)$ with a finite temperature Thomas-Fermi profile which yields $T/T_F = 0.32$ for the degenerate sample.

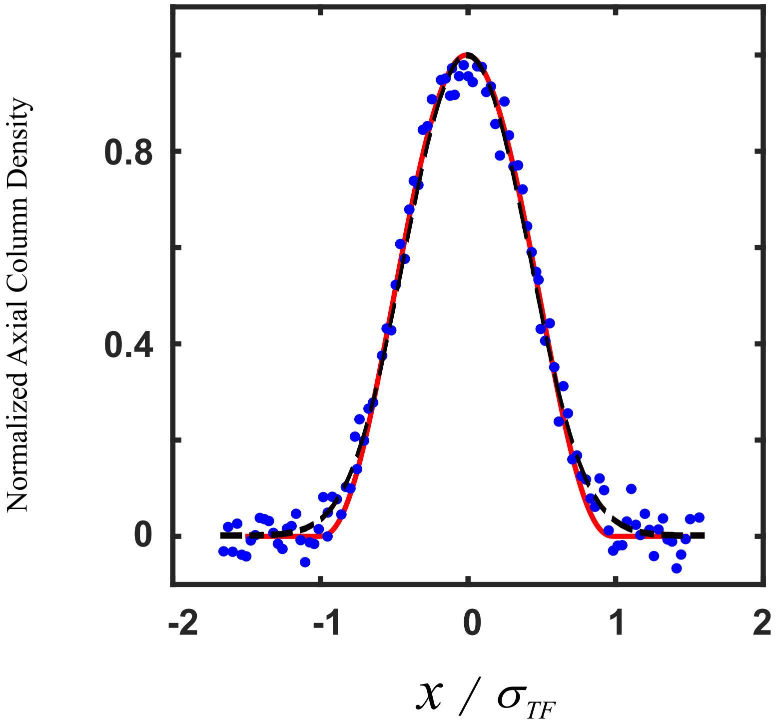

Figure 1.8: Normalized axial column density. (Blue), Total axial spin density from the last column of Fig. 1.4. (Red), Zero temperature Thomas-Fermi fit. (Black), finite temperature fit with $T/T_F = 0.32$. For this profile, $\sigma_{TF} = 310\ \mu m$ and $T_{TF} = 0.73\ \mu K$. In the degenerate regime, there is roughly 100 atoms/μm.

The other advantages that weakly interacting Fermi gases provide is a rich platform for investigating information spreading and spin coherence. In Ch 6, I demonstrate a protocol for the study of information scrambling, employing an inverse Abel-transform to extract energy-resolved out-of-time-order correlation functions and many-body coherence from the spatial profiles of the spin density.

1.2.1 Hamiltonian for a Weakly Interacting Two-Spin-1/2 System

In the investigation of many-body systems, the modeling of interparticle interactions is typically one of the central problems. Despite the complicated internal structure of atoms, the description of interactions between them can be greatly simplified, as shown in Sec. 2.2. From the conservation of total angular momentum, when two Fermi atoms with different spins collide, their respective electronic spins, $\vec{s}_1$ and $\vec{s}_2$, will add to make a total electronic spin

$$\vec{S} = \vec{s}_1 + \vec{s}_2, \tag{1.6}$$

which will have a value of either 0 or 1. For the singlet spin state, we have $S = 0$ and for the triplet spin state $S = 1$. In Ch. 2, I will explain in detail how different symmetries of these two electronic spin states cause their associated collisional potentials to respond differently when the collision occurs in a static magnetic field

Since s-wave scattering for Fermi gases is allowed only for antisymmetric spin states, two-component spins exhibit an effective exchange interaction, enabling simulations of a variety of spin-lattice models [Piéchon et al., 2009, Natu and Mueller, 2009, Deutsch et al., 2010, Wall, 2020]. We know that the spin operator does commute with $\vec{S}^{\,2}$, therefore

$$\left[\vec{S}^{\,2}, \vec{s}_1\right] = \left[\vec{S}^{\,2}, \vec{s}_2\right] = 0. \tag{1.7}$$

$\vec{S}^{\,2}$ of $\vec{s}_1$ and $\vec{s}_2$ gives rise to a projection operator $\hat{P}$ onto the singlet electron-spin subspace as

$$\vec{S}^{\,2} = (\vec{s}_1 + \vec{s}_2)^2 = 3/4 + 3/4 + 2\,\vec{s}_1 \cdot \vec{s}_2. \tag{1.8}$$

By rearranging Eq. 1.8, we have

$$\begin{aligned} 1 - \vec{S}^{\,2}/2 &= 1 - 3/4 - \vec{s}_1 \cdot \vec{s}_2 \\ \hat{P} \equiv 1 - \vec{S}^{\,2}/2 &= (1/4 - \vec{s}_1 \cdot \vec{s}_2). \end{aligned} \tag{1.9}$$

This projection operator for a singlet spin state with $S = 0$, projects an interacting pair of spins to $\hat{P} \to 1$ and for a triplet state ($S = 1$) to $\hat{P} \to 0$. Thus, $\hat{P}$ projects any two interacting spins to the triplet or the singlet subspaces, depending on their S.

As I mentioned earlier, in the low-energy limit, atomic interactions are well approximated by the s-wave scattering contact interaction, with the scattering length depending on the spin state of the colliding atoms. (Sec. 2.2.4). Thus, from Eq. 1.9, the effective exchange interaction for antisymmetric (singlet) spin states can be written as

$$H' = \tfrac{8\pi\hbar^2 a}{m}\hat{P}\ \delta(\vec{r}_1 - \vec{r}_2) = \tfrac{8\pi\hbar^2 a}{m}(1/4 - \vec{s}_1 \cdot \vec{s}_2)\ \delta(\vec{r}_1 - \vec{r}_2). \tag{1.10}$$

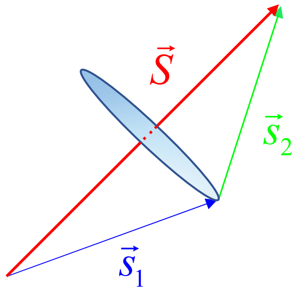

Figure 1.9: In a collision, two spins precess along the $\vec{S}$, where S always remains constant.

Note that the Hamiltonian is rotationally symmetric. Heisenberg equations for $\vec{s}_i$ yields

$$\dot{\vec{s}}_i = \frac{i}{\hbar}\frac{8\pi\hbar^2 a}{m}[-\vec{s}_1\cdot\vec{s}_2, (\vec{s}_1)_i]\delta(\vec{r}_1-\vec{r}_2). \tag{1.11}$$

The commutator relation on the right hand side can be written as

$$\begin{aligned}[\vec{s}_1\cdot\vec{s}_2, s_{1i}] &= [s_{1j}s_{2j}, s_{1i}] = s_{2j}\,[s_{1j}, s_{1i}]\\ &= s_{2j}\ \mathrm{i}\in_{jik}\ s_{1k}\\ -\ \mathrm{i}\in_{jki}s_{2j}s_{1k} &= -i(\vec{s}_2\times\vec{s}_1)_i.\end{aligned} \tag{1.12}$$

From Eq. 1.12, the right hand side of the Eq. 1.11 yields

$$\dot{\vec{s}}_1 = -\frac{8\pi\hbar a}{m}\delta(\vec{r}_1-\vec{r}_2)(\vec{s}_2\times\vec{s}_1). \tag{1.13}$$

similarly for $\vec{s}_2$, we have,

$$\dot{\vec{s}}_2 = -\frac{8\pi\hbar a}{m}\delta(\vec{r}_1-\vec{r}_2)(\vec{s}_1\times\vec{s}_2). \tag{1.14}$$

As shown in Fig. 1.9, for $\vec{S}$, from Eq. 1.13, 1.14, we have

$$\dot{\vec{S}} = \dot{\vec{s}}_1 + \dot{\vec{s}}_2 = 0. \tag{1.15}$$

Thus, the sum of two spins under the contact exchange interaction remains the same and $\vec{s}_1$ and $\vec{s}_1$ constantly rotate around $\vec{S}$.

If we have N-spins that are interacting, we can generalize the exchange Interaction Hamiltonian to

$$\frac{a_s}{2}\sum_{i,j\neq i}^{N} g_{ij}\,\vec{s}_i\cdot\vec{s}_j. \tag{1.16}$$

This is known as the Heisenberg Hamiltonian for interaction between many spins, where g_{ij}

is the coupling interaction between spins and plays the role of the site-to-site coupling in a lattice model and a_s is the s-wave scattering length. We will exploit this concept to describe the spin-segregation effect, Ch. 5.

1.3 Dissertation Organization

In Ch. 2, I overview the basic concepts of atom cooling and optical cooling techniques, which we apply for our experiments. I will start by talking about hyperfine and Zeeman interactions for ^{6}Li and will move to optical dipole traps. Then, I will present the method of obtaining absorption images of trapped atoms, which determines the spin density in the non-interacting Fermi gas. Finally, I will describe the lattice in energy space, which is created using a weakly interacting Fermi gas.

In Ch. 3, the detailed description of the mean-field model and its application for the many-body spin system is presented. I will show that for a coherently prepared cloud of ^{6}Li hyperfine states, there is a very good agreement between experimental spatial spin density profiles and the model. Then, the energy dependence of the scattering length near the zero-crossing is included to explain the observation of spin density profile in the nondegenerate regime at higher temperatures.

In Ch. 4, first, the theory of out-of-time order correlation (OTOC) functions is described. Then, I will show that by employing an inverse Abel-transform method, one can extract an energy-dependent spin vector from the spatial profile of the spin density. The OTOC functions and inverse-Able transform method provide the building blocks for the energy-resolved measurements in Ch. 6

In Ch. 5, I will present experimental measurements of time-dependent spin-density profiles for coherently prepared two-state Fermi gases of ^{6}Li. These measurements provide a precise quantitative test of the underlying energy-space spin-lattice model and energy-dependent long-range couplings discussed in Ch. 3. I will show this system allows implementing precise measurements of the zero crossings, where s-wave scattering length is zero, for ^{6}Li atoms.

In Ch. 6, energy-resolved out-of-time-order correlation functions and many-body coherence are extracted from the spatial profiles of the spin density using inverse Abel-transform method. Then, a new protocol for measuring the information scrambling in a large many-body system is implemented based on OTOC correlation functions in Ch. 3. From this energy-resolved study, we reveal the coherence structure hidden in measurements of the total collective spin vector.

In Ch. 7, the summary of the dissertation and the outlook for the future work is provided.

Chapter 2

Background

In this chapter, I will give a reader an overview on some of the basic concepts that apply to atom and optical cooling techniques. In our laboratory, atom-atom interactions are tuned by means of magneto optical traps (MOT), and atoms can be cooled through two stages. First, atom cool to the Doppler limit, using the MOT. In the second stage, atoms evaporatively cooled to nK, below the Doppler cooling limit, in optical dipole traps. Therefore, I will start by talking about the single atom interactions for ^{6}Li and will move to optical dipole traps. Then, I present the main part of the apparatus that leads to absorption images of atoms.

2.1 ^{6}Li atomic structure

Since we implement experiments on ^{6}Li atoms, first I will talk briefly about the electronic structure of ^{6}Li that is covered extensively in all previous thesis in our group. Therefore, I suggest the reader to refer to older theses [Elliott, 2014, Ong, 2015], in our group to get a detailed description. The alkali metal employed in our laboratories for atom cooling and trapping experiments is an isotope of lithium, ^{6}Li. An atom of ^{6}Li is composed of 3 protons, 3 neutrons, and 3 electrons, yielding an overall charge neutral. The valence electron makes the total atom spin half integral so that neutral ^{6}Li atom is fermion. The nuclear ground state has nuclear spin $I = 1$, while the electronic ground state consists of 2 electrons in the 1s orbital and a third, electron in the 2s orbital. The total angular momentum quantum number F arises from the sum of nuclear, orbital, and electron spins. In the electronic ground state, ($I = 1$, $L = 0$, and $S = 1/2$), angular momentum addition yields two possible values for the total angular momentum, $F = 3/2$ and $F = 1/2$.

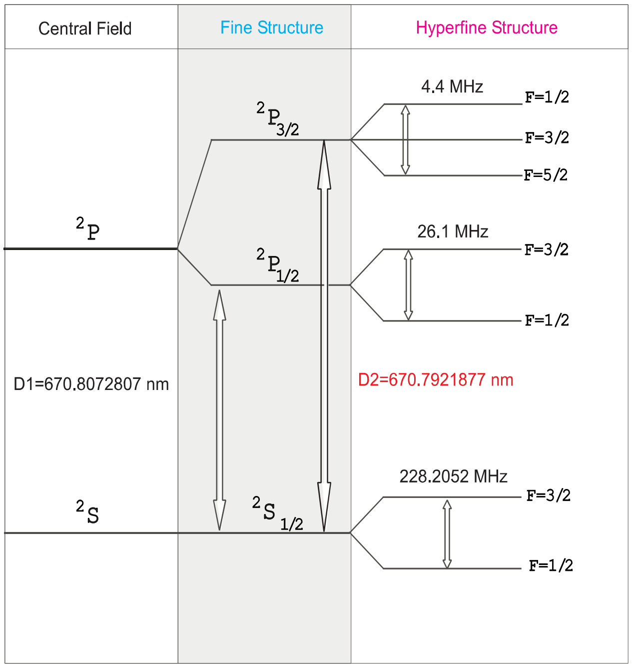

Figure 2.1: Fine structure and hyperfine structure of ^{6}Li. D_2 transition, in red color, is the transition that we use for trapping the atoms in the magneto optical trap.

2.1.1 Hyperfine States in Zero Magnetic Field

The fine structure of ^{6}Li arises from the magnetic dipole interaction between the electronic spin angular momentum, $\mathbf{S}$, and the orbital angular momentum, $\mathbf{L}$, resulting in a total angular momentum of $\mathbf{J} = \mathbf{L} + \mathbf{S}$. Because of this interaction, the transition from the ground state to the excited state splits into the $D1$ and $D2$ lines indicated in Fig. 2.1, corresponding to the fine structure transitions of $2^2\mathrm{S}_{1/2} \leftrightarrow 2^2\mathrm{P}_{1/2}$ and $2^2\mathrm{S}_{1/2} \leftrightarrow 2^2\mathrm{P}_{3/2}$ respectively.

Hyperfine splitting of the ground and excited states arises from the interaction between the valence electron and the magnetic and quadrupole moments of the nonspherically symmetric nucleus. The Hamiltonian of the hyperfine interaction includes both the nuclear magnetic dipole and nuclear electric quadrupole interactions.

In the absence of an external magnetic field, the total angular momentum $\mathbf{F} = \mathbf{I} + \mathbf{S}$ is conserved. The $F = 1/2$ manifold of the ground state is two-fold degenerate, with spin projections $m_F = \pm 1/2$, while the $F = 3/2$ manifold of the ground state is four-fold degenerate, with spin projections $m_F = \pm 3/2$, $m_F = \pm 1/2$.

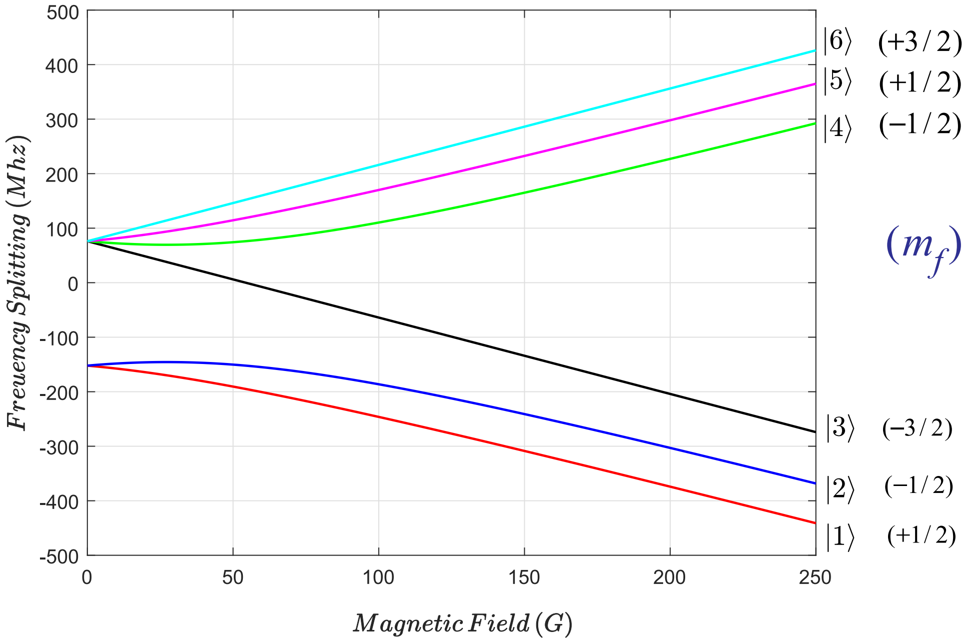

Figure 2.2: Tuning of energy of the lowest six hyperfine states with an externally applied magnetic field in Gauss unit. a_0 is the Bohr radius.

2.1.2 Zeeman splitting in an external B field

In the presence of a strong magnetic field, the magnetic interaction energy can not be treated as a perturbation on the electron-nucleus interaction in the most general cases. That means F and m_F are no longer good angular momentum quantum numbers.

The interaction between the electron and the nuclear magnetic moments as well as an externally applied magnetic field, which breaks this degenracy, can be written as the following:

$$H_{\text{int}} = \frac{a_{hf}}{\hbar^2}\,\mathbf{S}\cdot\mathbf{I} \;-\; \frac{\mu_B}{\hbar}\,(g_J\;\mathbf{S} + g_I\;\mathbf{I})\cdot\mathbf{B} \tag{2.1}$$

where $a_{hf}/h = 152.137$ MHz is the magnetic hyperfine constant and $g_J = -2.002$ is the total electronic g-factor for the ^{6}Li ground state, $g_I = +0.000448$ is the total nuclear g-factor, μ_B is the bohr magneton, and B is the external magnetic field.

At the zero field position in Fig. 2.2, the total angular momentum quantum numbers $F = 1/2$ and $F = 3/2$ are good quantum numbers. When the magnetic field increases, the six energy levels evolve into two groups because the hyperfine interaction is much smaller than the magnetic interaction when the magnetic field is large enough. Under this condition, the eigenstates eventually are the product states $|m_S\; m_I\rangle$, where m_S and m_I are respectively the projections of $\mathbf{S}$ and $\mathbf{I}$ onto the quantization axis. These six distinct eigenstates are conventionally labeled as $|1\rangle$, $|2\rangle$, $|3\rangle$, $|4\rangle$, $|5\rangle$, and $|6\rangle$ in the order of increasing energy. As the magnetic field increases, the hyperfine energy shift for the three lowest states approximately is -1.4 MHz/G. The energy differences between energy levels correspond to resonant radiofrequency transitions which we use for the purposes of magnetic field calibration.

In the next section, I will talk about what mixture of states we experimentally prepare and tunable interaction between atoms.

2.2 Atom-Atom Interaction in Ultracold Fermi Gases

In our laboratory, the initial stages of our experimental sequence are designed to produce a 50-50 mixture of the $|1\rangle$, $|2\rangle$ hyperfine ground states. One may ask why are these states preferable to other two-component mixture? There are several reasons. First, there are unitary resonances (strongly interacting regime) in the $|1\rangle$, $|2\rangle$ mixture which occur at experimentally accessible magnetic fields. These resonances which usually known as Feshbach resonance are depicted in Fig. 2.6 [Bartenstein et al., 2005].

A second reason for studying the $|1\rangle$, $|2\rangle$ mixture is that it is an energetically stable combination of states and they are stable against collisional decay to a dark state. This mixture has the lowest internal energy of any interacting mixture. The low-energy nature of the mixture is important because many higher-energy mixtures have open inelastic collision channels whereby an atom can change its internal state and release enough energy to eject one or more atoms from the trap. Mixtures with open inelastic channels tend to destroy themselves.

Third, at zero-field, $|1\rangle$, $|2\rangle$ mixture consists of states that are in some sense mirror images of one another; they differ only in the sign of their magnetic quantum number. This makes the mixture particularly well-suited for studies of spin dependent potential and higher order quantum coherence, those experiments will be discussed in Ch. 5, Ch. 6. Therefore, since the $|1\rangle$, $|2\rangle$ mixture is stable against inelastic collisions, and possesses tunable s-wave interaction at experimentally accessible magnetic fields, it is an excellent choice for researchers to study two-component weakly interacting Fermi gases.

In order to study different interaction regimes, such as weakly and strongly interacting Fermi gases, first we need to make ourselves more familiar with the concept of s-wave scattering and Feshbach resonances in an ultracold ^{6}Li gas.

2.2.1 s-wave Quantum Scattering

The quantum scattering of two particles is a central topic in nearly every quantum mechanics textbook [Griffths, 2005, Zettili, 2009] and in previous dissertations from this group [Elliott, 2014]. Here, I will provide a brief introduction to s-wave quantum scattering, which provides a valuable experimental knob throughout this dissertation.

Neutral alkali atoms interact primarily via an electrostatic molecular potential V($\mathbf{r}$), which only depends on the distance r between the particles. The result of the scattering event will be observed in the far field, far past the range of an interatomic potential, so that the outgoing, scattered wave can be approximated as a spherical wave.

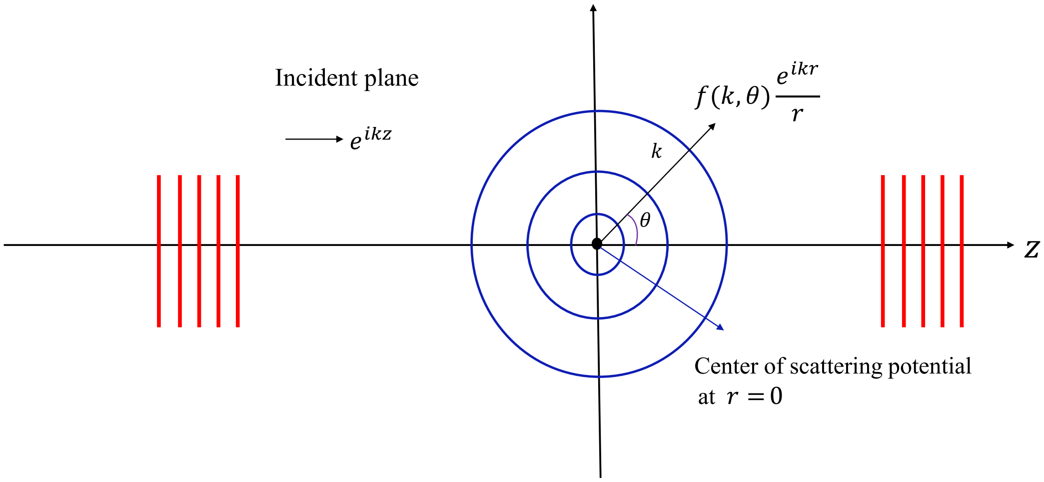

Figure 2.3: An incoming plane wave scattering off a potential to an outgoing spherical wave. This is the asymptotic form of the wave function expected from scattering theory, where the amplitude of the outgoing wave is $f(k,\theta)$ which is referred to as the scattering amplitude.

Consider a wave of incident particle traveling in the $+\hat{z}$ direction with momentum $\mathbf{k}\hbar$, which encounters a scattering potential, producing an outgoing spherical wave Fig. 2.3. At long distances from the center of the scattering center, the asymptotic single particle scattered wavefunction will consist of an incident plane wave e^{ikz} plus an outgoing spherical wave due to scattering from the potential:

$$\psi_{\mathbf{k}} = \frac{1}{\sqrt{V}}\,(e^{ikz} + \frac{f(k,\theta)}{r}e^{ikr}) \tag{2.2}$$

In order to find the probability of the scattering in a given direction θ, we need to determine the *scattering amplitude* f, which is a function of the incoming momentum and coordinate angles between the incident direction and the scattered direction $+\hat{z}$ of the particle. V is the volume in which the incident wave is normalized with.

From conservation of particle flux we have,

$$\vec{J}_{tot} = \vec{J}_{inc} + \vec{J}_{scatt}. \tag{2.3}$$

In the limit of $r \to \infty$, the incident flux on the scattering potential is

$$\vec{J}_{inc} = \frac{\mathbf{k}\hbar}{\mu}\frac{1}{V}\hat{z} \tag{2.4}$$

and the scattered flux, due to the forward interference that occurs in an arbitrary small angular area of $r^2 d\Omega$, is

$$\vec{J}_{scatt} = \frac{|f(k,\theta)|^2}{r^2}\frac{k\hbar}{\mu}\frac{1}{V}\hat{r}. \tag{2.5}$$

From Eq. 2.4 and Eq. 2.5, we can conclude that radial flux, which is $\propto \frac{1}{r^2}$, through a small area of $r^2 d\Omega$ is independent of unscattered flux, and the radial flux through a small area in the differential solid angle $r^2 d\Omega$ is

$$J_{scatt} d\sigma = |f|^2 d\Omega. \tag{2.6}$$

In the next section, we will obtain the differential cross-section, which is the ratio of the scattered flux to the incident flux.

2.2.2 Collisional Cross Section

The form of the collision cross section, σ_c as the result of azimuthal symmetric $V(r)$, is related to $f(k,\theta)$ through the conservation of probability. When the ratio of the rate of probability leaving the scattered area in the differential solid angle $r^2 d\Omega$ compared to rate of probability incident in the plane perpendicular to the incoming plane wave, we have:

$$\frac{d\sigma_c}{d\Omega} = |f(k,\theta)|^2 \tag{2.7}$$

This is the fundamental relation between the differential scattering cross section and the scattering amplitude.

If we assume the scattering potential is a central potential, we can expand the scattered wave functions in an orbital angular momentum basis $|l\rangle$ with the Legendre polynomials $P_l(x)$,

$$f(\theta,k) = \sum_{l=0}^{\infty} (2l+1) a_l(k) P_l(\cos(\theta)) \tag{2.8}$$

for the case of s-wave scattering where $l = 0$, we have

$$f(\theta, k) = \sum_{l=0}^{\infty} s_l(k) P_l(\cos(\theta)) \tag{2.9}$$

The coefficients of this expansions are known as the *partial wave amplitudes*, which are related to the scattering phase shifts δ_l by, [Sakurai, 1994],

$$\begin{aligned} s_l(k) &= \frac{e^{2i\delta_l} - 1}{2ik} \\ &= \frac{\sin(\delta_l) e^{i\delta_l}}{k}. \end{aligned} \tag{2.10}$$

In the case of an ultracold gas of ^{6}Li atoms, the dominant quantum scattering process is the s-wave ($l = 0$) due to the extremely low kinetic energy of the colliding atoms. To prove this quantitatively, the range of the interatomic potential between colliding ^{6}Li atoms is roughly $r_0 \approx$ 20 bohr $\approx 1\ nm$, and the temperature of the gas is on the order of 1 μK corresponding to the thermal de Broglie wavelength of approximately $\lambda_T = 700$ nm. The wavelength is significantly larger than the range of the potential, so that if we quantize the angular momentum l of the gas via the relation $l\hbar = r_0 p = r_0(h/\lambda_T)$, then l is given by:

$$l = \frac{2\pi r}{\lambda_T} \approx 0.001. \tag{2.11}$$

Therefore, the only relevant value for l is zero for scattering processes of ultracold Fermi gases.

The total scattering cross section of s-wave scattering is obtained by integrating Eq. 2.7 over the solid angle $d\Omega = \sin\theta \, d\theta d\phi$, we arrive at an expression for the s-wave collisional cross section given by

$$\sigma_c = \frac{4\pi}{k^2} \sin^2\delta. \tag{2.12}$$

2.2.3 The Scattering Length a_s

Using the partial wave analysis for a spherically symmetrical potential $V(r)$, we can write the s-wave radial Schrödinger equation in dimensionless units as

$$\left\{ \frac{d^2}{dr^2} + k^2 - \frac{2\mu}{m} V(r) \right\} u_{k0}(r) = 0. \tag{2.13}$$

where r is the separation in bohr, k is the wave number in inverse bohr, m is the electron mass, μ is the reduced mass of two ^{6}Li atoms. The radial wavefunctions of Eq. 2.13, in the asymptotic limit, have the low energy form as

$$\begin{aligned} u(r) &= C\sin(\text{ kr } + \delta) \\ \psi(\text{r}) &= \frac{u(r)}{r}. \end{aligned} \tag{2.14}$$

In the zero energy $k \to 0$ limit of low energy interactions, collision strength between atoms is characterized by a single parameter known as the s-wave scattering length.

This scattering length has a simple geometric interpretation, which is shown in Fig. 2.4. To give a physical interpretation of the scattering length a_s pointed in [Sakurai, 1994], we assume the center of the scattering potential is located at the origin of a spherical coordinate system, Fig. 2.3. In the limit of $k \to 0$, the scattering length is defined as the distance between the origin and the crossing point of the asymptotic radial wavefunction on the r axis. Therefore, the value of a_s represents how much the particle wavefunction is phase shifted by the scattering potential shown in Fig. 2.4.

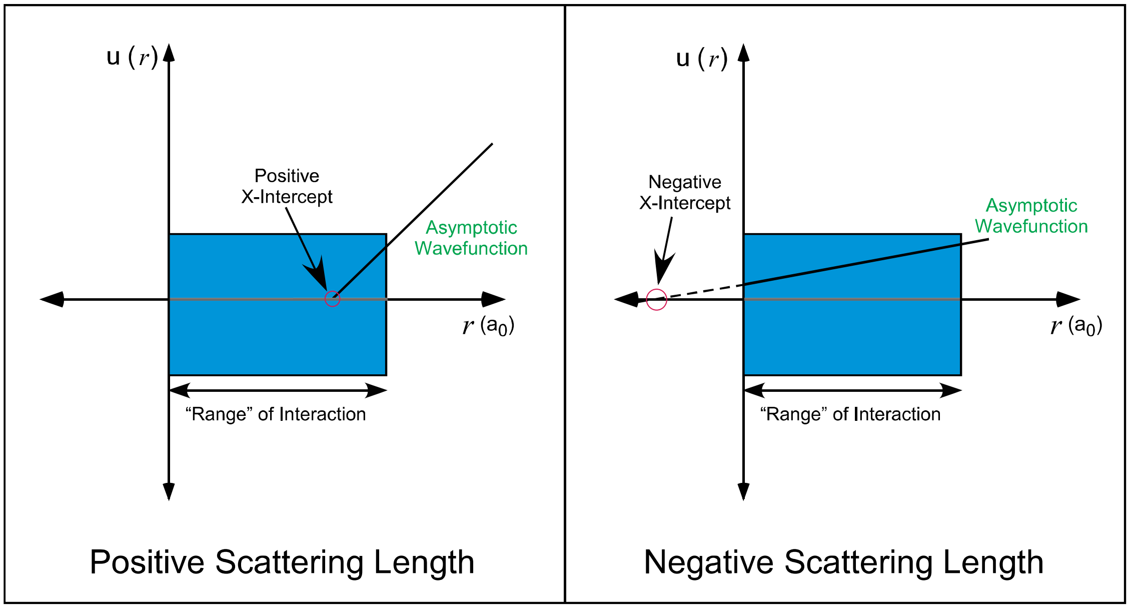

Figure 2.4: Determination of Scattering Length.

Larger a_s represents stronger interactions between the particles. The sign of the scattering length indicates the overall effect of the potential. A positive a_s indicates that the scattering wavefunction is pushed away from the origin by the scattering potential, which indicates that the effective interaction is repulsive. On the contrary, a negative scattering length shows the scattering wavefunction is pulled closer to the origin, which represents an effective attractive interaction. The total scattering cross section using Eq. 2.14 can also be written in term of the scattering length as

$$\begin{aligned} \underset{k\to 0}{k\cot\delta} &= -\frac{1}{a_s}+\frac{k^2 r}{2} \\ a_s &\equiv -\lim_{k\to 0}\frac{\tan\delta}{k} \\ \sigma_c &= 4\pi a_s^2 \qquad k a_s \to 0. \end{aligned} \tag{2.15}$$

There are two limiting cases, the strongly interacting limit ($ka_s \gg 1$) and the weakly interacting limit ($ka_s \ll 1$). In the weakly interacting limit $a_s \ll 1/k \simeq \lambda_{dB}/2\pi$ which means that the zero energy s-wave scattering length is much smaller than the De Broglie wavelength of the relative momentum of the colliding atoms. Thus, the scattering cross section reduced to $\sigma_s \approx 4\pi a_s^2$. However in the unitary limit the opposite is true and when $a \to \pm\infty$ the scattering cross section becomes $\sigma_c = 4\pi/k^2$. This is unitary limit and the scattering becomes independent of the scattering length.

2.2.4 Tunable Interactions

Here I will describe collisions via Feshbach resonance and their role in cold atoms interactions. I highly recommend you to read more thorough discussion of strongly interacting regimes through previous theses of [Elliott, 2014].

Experimentally, Feshbach resonance is achieved by making use of a magnetically induced collisional Feshbach resonance, which occurs for two atoms in a bias magnetic field. Colliding atoms interact through two distinct attractive potentials in an atomic gas. Repulsive interactions arising from a repulsive potential will not produce molecules, but the repulsive interactions from an attractive molecular potential can led to molecules. The ^{6}Li atoms in the different spin states $|1\rangle$ and $|2\rangle$ in our laboratory, interact via either a singlet or triplet molecular potential. For s-wave scattering in singlet potential, the valence electrons from two different atoms form a spin singlet state with $S_{total} = s_1 + s_2 = 0$. In contrast, the triplet potential is made by the electrons combining to spin triplet state $S_{total} = s_1 + s_2 = 1$.

As electrons are fermions, their overall electronic wave function must be antisymmetric, so the triplet state must accompany a spatially antisymmetric two electron state, while the singlet state requires a spatially symmetric two electron state. The spatially symmetric state allowed by the singlet state concentrates the electrons towards the middle of the two atoms, attracting the nuclei inward and helping to shield the repulsive forces between the nuclei, which creates a potential well much deeper than the spatially antisymmetric spin state associated with the triplet state. Despite this, the triplet potential is able to interact with the singlet potential via

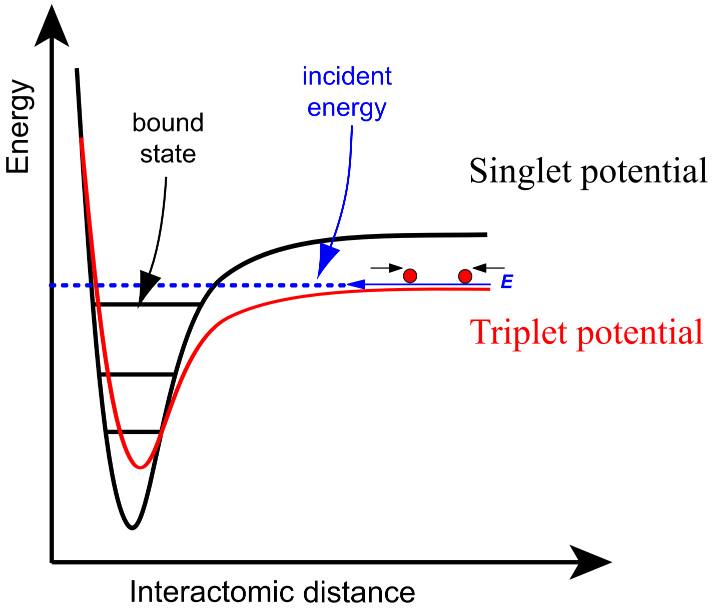

Figure 2.5: The two-channel model for a Feshbach resonance. Atoms, which are prepared in the open channel, undergo a collision at low incident energy. In the course of the hypefine interaction, the open channel is coupled to the closed channel. When the incident energy in the open channel has the energy close to the bound state of the closed channel, Feshbach resonance occurs.

tunable bias magnetic field.

In addition to electronic spin, an atom also has a small nuclear spin coupled to its electronic spin through the hyperfine interaction, the associated energy of which is given by $V_{hf} = a_{hf}(\vec{s}.\vec{i})$ where i is the nuclear spin and a_{hf} is the hyperfine coupling. If the total hyperfine interaction between two colliding atoms is considered,

$$\begin{aligned} V_{hf\ \text{Total}} &= V_{hf1} + V_{hf2} = a_{hf}(s_1 \,.\, i_1 + s_2 \,.\, i_2) \\ &= \frac{a_{hf}}{2}\Big[(s_1 + s_2)\,.\,(i_1 + i_2) + (s_1 - s_2)\,.\,(i_1 - i_2)\Big]. \end{aligned} \tag{2.16}$$

It is this coupling that allows a nearby bound state of the deeper singlet well to affect the scattered free atoms, although they must enter and exit along the triplet channel as it is shown in Fig. 2.5. The different symmetries of these two electronic spin states also cause their associated collisional potentials to respond differently when the collision occurs in a static magnetic field. The basis for colliding particle that we work with, includes the total spin as $\vec{S} = \vec{s}_1 + \vec{s}_2$ and

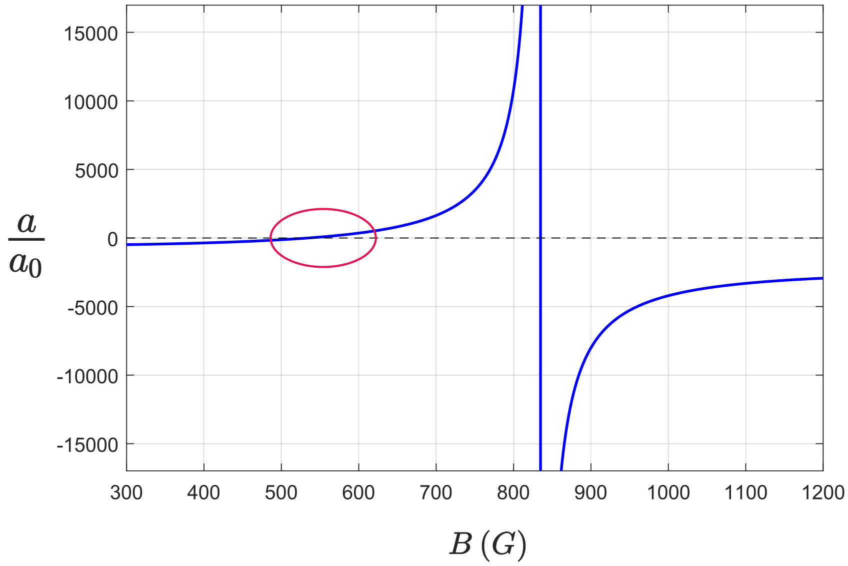

Figure 2.6: s-wave scattering length vs applied magnetic field for $|1\rangle$ and $|2\rangle$ mixture. The red circle shows the location where scattering length is zero (zero-crossing).

total nuclear spins as $\vec{I} = \vec{i}_1 + \vec{i}_2$. Thus the basis that we have in a static magnetic field is,

$$|S\ m_s\rangle\,|I\ m_I\rangle \tag{2.17}$$

According to the ground energy eigenstate for ^{6}Li atoms that we labeled as $|1\rangle$... $|6\rangle$, in a magnetic field, a pair of atoms in the two lowest states, $|1\rangle = \left|-\frac{1}{2}, 1\right\rangle$ and $|2\rangle = \left|-\frac{1}{2}, 0\right\rangle$, is almost a pure triplet state with a small singlet admixture at these large magnetic fields. The spins of the singlet state are anti-parallel and have a negligible dipole moment that is not tunable with a magnetic field, while for triplet state, the spins are parallel and the energy of the two atom state varies with magnetic field approximately as $-2\mu_B$.

The triplet state is an open channel for interactions and the singlet state is a closed channel, which is energetically inaccessible at long range. Therefore, by adjusting the magnetic field, the energy of the open channel can be tuned such that it is in resonance with a bound singlet state of higher lying closed channels. In other words, the energy of the two colliding atoms in the triplet state can be degenerate with the energy bound molecular vibrational state in the singlet molecular potential. Under this condition, the scattering length between the colliding atoms is enhanced dramatically, which results in the Feshbach resonance, as shown in Fig. 2.6.

One of the dominant resonances between states $|1\rangle$ and $|2\rangle$ occurs at 832.2 G (broad). For our experiment, we exploit the broad resonance to tune the interaction between the two colliding atoms. Near 832.2 G, the zero energy scattering length is approximated by,

$$a = a_{bg}\Big(1 - \frac{\Delta_B}{B - B_0}\Big) \tag{2.18}$$

where $a_{bg} = -1405\,a_0$, $B_0 = 832.2\,G$ and $\Delta_B = 300\,G$. Fig. 2.6 shows how scattering length a, changes near the resonance. The existence of Feshbach resonance means that not only we can explore weakly-interacting mixtures for $a \to 0$ (by magnetically-tuning the magnitude of the scattering length), but that we can also change the sign of the interactions by simply scanning a, from positive to negative or vice-versa. Thus, we have complete control not only of whether the mixture is interacting or noninteracting, but also over the type and strength of the interaction. Much of the exciting physics of fermionic gases depends on the details of the scattering interactions—Working with Feshbach resonance in two-component mixtures means we have the capability to easily explore all the possible regimes.

For most experiments presented in this dissertation on studying a weakly interacting Fermi gas, we initially use an ultracold degenerate Fermi gas at the Feshbach resonance of 832.2 Gauss, and tune the field downward, setting the bias magnetic field at 527 G, to study a noninteracting Fermi gas. At this field scattering length is nearly vanishing ($a = 0$). We call this zero-crossing, which refers to the point that scattering length in Fig. 2.6, crosses the x-axis.

2.3 Experimental Setup

Here, I summarize the cooling and trapping techniques used in the initial stages of atom preparation for experiments that will be discussed in Ch. 5 and Ch. 6. These techniques and equipment have been covered in great detail in previous theses [Gehm, 2003,Kinast, 2006,Luo, 2008,Elliott, 2014], but I will describe them briefly in this chapter to provide background for the current work.

2.3.1 Zeeman slower

We start by evaporating solid ^{6}Li stored in an oven and directing the atomic beam in to a vacuum chamber where a magnito-optical trap (MOT) and a CO_2 laser optical dipole trap are used to cool and trap the atoms. In the process of evaporating, solid ^{6}Li is heated up to about $\simeq$ 400°C and vaporized through a long beam collimating wick nozzle such a way that the temperature from about 400°C at the oven drops to 250°C at the end of the nozzle. This temperature gradient assures that any condensed ^{6}Li is recycled back to the oven, which greatly extending the lifetime of the oven.

As the thermal velocity of the atoms exiting the oven region is too high for them to be captured by a magneto-optical trap, the atomic beam enters the Zeeman slower, Fig. 2.7 right,

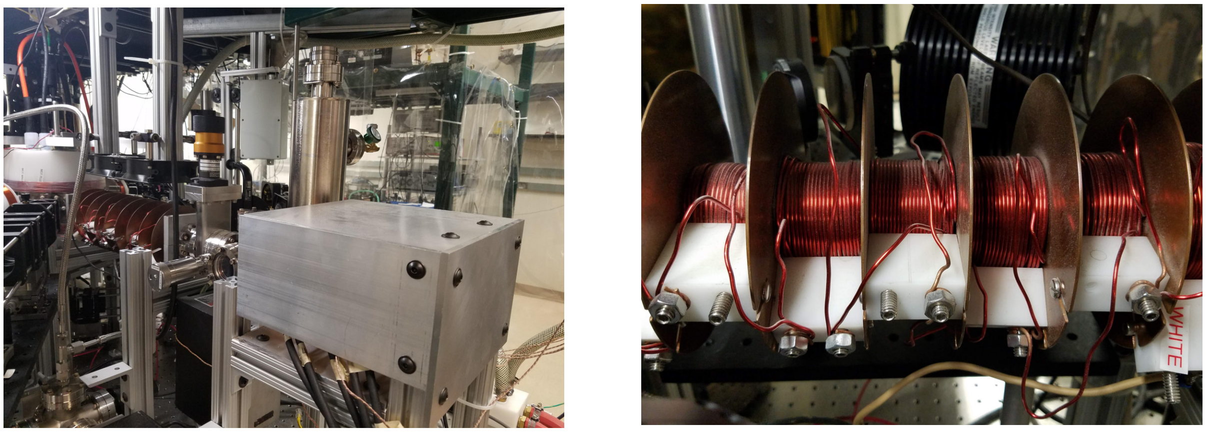

Figure 2.7: ^{6}Li oven on the left and Zeeman slower on the right.

where it is overlapped with a counterpropagating red-detuned laser beam in a spatially varying magnetic field, which is used to produce a Zeeman shift. The magnitude of the magnetic field, created by a series of electromagnetic coils, is set to spatially decrease velocity of atoms as they move along the Zeeman slower. Atoms with large velocities are slowed by absorbing counter-propagating photons that are brought into resonance by the Doppler effect and Zeeman shift from the magnetic field. Both the Zeeman slower and the magneto-optical trap are based on the radiation pressure force. Radiation pressure causes a force on the atom in the direction of propagation of the incident light that I will explain in more depth in Sec. 2.4.1.

Finally, using a one dimensional radiation pressure in a Zeeman slower, we slow down the atomic beam of vapor with thermal velocities of over 1000 m/s down to about 30 m/s.

After exiting the Zeeman slower, atoms are trapped and cooled by three retro reflected orthogonal beams overlapping near the point of zero magnetic field gradient of a quadrupole magnetic field which will be explained below. The mechanism for trapping and cooling in the MOT relies on the momentum transfer from absorbed photons. The recoil momentum from photons emitted from atoms in the MOT puts a lower bound, Doppler limit cooling, on the temperatures that can be achieved in the MOT which is $\sim 140\ \mu$K. For further cooling, we transfer atoms from the MOT to a dipole force trap, which does not rely on the momentum of photons for trapping and cooling. Finally, we achieve much lower temperatures by evaporatively cooling atoms held in the dipole trap.

2.4 Magneto-optical trap

Our apparatus uses two physical mechanisms of magneto optical trap for cooling and trapping the atomic sample, and for future cooling, we create an optical dipole trap using a far off-resonance CO2 laser. A Coherent 899-21 dye laser pumped by a Verdi V-10 solid state laser along with standard frequency stabilization techniques, generates laser beam with a wavelength, near the D_2 of Fig. 2.1, resonance near 670.9 nm with a linewidth $\simeq$1 MHz to be used as the trapping beams for the magneto-optical trap. We get approximately 800 mW of power from the dye laser. The beam from the dye laser is processed further to generate all the beams necessary for our cooling and trapping experiments, namely, the slower beam, the MOT (Magneto-optical trap) beams and, the repumper beams, whose purpose is explained in detailed below.

In the following, I will explain in more detail the two stages of MOT and FORT that we apply for in the atomic sample preparation for the experiment.

2.4.1 Velocity dependent radiation pressure

The first cooling mechanism uses the momentum of photons $p = \hbar k = h/\lambda$ to reduce the velocity of the atoms. Imagine a laser beam with a laser frequency of $\nu_L = \nu_0\ (1 - v_a/c)$ tuned below the atomic resonance where v_a is atom velocity. The frequency seen by an atom moving towards the laser beam is Doppler shifted up, (see below); this will provide a net momentum transfer in the opposite direction. In the rest frame of the atom, the photon frequency due to Doppler effect is

$$\nu_L' = \nu_L\ (1 + v_a/c) \approx \nu_0 - v_a/c + v_a/c, \tag{2.19}$$

where ν_L' is the frequency observed by the atom, ν_0 is the photon frequency and c is the speed

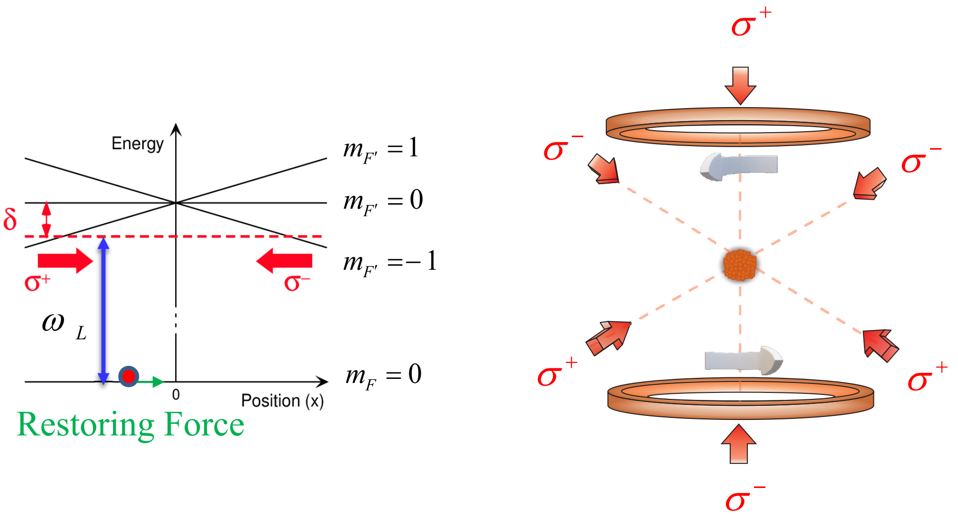

Figure 2.8: The magneto-optical trap (MOT). Three orthogonal retro-reflected laser beams along with the quadrupole magnetic field generated by two electromagnetic coils in an anti-Helmholtz configuration trap.

of light. When this condition is satisfied, the photon will be resonant with atoms moving in the atom direction and will be absorbed by the atoms that go to an excited state. Through spontaneous emission, atoms emit another photon with the same frequency in a random direction. However, due to conservation of momentum during the absorption and emission process, a photon absorbed by an atom will transfer momentum to the atom in the direction that the photon was traveling. We can reduce the velocity of atoms by applying radiation pressure force on them. In one dimension, two overlapping counter propagating laser beams that have been tuned below the atomic resonance will slow atoms moving in either direction. This velocity dependent radiation pressure, also called optical molasses, is used to slow down atoms in three dimensions, as shown in Fig. 2.8, by overlapping three orthogonal counterpropagating laser beams pairs. In the next section, I will talk about spatial confinement in three directions.

2.4.2 Spatially dependent radiation pressure

A spatially varying magnetic field will create a spatially dependent energy shift that we use to trap atoms. Between the two magnets the field is zero and its magnitude increases linearly in all directions from this point. For simplicity, we consider atoms in a ground state with total angular momentum $F = 0$, and atoms in the first excited state with total angular momentum $F = 1$. A spherical quadrupole magnetic field splits the degeneracy of the hyperfine states to $m_F = -1, 0, +1$, resulting in a linear variation of the energy levels about the center of the trap. The red-detuned laser beams used to create a velocity dependent radiation pressure are cicrularly polarized to provide a spatially dependent radiation pressure to atoms in a spatially varying magnetic field. Atoms in a region of positive magnetic field will have $m_F = -1$ excited state sublevel shifted down in energy and will absorb circularly polarized σ_- photons. Atoms in a negative magnetic field will have the $m_F = +1$ excited sublevel downshifted and will absorb σ_+ polarized photons.

Consider a one dimensional case where atoms are free to move in a magnetic field that increases linearly in the positive direction about a zero point. A beam propagating in the positive direction with σ_+ polarization is overlapped with a beam propagating in the negative direction with σ_- polarization. Atoms in regions of negative magnetic field absorb σ_+ photons and receive momentum kicks in the positive direction. Atoms in regions of positive magnetic field absorb σ_- photons and receive momentum kicks in the negative direction. The combined result of the magnetic and optical fields creates a spatially dependent radiation pressure that confines atoms near the zero point of the magnetic field. The spatially dependent radiation pressure, in addition to the velocity dependent radiation pressure is used to trap and cool atoms in three dimensions.

In the MOT, this photon absorption and emission are used to create velocity and spatially dependent radiation pressure shown in Fig. 2.8, near the 671 nm transition of ^{6}Li with linewidth of 5.9 MHz, which provides a source of cold atoms. The MOT, at full intensity, spatially confines the atoms and cools them to ~ 1 mK. At the end of the MOT cooling stage temperature is reduced to doppler limit of 140 μK, with an average velocity of about 60 cm/s. Atoms are then transfered to a far off-resonance optical dipole trap (FORT) before extinguishing the magnetic field and the trapping beams for the MOT. The MOT beams are extinguished and a bias magnetic field of ~ 8 G is applied to break the degeneracy of $^2S_{1/2}$ (F = 1/2) ground state, shown in Fig. 2.2, where the atoms are trapped. Then a frequncy modulated radio frequency pulse with a central frequency correspond to the energy splitting between the lowest two hyperfine states (states $|1\rangle$ and $|2\rangle$) is applied to obtained a balanced mixture of the lowest hyperfine states $|1\rangle$ and $|2\rangle$.

The frequency of the MOT beams primarily corresponds to the F = 3/2 ground state in Fig. 2.1 to the excited state transition. However, the atoms that exit the Zeeman slower region, will populate both the F = 1/2 and F = 3/2 ground states. The F = 1/2 ground state is 228 MHz lower in energy than the F = 3/2 ground state. In order to cool the atoms that populate both the ground states, we use an acoustooptical modulator (AOM) to generate an additional optical beam, "repumper" beam, whose frequency corresponds to the F = 1/2 ground state to the excited state transition. The MOT beam and the repumper beam are overlapped and their powers are empirically chosen to be in the ratio of 3:1.

The MOT precooling is done in three phases. In the "loading" phase, both the MOT beam and the repumper beam are detuned by about 30 MHz from resonance. The loading phase will initially load the atoms exiting from the slower region into the MOT. The second phase is the "cooling" phase, where both the MOT beams and the repumper beams are tuned to within 3 MHz of resonance. The final phase is the "optical pumping" phase, where the MOT beam is tuned to resonance and the repumper is turned off. The optical pumping phase transfers all the atoms in the F = 3/2 ground state to the F = 1/2 ground state.

At the end of the MOT precooling phase, we have about 300 million atoms in the F=1/2 ground state at a Doppler limited temperature of 140 μK. Fig. 2.9 shows fluorescence from the atoms trapped in the MOT.

2.5 Optical Dipole Traps

When a neutral atom is placed in an electric field $\mathbf{E}$, the interaction creates an induced dipole moment $\mathbf{d} = \alpha\mathbf{E}$ in the atom, where α is the polarizability. Then the potential of the induced dipole moment is given by

$$V_{dip} = -\frac{1}{2}\mathbf{d}\cdot\mathbf{E}. \tag{2.20}$$

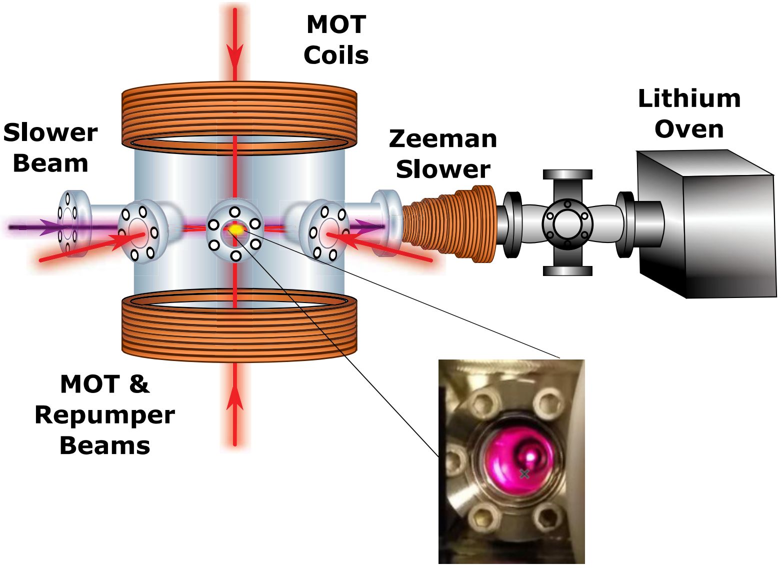

Figure 2.9: Experimental setup for initial cooling of atoms by the Zeeman slower, slower beam, precooling by the MOT beams, repumper beams, and MOT coils. MOT and repumper beams are overlapped and are shown together in red. Inset shows Fluorescence from the atoms trapped in the MOT.

where the factor of $\frac{1}{2}$ accounts for the fact that the dipole moment is an induced, not a permanent one. Atoms polarized in the electric field of a laser, detuned far from an atomic resonance, will experience a force from the dipole interaction $\mathbf{F} = -\nabla V_{dip}$, where the cycle-averaged potential of the electric field is

$$V_{dip} = -\frac{1}{2}\,\alpha\,\overline{\mathbf{E^2}} = \frac{-2\pi}{c}\,\alpha(\omega)\,I(x,y,z), \tag{2.21}$$

where c is the speed of light, $\alpha(\omega)$ the polarizability of the sample, and $I(x,y,z)$ the intensity of the laser beam. The dipole polarizability of ^{6}Li

$$\alpha(\omega) = \frac{\alpha_0\,\omega_0^2}{\omega_0^2 - \omega^2}, \tag{2.22}$$

is determined by the frequency of the laser light ω, where $\alpha_0 = 24.310^{-24}\ cm^3$ is the static polarizability [Wiese et al., 1966] and ω_0 is the resonant frequency. Atoms will be attracted to regions of high laser intensity when the $\omega > \omega_0$ or repelled when $\omega < \omega_0$. The intensity I of the laser beam in Eq. 2.21 is given by,

$$I = \frac{I_0}{1 + (z/z_0)^2}\,e^{-2r^2/w^2} \tag{2.23}$$

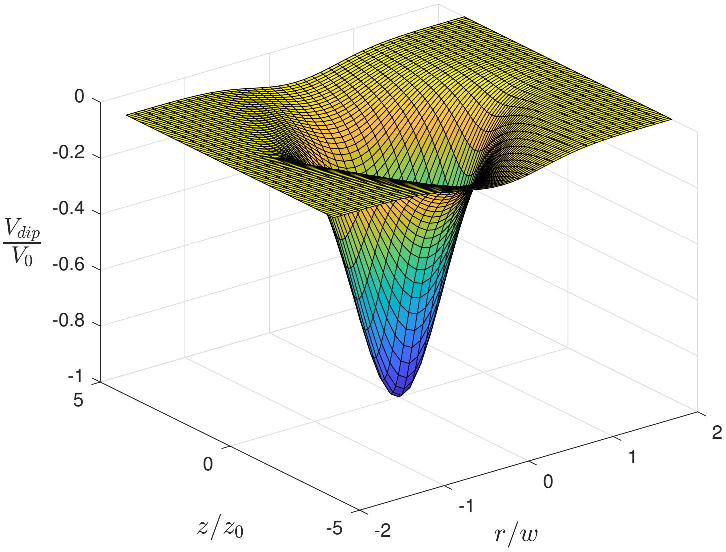

Figure 2.10: Attractive potential created by a focused laser beam propagating in z direction. Here $V_0 = 2\pi\alpha I_0/c = 654\ \mu K \times k_B$.

for a beam travelling in z direction. Here I_0 is the peak intensity, $w = 50\,\mu$m is the $1/e^2$ intensity radius and $z_0 = \pi w^2/\lambda = 741\,\mu m$ is the Rayleigh length of the focused beam with a wavelength λ. Note that experimentally $I_0 = 2P/\pi w^2$ with P being the measured power of the gaussian beam of 71 watt.

2.5.1 Far-Off-Resonance CO2 Laser

When the MOT beams are extinguished, the focused beam of a CO_2 laser, with λ_{CO_2} =10.6 μm and 140 Watt output power, produces an attractive far off resonance trap (FORT) for further cooling of the atoms through evaporation. This beam is focused to a size of 50 μm $1/e^2$ radius, creating a peak trap depth of about 50 μK. As I mentioned above, the laser is tuned far below resonance, $\omega << \omega_0$, to provide frictionless confinement while the most high energy atoms escape from the trap. To aid in efficient evaporative cooling, a magnetic field is applied to tune near the broad Feshbach resonance occurring at 832.2 Gauss ([Zürn et al., 2013]) giving us a unitary collision cross section $4\pi/k^2$ and strong interactions. Evaporation in the full power FORT cools the atoms to a temperature of $\sim 50\ \mu$K.

Further cooling of the sample is done by forced evaporation. The CO_2 beam power is lowered with an acousto-optic modulator (AOM), a device that uses an RF signal (40 MHz and 32 MHz) to generate acoustic waves in a material to diffract a laser beam, altering the intensity and frequency of diffracted modes. An artificial waveform generator provides the control voltage $V(t)$ for the AOM, giving us full control over the trap depth $U(t)$ as a function of time. Here the CO_2

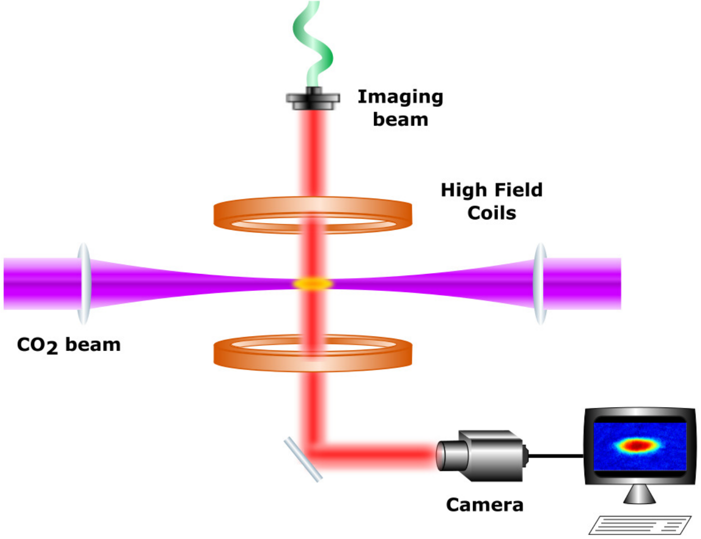

Figure 2.11: Experimental setup for evaporative cooling of ^{6}Li atoms in a CO2 optical dipole trap and absorption imaging using a resonant beam. The high field coils generate the magnetic field required for evaporative cooling at 832.2 G.

potential is gradually lowered over a few seconds to continue the evaporation process, finally cooling the atoms between 10 and 100 nK. A lowering curve is programmed into a waveform generator with user defined inputs including the lowering time and final trap depth. Lowering the CO_2 power over 9 seconds to a shallow final trap depth, $U_{final} \approx U_0 \times 10^{-3}$ ($U_0 \approx 650 \mu$K), produces an atomic sample with temperatures as low as ~ 10 nK. A typical absorption image of an atomic sample after we release it from 0.2 % to 2 % trap at the end of forced evaporation is shown in Fig 2.12.

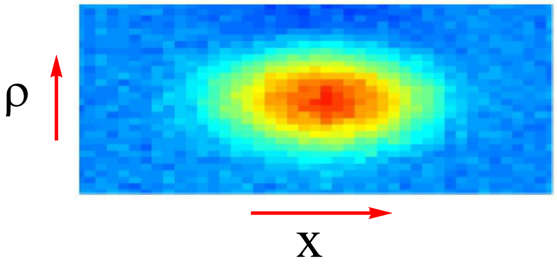

Figure 2.12: Absorption image of an atomic cloud evaporative cooled at 832 G with a low trap depth of 0.2 % and a final trap depth of 2 %. The direction of propagation of the CO2 optical beam (axial) is labeled as z. The dipole trap provides strong confinement of the the atoms in the radial direction.

We use absorption imaging to extract the density profile of the cloud. This technique uses a pulse of resonant light to image a shadow of the density distribution from the atomic cloud on a CCD camera [Ong, 2015]. This imaging process destroys the atomic sample, as the probe beam kicks the atoms out of trap and atomic sample with similar conditions will be created again.

Bias field has a curvature, produces a magnetic potential – not negligible at low trap depth. Atoms that are confined in a cigar shaped optical dipole trap at low trap depth, experience the magnetic potential from the bias coils that is comparable with the potential from the optical field. In Ch. 3 and Ch. 5, I exploit this bias field curvature to study spin dependent potential effects on a many-body system.

Chapter 3

Mean-Field Theory

In this chapter, I will explain the building blocks of mean-field model and an application to describe the evolution of the many-body spin system, in the presence of magnetic field curvature, and forward scattering interactions. I will show that for a coherent mixture of ^{6}Li hyperfine states, there is a remarkable agreement between experimental spatial spin density profiles and the model. I will show that how to include the energy dependence of the scattering length near the zero-crossing in the nondegenerate regime at higher temperatures.

3.1 Magnetic Field Curvature

We employ a mean-field model in energy representation to describe the time evolution for coherently prepared spins in the presence of magnetic field curvature. As shown in the previous chapter for two atom mixtures of ^{6}Li, a bias magnetic field tunes the s-wave scattering length near the zero crossing, where the gas is very weakly interacting and the energy changing collision rate is negligible, $0.004\ \mathrm{s}^{-1}$ for scattering length of $4\,a_0$. We begin with the single particle Hamiltonian for a noninteracting Fermi gas with two spin states, a lower hyperfine state denoted $\uparrow$ and an upper hyperfine state denoted by $\downarrow$. For an atom at rest, these states differ in energy by $\hbar\omega_{HF}$, where ω_{HF} is the hyperfine resonance frequency.

A spin-independent cigar-shaped optical trap confines the atom cloud weakly along the cigar axis, denoted x, and tightly in the perpendicular ρ direction, so that $\rho << |x|$. Curvature in the bias magnetic field produces a significant harmonic confining potential along the x-axis, while for the ρ direction, the magnetic contribution to the confining potential is negligible compared to that of the optical trap. The net optical and magnetic trapping potential along x is then spin-dependent, with harmonic oscillation frequencies $\omega_{x\uparrow}$ and $\omega_{x\downarrow}$ that gives rise to an energy dependent Zeeman-precession as shown in Fig. 3.2.

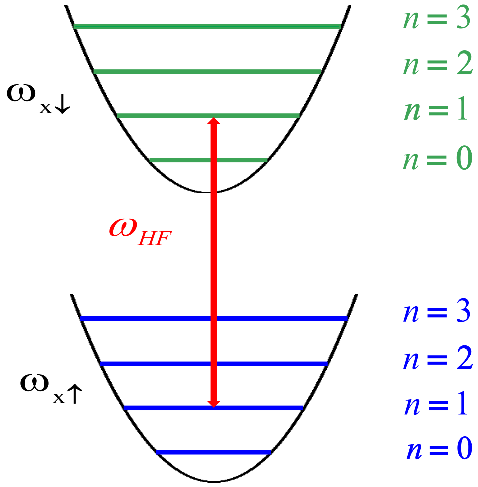

Figure 3.1: Spin-dependent harmonic potentials. An rf pulse initially creates x-polarized spins (in the rotating frame). For an rf transition between harmonic oscillator-spin states $|n,\uparrow\rangle$ and $|n,\downarrow\rangle$, the resonance frequency ω_{HF} (denoted by the red arrow) decreases with n, due to the difference in the harmonic oscillator frequencies for the two spin states.

3.1.1 Spin-Energy Correlation

The non-interacting Hamiltonian for this system (in the frame rotating at the hyperfine resonance frequency) is

$$\hat{H}_0 \;=\; \sum_n |n\rangle\langle n| \Big[(n+1/2)\,\hbar\omega_{x\uparrow} |\uparrow\rangle\langle\uparrow| + (n+1/2)\,\hbar\omega_{x\downarrow} |\downarrow\rangle\langle\downarrow| \Big]. \tag{3.1}$$

For later use, we define the dimensionless single particle spin operators,

$$\begin{aligned} s_z &= \frac{|\uparrow\rangle\langle\uparrow| - |\downarrow\rangle\langle\downarrow|}{2} \\ s_x &= \frac{|\uparrow\rangle\langle\downarrow| + |\downarrow\rangle\langle\uparrow|}{2} \\ s_y &= \frac{|\uparrow\rangle\langle\downarrow| - |\downarrow\rangle\langle\uparrow|}{2i}, \end{aligned} \tag{3.2}$$

where $[s_x, s_y] = s_x s_y - s_y s_z = i s_z$ is the cylic permutations. A radio-frequency transition that we apply to a mixture of two lowest states of two hyperfine states does not decrease the harmonic oscillator quantum number as harmonic potentials are nearly identical. Hence, the resonance frequency for a transition from the lower $\uparrow$ to the upper $\downarrow$ hyperfine state of an oscillating atom in state $|n\rangle$ is $\omega_{res} = \omega_{HF} + (n + \frac{1}{2})\,\delta\omega_x$ with $\delta\omega_x \equiv \omega_{x\downarrow} - \omega_{x\uparrow}$. Working in a frame rotating at the hyperfine resonance frequency ω_{HF} and defining the energy $E = (n + \frac{1}{2})\,\hbar\bar{\omega}_x$, where the mean oscillation frequency, $\bar{\omega}_x \equiv (\omega_{x\uparrow} + \omega_{x\downarrow})/2$, we can rewrite the Hamiltonian from Eq. 3.1

in the energy space as

$$\hat{H}_0 \;=\; \sum_E |E\rangle\langle E| \left[E(|\uparrow\rangle\langle\uparrow| + |\downarrow\rangle\langle\downarrow|) + \hbar\Omega(E)\, S_z \right], \tag{3.3}$$

where $\langle E'|E\rangle = \delta_{E',E}$ and the last term is proportional to S_z, with

$$\Omega(E) \equiv -\delta\omega_x \frac{E}{\hbar\bar{\omega}_x}. \tag{3.4}$$

In the numerical implementation section of this chapter, we derive the resonance frequency difference $\delta\omega_x$ in detail in Sec. 3.3, which arises from the curvature of the bias magnetic field in the axial direction and the difference of the magnetic moments for the ↑ and ↓ states.

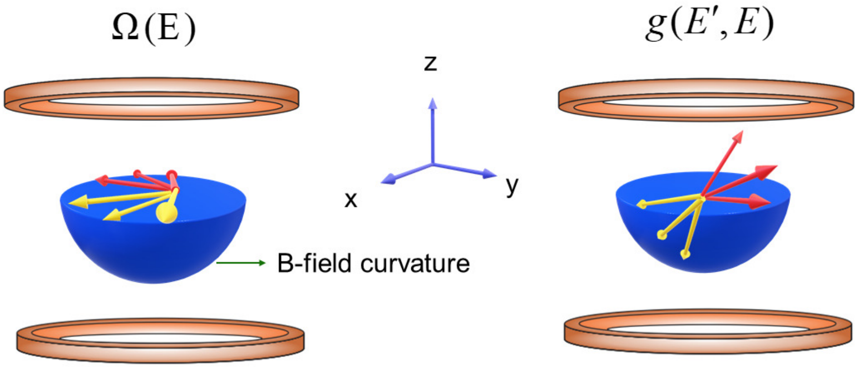

Figure 3.2: Spin segregation. The energy dependent Zeeman term, due to magnetic field curvature, causes spin vector for atoms of different energies to fan out in x-y plane (left). When coherently prepared atoms collide, due to forward s-wave scattering, the energy-dependent precession angle $\Omega(E)$ then leads to a correlation between the z component of the spin vector and the energy. As explained in the introduction, the collisional interaction results in a rotation of each atom's spin vector about the total spin vector, which is conserved $S = s_\uparrow + s_\downarrow$.

To treat the many-body problem for a very weakly interacting gas, where the single particle energies do not change during the evolution time, we define the field operator in energy representation as

$$\hat{\psi} \equiv \sum_{E,\sigma=\uparrow,\downarrow} \hat{a}_\sigma(E)\,|E\rangle|\sigma\rangle. \tag{3.5}$$

With the anticommutation relations

$$\{\hat{a}_\sigma(E), \hat{a}^\dagger_{\sigma'}(E')\} = \delta_{\sigma,\sigma'}\delta_{E,E'}, \tag{3.6}$$

we have $\{\hat{\psi}, \hat{\psi}^\dagger\} = \hat{1}$, the product of the energy and spin identity operators. The many-body Hamiltonian for the noninteracting atoms is then defined by $\hat{H}_0 = (\hat{\psi}^\dagger H_0 \hat{\psi})$, where the parenthesis (...) denotes inner products for the *single particle* energy and spin states. Then, we can write the noninteracting Hamiltonian as

$$\hat{H}_0 \;=\; \sum_{E'} E'[\hat{N}_\uparrow(E') + \hat{N}_\downarrow(E')] + \sum_{E'} \hbar\Omega(E')\,\hat{S}_z(E'). \tag{3.7}$$

Here, the number operators are $\hat{N}_\uparrow(E) = a^\dagger_\uparrow(E)a_\uparrow(E)$ and $\hat{N}_\downarrow(E) = a^\dagger_\downarrow(E)a_\downarrow(E)$ and the dimensionless many-body spin operators are given (in the Schrödinger picture) by

$$\begin{aligned}
\hat{S}_z(E) &= (\hat{\psi}^\dagger\,|E\rangle\,\langle E|\,s_z\hat{\psi}) = \frac{\hat{N}_\uparrow(E) - \hat{N}_\downarrow(E)}{2} \\
\hat{S}_x(E) &= (\hat{\psi}^\dagger\,|E\rangle\,\langle E|\,s_x\hat{\psi}) = \frac{\hat{a}^\dagger_\uparrow(E)\,\hat{a}_\downarrow(E) + \hat{a}^\dagger_\downarrow(E)\,\hat{a}_\uparrow(E)}{2} \\
\hat{S}_y(E) &= (\hat{\psi}^\dagger\,|E\rangle\,\langle E|\,s_y\hat{\psi}) = \frac{\hat{a}^\dagger_\uparrow(E)\,\hat{a}_\downarrow(E) - \hat{a}^\dagger_\downarrow(E)\,\hat{a}_\uparrow(E)}{2\,i}.
\end{aligned} \tag{3.8}$$

and the corresponding field operators in position representation are

$$\hat{\psi}(x) \;=\; (\langle x|\hat{\psi}) = \sum_{E,\sigma} \hat{a}_\sigma(E)\phi_E(x)|\sigma\rangle \equiv \sum_\sigma \hat{\psi}_\sigma(x)|\sigma\rangle. \tag{3.9}$$

Using the Eq. 3.9, we can write the Schrödinger picture operator for the z component of the spin density as

$$\begin{aligned}
\hat{S}_z(x) &= (\hat{\psi}^\dagger(x)s_z\hat{\psi}(x)) \\
&= \frac{1}{2}\sum_{E,E'} \phi^*_{E'}(x)\phi_E(x)\left[\hat{a}^\dagger_\uparrow(E')\,\hat{a}_\uparrow(E) - \hat{a}^\dagger_\downarrow(E')\,\hat{a}_\downarrow(E)\right].
\end{aligned} \tag{3.10}$$

Note that the orthonormality of the $\phi_E(x)$ yields $\int dx\hat{S}_z(x) = \sum_E \hat{S}_z(E) = \hat{S}_z$, the total z-component of the spin operator. For our mean-field treatment, we assume initially that there is no coherence between atoms with different energy, $E' \neq E$, for a thermal average, i.e.,

$\langle \hat{a}_\uparrow^\dagger(E')\hat{a}_\uparrow(E)\rangle = \langle \hat{N}_\uparrow(E)\rangle\, \delta_{E',E}$. Then the average z-component of the c-number spin density is given by

$$S_z(x,t) \equiv \langle \hat{S}_z(x,t)\rangle = \sum_E |\phi_E(x)|^2 \langle \hat{S}_z(E,t)\rangle. \tag{3.11}$$

Hence, we need only to determine $S_z(E,t)$ to predict the measured $S_z(x,t)$. In Ch. 4, I will show that this relation corresponds to an integral Abel-transform that can be inverted and provide us a useful method to study energy-resolved measurement of spins in the energy lattice.

Using the anticommutation relations of Eq. 3.6, it is easy to evaluate the elementary commutators,

$$\begin{aligned} \left[\hat{a}^\dagger_{\sigma_1'}(E_1')\,\hat{a}_{\sigma_1}(E_1), \hat{a}^\dagger_{\sigma'}(E)\right] &= \hat{a}^\dagger_{\sigma_1'}(E_1')\,\delta_{E1,E}\,\delta_{\sigma_1,\sigma'} \\ \left[\hat{a}^\dagger_{\sigma_1'}(E_1')\,\hat{a}_{\sigma_1}(E_1), \hat{a}_{\sigma}(E)\right] &= -\hat{a}_{\sigma_1}(E_1)\,\delta_{E1',E}\,\delta_{\sigma_1',\sigma}, \end{aligned} \tag{3.12}$$

which are formally identical to the results obtained for bosons. With Eq. 3.12, it is straightforward to show that the spin operators of Eq. 3.8 satisfy the usual cyclic commutation relations,

$$[\hat{S}_i(E'), \hat{S}_j(E)] = i\,\epsilon_{ijk}\,\hat{S}_k(E)\,\delta_{E',E}. \tag{3.13}$$

With the non-interating Hamiltonian in Eq. 3.7, the Heisenberg operator equations for the collisionless spin evolution are then

$$\frac{\partial \hat{\mathbf{S}}(E,t)}{\partial t} = \frac{i}{\hbar}\left[\hat{H}_0, \hat{\mathbf{S}}(E,t)\right] = \mathbf{\Omega}(E,t) \times \hat{\mathbf{S}}(E,t), \tag{3.14}$$

where the Zeeman term as it is shown in Fig. 3.2, is along the z-axis

$$\mathbf{\Omega}(E) = \hat{e}_z \Omega(E) \tag{3.15}$$

and $\Omega(E)$ is given by Eq. 3.4. For sample preparation using radio frequency excitation, Eq. 3.15 is readily generalized to include a time dependent Rabi frequency rotation rate $\Omega_R(t)\,\hat{e}_y$ that allows us to create the coherent sample of atoms and an additional time dependent detuning term $\Delta(t)\,\hat{e}_z$, with $\Delta = \omega(t) - \omega_{HF}$ in the rotating frame. Thus, the energy-dependent precession in the more general form can be written as,

$$\mathbf{\Omega}(E) = (\Omega(E) + \Delta)\hat{e}_z + \Omega_R\,\hat{e}_y \tag{3.16}$$

3.2 Interaction Hamiltonian

Next, we consider collisional s-wave scattering interactions, which are dominant at low temperature regime. Short range scattering is modeled by a contact interaction between spin-up and spin-down atoms with an s-wave scattering length a_S,

$$H'(\mathbf{x}_1-\mathbf{x}_2)=\frac{4\pi\hbar^2 a_S}{m}\,\delta(\mathbf{x}_1-\mathbf{x}_2)\equiv g\,\delta(\mathbf{x}_1-\mathbf{x}_2). \tag{3.17}$$

For the many-body system the Hamiltonian operator yields,

$$\begin{aligned}\hat{H}' &= \int\frac{d^3\mathbf{x}_1 d^3\mathbf{x}_2}{2}\left(\hat{\psi}^\dagger(\mathbf{x}_2)\hat{\psi}^\dagger(\mathbf{x}_1)H'(\mathbf{x}_1-\mathbf{x}_2)\hat{\psi}(\mathbf{x}_1)\hat{\psi}(\mathbf{x}_2)\right)\\ &= g\int d^3\mathbf{x}\,\hat{\psi}^\dagger_\uparrow(\mathbf{x})\hat{\psi}^\dagger_\downarrow(\mathbf{x})\hat{\psi}_\downarrow(\mathbf{x})\hat{\psi}_\uparrow(\mathbf{x}),\end{aligned} \tag{3.18}$$

where the factor 1/2 avoids double counting and $\hat{\psi}^2_{\uparrow,\downarrow}(\mathbf{x})=0$. For simplicity, we initially neglect the dependence of a_S on the relative kinetic energy of the colliding pair, which will be included later.

3.2.1 Mean-field interaction

As mentioned earlier, the atoms are confined in a cigar-shaped cloud, where the x dimension is large compared to the radial dimension ρ, so that the bias field curvature is negligible along the ρ direction. Therefore, we treat the problem as one-dimensional by taking the field operators to be of the form,

$$\hat{\psi}_\sigma(\mathbf{x})=\phi(\rho)\,\hat{\psi}_\sigma(x), \tag{3.19}$$

Carrying out the ρ integration in Eq. 3.18, we determine the effective one-dimensional interaction Hamiltonian,

$$\hat{H}'=\tilde{g}\int dx\,\hat{\psi}^\dagger_\uparrow(x)\hat{\psi}^\dagger_\downarrow(x)H'\hat{\psi}_\downarrow(x)\hat{\psi}_\uparrow(x). \tag{3.20}$$

where $\tilde{g}\equiv g\,\bar{n}_\perp$ and

$$\bar{n}_\perp=\int 2\pi\rho d\rho\,[n_\perp(\rho)]^2. \tag{3.21}$$

Here, we have let $|\phi(\rho)|^2\to n_\perp(\rho)$, where $\int 2\pi\rho d\rho\, n_\perp(\rho)=1$. Eq. 3.21 determines an effective mean transverse density, $\bar{n}_\perp$, as a fraction per unit transverse area. Using Eq. 3.9, Hamiltonian operator of Eq. 3.20 takes the form

$$\begin{aligned}\hat{H}' &= \tilde{g} \sum_{E_1,E_2,E_1',E_2'} \int dx\, \phi^*_{E_1'}(x)\phi^*_{E_2'}(x)\phi_{E_2}(x)\phi_{E_1}(x) \\ &\qquad \times \hat{a}^\dagger_\uparrow(E_1')\hat{a}^\dagger_\downarrow(E_2')\hat{a}_\downarrow(E_2)\hat{a}_\uparrow(E_1). \end{aligned} \tag{3.22}$$

We simplify the interaction Hamiltonian by using a mean field approximation to evaluate

$$\langle \hat{a}^\dagger_\uparrow(E_1')\hat{a}^\dagger_\downarrow(E_2')\hat{a}_\downarrow(E_2)\hat{a}_\uparrow(E_1)\rangle. \tag{3.23}$$

where $\langle ... \rangle$ denotes a thermal averaged operator products. To calculate the Eq. 3.23, we used the Wick's theorem, which expresses a product of fields as a sum of several terms, each term is a product of contractions of pairs of fields and normal ordered products of remaining fields.

3.2.2 Wick's theorem

For an arbitrary choice of operators as b_1, b_2, b_3, b_4, according to Wick's theorem, we have,

$$\langle b_1\ b_2\ b_3\ b_4\rangle = \langle b_1\ b_2\rangle\langle b_3\ b_4\rangle \mp \langle b_1\ b_3\rangle\langle b_2\ b_4\rangle + \langle b_1\ b_4\rangle\langle b_2\ b_3\rangle. \tag{3.24}$$

Here the negative sign is for the case of Fermion particles and the positive sign is for Bosons. Using Eq. 3.24, we can write the average of the field operator Eq. 3.22 as,

$$\begin{aligned}\langle \psi^\dagger_\uparrow\ \psi^\dagger_\downarrow\ \psi_\downarrow\ \psi_\uparrow\rangle &= \langle \psi^\dagger_\uparrow\ \psi_\uparrow\ \psi^\dagger_\downarrow \psi_\downarrow\rangle \mp \langle \psi^\dagger_\uparrow\ \psi_\downarrow\rangle\langle \psi^\dagger_\downarrow\ \psi_\uparrow\rangle \\ &+ \langle \psi^\dagger_\uparrow\ \psi^\dagger_\downarrow\rangle\langle \psi_\downarrow\ \psi_\uparrow\rangle. \end{aligned} \tag{3.25}$$

The first term on the right side is the product of number operator and the second term is responsible for interaction between the atoms of opposite spins, where causes spin segregation as will be shown in Ch. 5. The last term produces the BCS-gap energy which we assume vanishes for our weakly interacting system. If we apply the Wick's theorem on the average of field operators up to first order fluctuation, we obtain,

$$\begin{aligned}\hat{O}' \simeq\ & \langle \hat{a}^\dagger_\uparrow(E_1')\,\hat{a}_\uparrow(E_1)\rangle\,\hat{a}^\dagger_\downarrow(E_2')\,\hat{a}_\downarrow(E_2) + \langle\,\hat{a}^\dagger_\downarrow(E_2')\,\hat{a}_\downarrow(E_2)\rangle\,\hat{a}^\dagger_\uparrow(E_1')\,\hat{a}_\uparrow(E_1) \\ & -\langle\,\hat{a}^\dagger_\uparrow(E_1')\,\hat{a}_\downarrow(E_2)\rangle\,\hat{a}^\dagger_\downarrow(E_2')\,\hat{a}_\uparrow(E_1) - \langle \hat{a}^\dagger_\downarrow(E_2')\,\hat{a}_\uparrow(E_1)\rangle\,\hat{a}^\dagger_\uparrow(E_1')\,\hat{a}_\downarrow(E_2). \end{aligned} \tag{3.26}$$

Further, we will require a thermal average of the Heisenberg equations of motion as well, i.e., $\langle[\hat{O}', \hat{S}_i(E)]\rangle$. This will vanish unless the energy arguments in the operator factors are the same.

Hence, the interaction Hamiltonain can be rewritten as,

$$\begin{aligned}\hat{H}' &= \tilde{g}\sum_{\tilde{E},E'}\int dx\,|\phi_{E'}(x)|^2|\phi_{\tilde{E}}(x)|^2 \times \Big\{\langle\hat{a}^\dagger_\uparrow(E')\,\hat{a}_\uparrow(E')\rangle\,\hat{a}^\dagger_\downarrow(\tilde{E})\,\hat{a}_\downarrow(\tilde{E}) + \langle\hat{a}^\dagger_\downarrow(E')\,\hat{a}_\downarrow(E')\rangle\,\hat{a}^\dagger_\uparrow(\tilde{E})\,\hat{a}_\uparrow(\tilde{E}) \\ &\quad -\langle\hat{a}^\dagger_\uparrow(E')\,\hat{a}_\downarrow(E')\rangle\,\hat{a}^\dagger_\downarrow(\tilde{E})\,\hat{a}_\uparrow(\tilde{E}) - \langle\hat{a}^\dagger_\downarrow(E')\,\hat{a}_\uparrow(E')\rangle\,\hat{a}^\dagger_\uparrow(\tilde{E})\,\hat{a}_\downarrow(\tilde{E})\Big\}. \qquad (3.27)\end{aligned}$$

With the collective spin operators, Eq. 3.8, we rewrite Eq. 3.27 as

$$\hat{H}' = 2\,\tilde{g}\sum_{\tilde{E},E'}\int dx\,|\phi_{E'}(x)|^2|\phi_{\tilde{E}}(x)|^2 \times \Big\{\frac{1}{4}N(E')\,\hat{N}(\tilde{E}) - \mathbf{S}(E')\cdot\hat{\mathbf{S}}(\tilde{E})\Big\}, \qquad (3.28)$$

where $\hat{N}(\tilde{E}) = \hat{N}_\uparrow(\tilde{E}) + \hat{N}_\downarrow(\tilde{E})$ is the total number operator and $\hat{\mathbf{S}}(\tilde{E})$ is the total spin vector operator for atoms of energy $\tilde{E}$. $N(E')$ is a c-number scalar and $\mathbf{S}(E')$ is a c-number vector, i.e., the corresponding thermal averaged Heisenberg operators for energy E'.

To evaluate the collisional contribution of the Heisenberg equations of motion, we require $[\hat{H}', \hat{\mathbf{S}}(E)]$. Here, $[\hat{N}(\tilde{E}), \hat{\mathbf{S}}(E)] = 0$, and using Eq. 3.13, $[\mathbf{S}(E')\cdot\hat{\mathbf{S}}(\tilde{E}), \hat{\mathbf{S}}(E)] = -i\,\mathbf{S}(E')\times\hat{\mathbf{S}}(\tilde{E})\,\delta_{\tilde{E},E}$. With Eq. 3.14, the Heisenberg equation $\dot{\hat{\mathbf{S}}}(E,t) = \frac{i}{\hbar}\left[\hat{H}_0 + \hat{H}', \hat{\mathbf{S}}(E,t)\right]$ for the spin vector operator of energy E takes the simple form,

$$\frac{\partial\hat{\mathbf{S}}(E,t)}{\partial t} = \mathbf{\Omega}(E,t)\times\hat{\mathbf{S}}(E,t) + \sum_{E'} g(E',E)\,\mathbf{S}(E',t)\times\hat{\mathbf{S}}(E,t), \qquad (3.29)$$

the result of this evolution was shown in Fig. 3.2. The second term describes the rotation of the spin vector for atoms of energy E arising from collisions with atoms of energy $E^{'}$. Here, the coupling matrix $g(E,E^{'})$ is proportional to the mean-field frequency and plays the role of the site-to-site coupling in a lattice model. Below, you will see in details how $g(E,E^{'})$ is related to the mean-field frequency.

In Eq. 3.29,

$$g(E',E) = -\frac{2\,g\,\bar{n}_\perp}{\hbar}\,I(E',E), \qquad (3.30)$$

where $I(E',E)$ is the probability densities for colliding atoms of energies E and E',

$$I(E',E) \equiv \int dx\,|\phi_{E'}(x)|^2|\phi_E(x)|^2, \qquad (3.31)$$

with $\bar{n}_\perp$ given by Eq. 3.21, and $g = 4\pi\hbar^2\,a_S/m$.

For our experiments in the weakly interacting regime, where the energy $E >> \hbar\bar{\omega}_x$, $|\phi_E(x)|^2$

can be evaluated by the WKB approximation,

$$|\phi_E(x)|^2 \simeq \frac{\Theta[a(E)-|x|]}{\pi\sqrt{a^2(E)-x^2}}, \tag{3.32}$$

where $a(E) = \sqrt{2E/(m\bar{\omega}_x^2)}$ is the classical turning point and Θ is a Heaviside function. Then, the x-integral in Eq. 3.31 takes the form of

$$I(E',E) = \frac{1}{\pi^2 a_{min}} \int_{-1}^{1} \frac{du}{\sqrt{\left[\frac{E}{E_{min}} - u^2\right]\left[\frac{E'}{E_{min}} - u^2\right]}}, \tag{3.33}$$

where we have taken $x = u\, a_{min}$. Here, $a_{min} = \sqrt{2E_{min}/(m\bar{\omega}_x^2)}$ determines the overlap region, with E_{min} the minimum of E, E'. Using $u = \sin\theta$, and by considering separately the cases $E_{min} = E < E'$ and $E_{min} = E' < E$, we obtain,

$$I(E',E) = \frac{1}{\pi^2}\sqrt{\frac{m\bar{\omega}_x^2}{2|E-E'|}} \int_{-\pi/2}^{\pi/2} \frac{d\theta}{\sqrt{1 + \frac{E_{min}}{|E-E'|}\cos^2\theta}}. \tag{3.34}$$

The integral is readily evaluated, yielding a closed form EllipticK [Abramowitz et al., 1988] as,

$$g(E',E) \quad = \quad -\frac{4\,g\,\bar{n}_\perp}{\pi^2\hbar}\sqrt{\frac{m\bar{\omega}_x^2}{2|E-E'|}} \times \text{EllipticK}\left[-\frac{E_{min}}{|E-E'|}\right] \tag{3.35}$$

where,

$$Elliptic\mathrm{K}(m) \equiv \int_0^{\frac{\pi}{2}} \frac{d\theta}{(1 - m\cos^2(\theta))^{\frac{1}{2}}} \tag{3.36}$$

with $m = -E_{\text{min}}/\,|E-E'|$, and $E' \neq E$, since the sum in the last term of Eq. 3.29 vanishes for $E' = E$, i.e., we can take $g(E' = E, E) = 0$ in Eq. 3.29. $g(E' = E, E)$ determines the effective long-range character of the spin couplings as $g(E',E) \propto 1/\sqrt{E-E'}$, which is a consequence of the separation of time scales for the fast harmonic oscillation of atoms and slow macroscopic spin-density evolution [Koller et al., 2016, Pegahan et al., 2019].

Taking the thermal average of the evolution equations, we replace the vector operators by the c-number vectors $\mathbf{S}(E,t) \equiv \langle\hat{\mathbf{S}}(E,t)\rangle$. Since $E >> \hbar\bar{\omega}_x$, we evaluate Eq. 3.29 in the continuum limit. We replace the sum $\sum'_E \equiv \sum'_n$ by $\int \frac{dE'}{\hbar\bar{\omega}_x}$ and define

$$\frac{\mathbf{S}(E,t)}{\hbar\bar{\omega}_x} \equiv \frac{N}{2}\tilde{\mathbf{S}}(E,t), \tag{3.37}$$

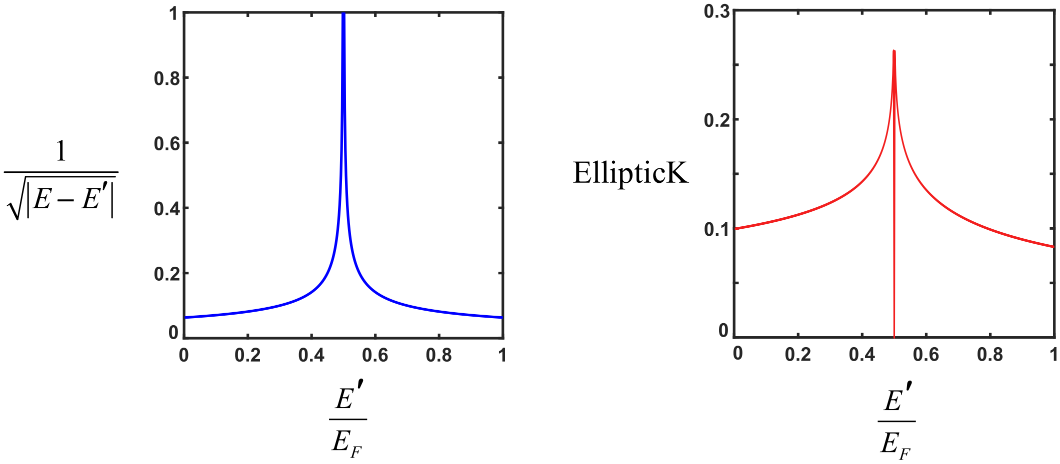

Figure 3.3: Dependence of $g(E',E)$ to $\frac{1}{\sqrt{|E-E'|}}$ multiplier and EllipticK function for $E=\frac{E_F}{2}$.

where $N = N_\uparrow + N_\downarrow$ is the total number of atoms. Then,

$$\frac{\partial\tilde{\mathbf{S}}(E,t)}{\partial t} = \boldsymbol{\Omega}(E,t)\times\tilde{\mathbf{S}}(E,t) + \int dE'\,\tilde{g}(E',E)\,\tilde{\mathbf{S}}(E',t)\times\tilde{\mathbf{S}}(E,t), \tag{3.38}$$

where $\tilde{g}(E',E) \equiv \frac{N}{2}\,g(E',E)$ has a dimension of s^{-1}. Note that here, the factor $N/2$ in Eq. 3.37 is defined to be consistent with the spin operators of Eq. 3.8, i.e., with all atoms in the ground hyperfine state with spin ↑, the total spin in the z-direction is $N/2$.

The integral term in Eq. 3.38 conserves the total spin vector $\int dE\,\tilde{\mathbf{S}}(E,t)$, since $\tilde{g}(E,E')$ is symmetric under $E' \leftrightarrow E$ and the cross product is antisymmetric. In contrast, $\boldsymbol{\Omega}(E)$ is an energy dependent rotation rate that does not conserve the total spin $\tilde{\mathbf{S}}(E,t)$. However, without radio frequency excitation, $\boldsymbol{\Omega}(E)$ is along the z-axis and the z-component of the total spin $\int dE\,\tilde{S}_z(E)$ is conserved. Since Eq. 3.38 describes a rotation of $\tilde{\mathbf{S}}(E,t)$, $\tilde{S}(E,t)\cdot\tilde{S}(E,t)=0$ and $|\tilde{\mathbf{S}}(E,t)| \equiv S(E)$ is conserved for each E.

As it will be shown in more detail in Ch. 5, we integrate Eq. 3.38 subject to the initial condition that all atoms are in the upper hyperfine (spin-down) state. A radio frequency pulse is then used to prepare a collective spin vector with components in the $x-y$ plane. With Eq. 3.37, the thermal averaged z-component of the initial collective spin operator, Eq. 3.8, requires

$$\tilde{S}_z(E,t=0) = S(E) = P(E), \tag{3.39}$$

where $P(E,T)$ is the fraction of atoms with an axial energy E at temperature T and

$$\int_0^\infty dE\, P(E) = 1 \tag{3.40}$$

in the continuum limit. In the high T imit that we normally work with,

$$P(E) = \frac{1}{Z}\, e^{-\frac{E}{k_B T}}, \tag{3.41}$$

where the partition function $Z = \int_0^\infty dE e^{-\frac{E}{k_B T}} = k_B T$. In the low temperature limit, $T \to 0$, we use the occupation number for a Fermi distribution in three dimensions and sum over the energies in the two perpendicular directions to obtain the normalized axial (x) energy distribution as

$$P(E) = \frac{3}{E_F}\left(1 - \frac{E}{E_F}\right)^2 \Theta\left(1 - \frac{E}{E_F}\right), \tag{3.42}$$

where for $N_\uparrow = N$, $E_F = (6N)^{1/3}\hbar\bar{\omega}$, with $\bar{\omega} \equiv (\omega_\perp^2 \bar{\omega}_x)^{1/3}$.

The measured axial spin density profiles, shown in Ch 5, are given by the continuum limit of Eq. 3.11,

$$\mathbf{S}(x,t) = \frac{N}{2}\int dE\, |\phi_E(x)|^2\, \tilde{\mathbf{S}}(E,t), \tag{3.43}$$

where we neglect coherence between states of different energy and $\int dx\, \mathbf{S}(x,t) = \frac{N}{2}\int dE\, \tilde{\mathbf{S}}(E,t)$. Evaluation of Eq. 3.43 is simplified by rewriting the WKB wave functions of Eq. 3.32 in the form,

$$|\phi_E(x)|^2 = \frac{\bar{\omega}_x}{\pi}\int_0^\infty dp_x\, \delta\left(E - \frac{p_x^2}{2m} - \frac{m\bar{\omega}_x^2}{2}x^2\right) \tag{3.44}$$

so that the spin density is

$$\mathbf{S}(x,t) = \frac{N}{2}\frac{\bar{\omega}_x}{\pi}\int_0^\infty dp_x\, \tilde{\mathbf{S}}\left(\frac{p_x^2}{2m} + \frac{m\bar{\omega}_x^2}{2}x^2, t\right). \tag{3.45}$$

The initial $t = 0$ spatial densities for the spin components are similarly determined. For the degenerate gas, we approximate the energy distribution by the zero temperature limit in Eq. 3.42, as discussed above. The corresponding spatial density for each spin component, just after preparation, is then a normalized zero temperature Thomas-Fermi profile. Analogous to Eq. 3.43, using the WKB approximation, and Eq. 3.42 it is easy to show that the initial density profiles for each state are of the one dimensional Thomas-Fermi form,

$$\begin{aligned} n_{\uparrow,\downarrow}(x,0) &= N_{\uparrow,\downarrow}\int dE\,|\phi_E(x)|^2\,P(E) \\ &= N_{\uparrow,\downarrow}\,\frac{16}{5\pi\,\sigma_{Fx}}\left(1-\frac{x^2}{\sigma_{Fx}^2}\right)^{5/2}\Theta\left(1-\frac{x^2}{\sigma_{Fx}^2}\right), \end{aligned} \tag{3.46}$$

where $\sigma_{Fx}=\sqrt{2E_F/(m\bar{\omega}_x^2)}$ is the Fermi radius and $N_\uparrow = N_\downarrow = N/2$ for a balanced mixture. As the energy distribution for the atoms does not change in time, the spatial profile for the total density $n(x)$ is time independent, i.e., $n_\uparrow(x,t)+n_\downarrow(x,t) = n_\uparrow(x,0)+n_\downarrow(x,0) = n(x)$, as shown later in Fig. 5.3. For the non-degenerate gas, the Maxwell-Boltzmann energy distribution of Eq. 3.41 yields the corresponding gaussian spatial profile.

3.2.3 Numerical Implementation

To determine $\tilde{\mathbf{S}}(E,t)$ from Eq. 3.38, we divide the energy range into discrete intervals ΔE, taking $E=(n-1)\Delta E$, with n an integer, $1\le n\le n_{\rm max}$. Typically, $n_{max}=500$. This method determines the spin components $i=x,y,z$ as column vectors in discrete energy space, $\tilde{S}_i^{\rm discr}(n,t)$, where n labels the row rather than the harmonic oscillator state.

We take $\tilde{\mathbf{S}}(E,t)=\tilde{\mathbf{S}}^{\,\rm discr}(n,t)/\Delta E$ in Eq. 3.38. With the replacement $\int dE'/\Delta E = \int dn' \to \sum_{n'}$, the discrete energy evolution equations are

$$\frac{\partial \tilde{\mathbf{S}}^{\,\rm discr}(n,t)}{\partial t} \;=\; \mathbf{\Omega}(n,t)\times\tilde{\mathbf{S}}^{\,\rm discr}(n,t)\sum_{n'}\tilde{g}(n',n)\,\tilde{\mathbf{S}}^{\,\rm discr}(n',t)\times\tilde{\mathbf{S}}^{\,\rm discr}(n,t), \tag{3.47}$$

where

$$\tilde{g}(n',n)=\frac{\tilde{\Omega}}{\sqrt{|n-n'|}}\;\text{EllipticK}\left[-\frac{n_{min}-1}{|n-n'|}\right]. \tag{3.48}$$

$\tilde{g}(n',n)$'s behavior is shown in Fig. 3.3. Here, n_{min} is the minimum of n and n' and

$$\tilde{\Omega}=-\frac{N}{2}\frac{4\,g\,\bar{n}_\perp}{\pi^2\hbar}\sqrt{\frac{m\bar{\omega}_x^2}{2\Delta E}}, \tag{3.49}$$

with $g=4\pi\hbar^2\,a_S/m$.

We define ΔE differently for the high and low temperature limits. In the low temperature limit, we take $\Delta E = s\,E_F$ with $E=(n-1)\;s\;E_F$, and $0\le E\le E_F$, we have $s=1/(n_{\rm max}-1)$. In the high temperature limit, we choose $\Delta E = s\,k_BT$ and take s such that $\exp[-s\,(n_{\rm max}-1)]$ is negligible. For both cases, it is convenient to let $\Delta E = s\,\frac{1}{2}m\bar{\omega}_x^2\sigma_x^2$. Then, for $T=0$, $\sigma_x = \sqrt{2E_F/(m\bar{\omega}_x^2)}\equiv\sigma_{Fx}$ is the Fermi radius, which is measured in the experiments. For the high temperature limit, $\sigma_x=\sqrt{2k_BT/(m\bar{\omega}_x^2)}$ is the measured gaussian (Boltzmann factor) $1/e$

radius. With $\Delta E = s\,\frac{1}{2}m\bar{\omega}_x^2\sigma_x^2$, Eq. 3.49 yields

$$\tilde{\Omega} = -\frac{1}{\sqrt{s}}\frac{4\,h}{\pi^2}\frac{a_S}{m}\frac{\bar{n}_\perp N}{\sigma_x} \equiv -\frac{1}{\sqrt{s}}\,\Omega_{MF}, \tag{3.50}$$

where we have defined the mean field frequency Ω_{MF}, $h = 2\pi\hbar$, and $\bar{n}_\perp$ given by Eq. 3.21. In the low temperature limit, with $n_\perp(\rho) = 3(1-\rho^2/\sigma_{F\perp}^2)/(\pi\sigma_{F\perp}^2)$, we obtain $\bar{n}_\perp = \frac{9}{5\pi\sigma_{F\perp}^2}$. In the high temperature limit, with $n_\perp(\rho) = \exp[-\rho^2/\sigma_\perp^2]/(\pi\sigma_\perp^2)$, we obtain $\bar{n}_\perp = \frac{1}{2\pi\sigma_\perp^2}$. Then the mean field frequency in these two regimes are,

$$\begin{aligned}\Omega_{MF} &= \frac{9}{20\pi}\frac{2h\,a_S}{m}\,n_{F0} \qquad T=0\\ \Omega_{MF} &= \frac{1}{\pi^{3/2}}\frac{2h\,a_S}{m}\,n_0 \qquad \text{High } T.\end{aligned} \tag{3.51}$$

Here $n_{F0} = 8\,N/(\pi^2\sigma_{F\perp}^2\sigma_{Fx})$ is the 3D central density for a $T=0$ Thomas-Fermi profile with $\sigma_{F\perp} = \sqrt{2E_F/(m\omega_\perp^2)}$ and $n_0 = N/(\pi^{3/2}\sigma_\perp^2\sigma_x)$ is the 3D central density in the Boltzmann limit, where $\sigma_\perp = \sqrt{2k_BT/(m\omega_\perp^2)}$.

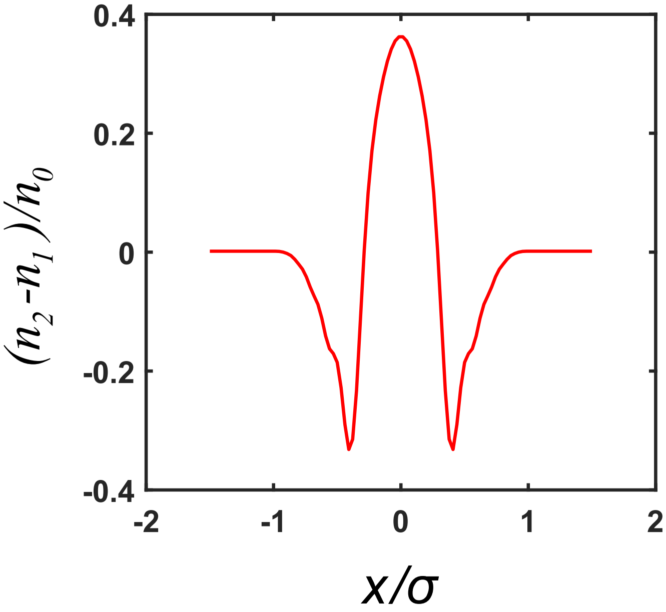

Figure 3.4: Low-temperature z component spin-density profile of 1-2 mixture for $t=$ 600 ms, $T/T_F = 0.35$, and $a = 3.1\ a_0$.

Using the measured experimental parameters of Ch. 5, we can easily calculate the mean field frequency of Eq. 3.51 and compare that with the energy dependent Zeeman precession of Eq. 3.4. For the degenerate gas $\Omega_{MF} = 1Hz$ with $a = 5.2a_0$, for the thermal gas $\Omega_{MF} = 0.5Hz$, and for the Zeeman precession rate is from $0Hz$ to $12Hz$, which depends on the energy of spins prepared along the x-axis on the Bloch sphere. The Zeeman detuning rate, Ω_z, for the average energy of degenerate atomic cloud, $\bar{E} = E_F/4$, is $3Hz$. For the degenerate gas, the average of the mean field frequency is $< g(n, n') >=< \frac{\tilde{\Omega}}{\sqrt{s}} \frac{EllipicK(n,n')}{\sqrt{n-n'}} >= 3.78\,\Omega_{MF}$, and for the Boltzman gas $< g(n, n') >= 1.97\,\Omega_{MF}$.

With our choices of ΔE, the initial conditions are analogous to Eq. 3.39,

$$\tilde{S}_z^{\text{discr}}(n, t = 0) = P(n), \tag{3.52}$$

where for the high temperature limit, $P(n) = \exp[-s(n-1)]/Z$, and for the $T = 0$ limit, $P(n) = 3s\,[1 - s(n-1)]^2/Z$, with $Z = \sum_{n=1}^{n_{\max}} P(n)$.

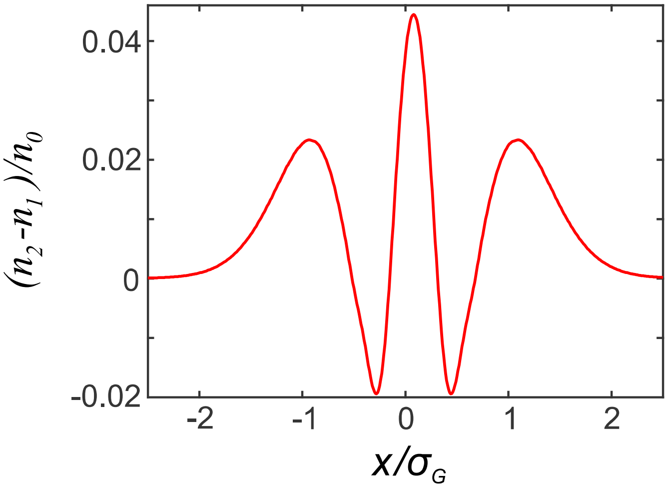

Figure 3.5: High-temperature spin-density profile for 1-2 mixture for $t = 400\ ms$. $T = 45.7\ \mu K$ and B $= 527.466\ G$, and the zero-energy s-wave scattering in this regime is 0.90 Bohr.

Numerical evaluation of Eq. 3.47 yields the tables $\{n-1, \tilde{S}_i^{\text{discr}}(n, t)\}$ for $1 \leq n \leq n_{\max}$. Note that $n-1$ is used as the independent variable so that $E = (n-1)\Delta E = 0$ for $n = 1$. The energy-dependent $\tilde{\mathbf{S}}^{\text{discr}}(n, t)$ is then converted to an interpolator function of $(n-1) = E/\Delta E$ and we use Eq. 3.45 to find the spin density $\mathbf{S}(x, t)$.

3.3 Spin-Dependence Harmonic Oscillation Frequency

Now that we explained thoroughly the method to evaluate the Eq. 3.47, here we will focus in more details on the first term that gives rise to energy dependent spin precession.

$$\boldsymbol{\Omega}(n) = \hat{e}_z\,\Omega_z(n). \tag{3.53}$$

As discussed above, $\Omega_z(n)$ arises from the bias magnetic field curvature. Using $E = (n-1)s\,E_F$ for the $T = 0$ limit (degenerate regime) and $E = (n-1)s\,k_BT$ in the high temperature limit,

$$\Omega_z(n) \equiv \Omega_z\,(n-1), \tag{3.54}$$

where $\Omega_z = -\delta\omega_x\,s\,E_F/(\hbar\bar{\omega}_x)$ for $T = 0$ and $\Omega_z = -\delta\omega_x\,s\,k_BT/(\hbar\bar{\omega}_x)$ in the high temperature limit.

As the magnetic moments of the two spins are not identical, the bias magnetic field in the axial x direction, which arises from the curvature of $\Delta B_z = x^2\,B_z''(0)/2$, leads to a resonance frequency difference between two lowest hypefine spin states, $\delta\omega_x = \omega_{x\downarrow} - \omega_{x\uparrow}$. The harmonic oscillation frequencies for the upper hyperfine state ($\downarrow$) and lower hyperfine state ($\uparrow$) are determined by the sum of optical and magnetic spring constants,

$$\omega_{x\downarrow,\uparrow}^2 = \omega_{\text{opt}}^2 + \omega_{\text{mag}\downarrow,\uparrow}^2 = \omega_{\text{opt}}^2 + \frac{1}{m}\frac{\partial^2 B_z}{\partial x^2}\frac{\partial E_{\downarrow,\uparrow}}{\partial B}, \tag{3.55}$$

where ω_{opt} arises from the optical trap and ω_{mag} from the bias field curvature. The last term in the Eq. 3.55 is the result of,

$$\frac{1}{2}m\omega_{\text{mag}\downarrow,\uparrow}^2 x^2 = \Delta B\mu = \frac{x^2}{2}\frac{\partial^2 B}{\partial x^2}\frac{\partial E_{\uparrow,\downarrow}}{\partial B}. \tag{3.56}$$

For our experiments in ^{6}Li, the hyperfine energies $E_{\downarrow,\uparrow}$ are dominated by the Zeeman shift of the (spin down) electron for each of the lowest three hyperfine states, while the much smaller difference $E_\downarrow - E_\uparrow$ arises from the difference between the nuclear parts of the magnetic moment and the difference in the hyperfine mixing. Then, with $\omega_{\text{mag}}^2 \equiv (\omega_{\text{mag}\downarrow}^2 + \omega_{\text{mag}\uparrow}^2)/2$ and $\bar{\omega}_x^2 \equiv \omega_{\text{opt}}^2 + \omega_{\text{mag}}^2$, we have

$$\omega_{x\downarrow,\uparrow} \;=\; \sqrt{\omega_{\text{opt}}^2 + \omega_{\text{mag}}^2 \pm \frac{\omega_{\text{mag}\downarrow}^2 - \omega_{\text{mag}\uparrow}^2}{2}} \simeq \bar{\omega}_x\left(1 \pm \frac{\omega_{\text{mag}\downarrow}^2 - \omega_{\text{mag}\uparrow}^2}{4\,\bar{\omega}_x^2}\right) \tag{3.57}$$

and

$$\frac{\delta\omega_x}{\bar{\omega}_x} = \frac{\omega_{x\downarrow} - \omega_{x\uparrow}}{\bar{\omega}_x} = \frac{\omega_{\text{mag}}^2}{\bar{\omega}_x^2}\;\frac{\omega_{\text{mag}\downarrow}^2 - \omega_{\text{mag}\uparrow}^2}{2\,\omega_{\text{mag}}^2}.$$

Then,

$$\delta\omega_x = \frac{\omega_{\text{mag}}^2}{\bar{\omega}_x}\left(\frac{\frac{\partial E_\downarrow}{\partial B} - \frac{\partial E_\uparrow}{\partial B}}{\frac{\partial E_\downarrow}{\partial B} + \frac{\partial E_\uparrow}{\partial B}}\right) \simeq \frac{\omega_{\text{mag}}^2}{\bar{\omega}_x}\frac{\hbar\omega'_{\downarrow\uparrow}}{g_J\mu_B}, \tag{3.58}$$

where $\omega'_{\downarrow\uparrow}$ is the tuning rate of the transition, with $\downarrow$ the *upper* hyperfine state. Here, we have assumed that the denominator of Eq. 3.58 is approximately twice the Zeeman tuning rate of a spin-down electron, $2\times g_J\mu_B/2 = -2\pi\times 2.8$ MHz/G, as is the case for our experiments near the zero crossings of ^{6}Li. For our experiments, $\omega_{\text{mag}}^2 = (2\pi\times 20.5\,\text{Hz})^2\,\text{B(G)}/834$. For the degenerate gas, $\bar{\omega}_x = 2\pi\times 23$ Hz, $\omega_\perp = 2\pi\times 625$ Hz; for the high temperature gas, $\bar{\omega}_x = 2\pi\times 174$ Hz, $\omega_\perp = 2\pi\times 5.77$ kHz.

For a mixture of the two lowest hyperfine states, as noted above, $\downarrow$ denotes the upper hyperfine state, and $\uparrow$ denotes the lower hyperfine state. The hyperfine energies for the three lowest states of ^{6}Li, denoted $1, 2, 3$ in order of increasing energy, yield the tuning rates which appear in the numerator of Eq. 3.58: $\omega'_{21}[527\text{G}] = 2\pi\times 3.61$ kHz/G and $\omega'_{32}[589\text{G}] = -2\pi\times 12.3$ kHz/G, $\omega'_{31}[568\text{G}] = -2\pi\times 10.3$ kHz/G. With $\bar{\omega}_x = 2\pi\times 23$ Hz, we obtain $\delta\omega_x = -2\pi\times 14.9$ mHz. For a $1-2$ mixture near 527 G, $\delta\omega_x = +2\pi\times 56.7$ mHz for a $2-3$ mixture near 589 G, and $\delta\omega_x = +2\pi\times 45.8$ mHz for a $1-3$ mixture near 568 G. In Ch. 5 we use these parameters to describe the spin density evolution for different mixture of atoms.

3.4 Energy Dependent Scattering Length

For experiments in the non-degenerate regime at higher temperatures, we find that the energy dependence of the scattering length cannot be neglected. This energy dependence strongly modifies the spin-density profiles for small scattering lengths, and produces a shift of the zero crossing field. We include this dependence in $g(E', E)$ of Eq. 3.35 by replacing the energy-independent s-wave scattering length a_s with an energy dependent scattering length $a(E', E)$. The s-wave scattering length is given by the energy-dependent scattering amplitude $f(k)$,

$$a[B, k] = f\left(-2\mu_B B + \frac{\hbar^2\mathbf{k}^2}{2\mu}\right), \tag{3.59}$$

where $\hbar\,\mathbf{k}$ is the relative momentum and $\mu = m/2$ is the reduced mass. As explained in Ch. 2, the applied bias magnetic field $B_z \equiv B$ tunes the energy of a colliding pair in the triplet channel downward, at a rate $-2\mu_B B$, with μ_B the Bohr magneton. For our experiments in the degenerate regime, where the relative kinetic energy term in Eq. 3.59 is negligible, we assume that the scattering length varies linearly with applied magnetic field near the zero crossing field B_0,

$$a(B) = a'\,(B - B_0), \tag{3.60}$$

where the tuning rate of the scattering length a' is given in units of a_0/G, where a_0 is the Bohr radius. To include the relative kinetic energy K_{rel} in Eq. 3.59, we can replace the magnetic field B by an effective magnetic field,

$$B_{eff} = \langle B_z \rangle - \frac{\langle K_{\mathrm{rel}} \rangle}{2\mu_B}. \tag{3.61}$$

Here, we include an additional average of the spatially varying bias field B_z over the position of the center of mass (CM) of a colliding atom pair. The total CM energy is

$$E^x_{\mathrm{CM}} = \frac{\vec{P}_{\mathrm{CM}}{}^2}{2(2m)} + \frac{1}{2}(2m)(\bar{\omega}_x^2 X^2 + \bar{\omega}_\perp^2 (Y_{CM}^2 + Z_{CM}^2)). \tag{3.62}$$

Since here $X >> \rho = \sqrt{Y_{CM}^2 + Z_{CM}^2}$, we can rewrite the center of mass energy using the Virial theorem for a harmonic trap, which holds for weakly interacting atoms. Thus, we obtain $2m\,\bar{\omega}_x^2\,\langle X^2_{\mathrm{CM}} \rangle = \langle E^x_{\mathrm{CM}} \rangle$, where $2m$ is the total mass. In the following, I will show how to evaluate $\langle B_z \rangle$.

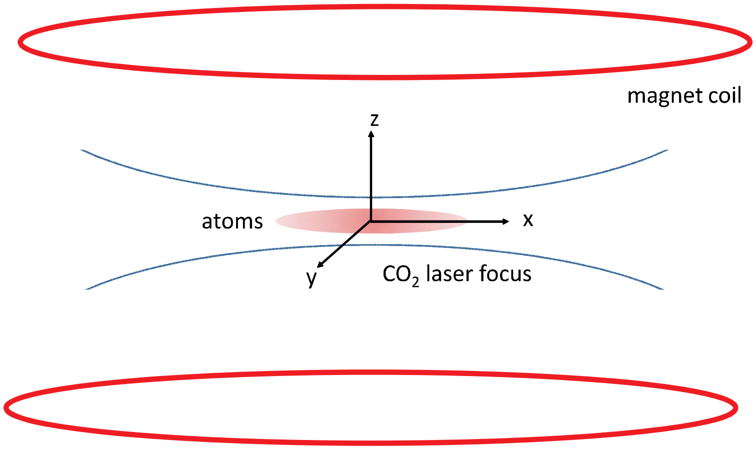

Figure 3.6: Orientation of the optical and magnetic potentials, objects not to scale. The atom cloud, in red, forms a tri-axial ellipsoid at the focus of a CO2 laser beam. Due to the curvature of the bias field, a spin-dependent potential forms for atoms with different magnetic moment.

As we see in Fig. 3.6, the bias field is cylindrically symmetric about the z axis, and oriented perpendicular to the long x-axis of the trapped cloud, so that $B_z = B_{z0}[1 + b(z^2 - (x^2 + y^2)/2)]$, where B_{z0} is the bias field at the cloud center and $b\,B_{z0}$ is the field curvature. For the cigar-shaped clouds utilized in the experiments, the variation of B_z in the z and y directions is negligible compared to that in the x direction, so that $B_z(x) = B_{z0}[1 - b\,x^2/2]$. We determine $b\,B_{z0}$ from the measured spring constant of the resulting harmonic confining potential, $-\mu_B B_z(x)$, where for ^{6}Li, the magnetic moment, $+\mu_B$, of the three lowest hyperfine states at high B field is dominated by the electron spin down contribution, $m_s = -1/2$. With $\mu_B\,b\,B_{z0} \equiv m\omega_{\rm mag}^2$, where $\omega_{\rm mag}$ is given above, the bias field, averaged over the center of mass position, is then $\langle B_z\rangle = B_{z0} - m\omega_{\rm mag}^2\,\langle X_{\rm CM}^2\rangle/(2\mu_B)$. Hence,

$$B_{eff} = B_{z0} - \frac{\omega_{\rm mag}^2}{\bar{\omega}_x^2}\frac{\langle E_{\rm CM}^x\rangle}{4\mu_B} - \frac{\langle K_{\rm rel}^x\rangle}{2\mu_B} - \frac{\langle K_{\rm rel}^\perp\rangle}{2\mu_B}. \tag{3.63}$$

Here, we have separated the relative kinetic energy term of Eq. 3.61 into axial and transverse parts.

Next, we need to evaluate the relative kinetic energy contributions in the above equation. For the axial x-direction, we *select* the axial energies of the two colliding atoms E and E' in $g(E, E')$, Eq. 3.35. Hence, the total energy is $E + E' = E_{\rm CM}^x + E_{\rm rel}^x$. For harmonic confinement, the kinetic and potential energies are quadratic degrees of freedom, which requires $E_{\rm CM}^x = (E + E')/2$ for any product state $\phi_E(x_1)\,\phi_{E'}(x_2)$. We also have $E_{\rm rel}^x = (E+E')/2$, where $E_{\rm rel}^x = K_{\rm rel}^x + \mu\,\bar{\omega}_x^2\,x_{\rm rel}^2/2$ for harmonic confinement. To evaluate $\langle K_{\rm rel}^x\rangle$, we note that for a collision to occur, the relative position $x_{\rm rel}$ of the two atoms must vanish for a contact interaction. Hence, $K_{\rm rel}^x = E_{\rm rel}^x = (E + E')/2$. For the transverse directions, we have defined a mean fractional spatial density $\bar{n}_\perp$, by Eq. 3.21. Assuming that the corresponding relative momentum average for the two transverse directions is determined by a Boltzmann distribution, $\langle K_{\rm rel}^\perp\rangle \simeq k_BT$. Using these results in Eq. 3.63, we obtain finally,

$$B_{eff} = B_{z0} - \frac{\langle K_{\rm rel}^\perp\rangle}{2\mu_B} - \left(1 + \frac{\omega_{\rm mag}^2}{2\bar{\omega}_x^2}\right)\frac{E + E'}{4\mu_B}, \tag{3.64}$$

where we leave $\langle K_{\rm rel}^\perp\rangle$ as an adjustable parameter, of order k_BT. Replacing a_S with $a(E', E) = a'(B_{eff} - B_0)$ in $g(E', E)$ of Eq. 3.31 and in the results for $\tilde{g}(n', n)$ that follow from it, we obtain a reasonable fit to the high temperature spin density profile shown in Fig. 5.14 with $\langle K_{\rm rel}^\perp\rangle = 0.59\,k_BT$. For $T = 45.7\,\mu$K, this corresponds to a shift of -0.2 G in B_{eff}, consistent with the upward shift of the applied field for which $a_{12} = 0$, as reported in Table. 5.1 of Ch. 5. For the low temperature data, where the energy scale is $< 1\,\mu$K, the corresponding energy shift is negligible.

Chapter 4

Information Scrambling in a Weakly interacting Fermi Gas

In this chapter, I will describe the theory of out-of-time order correlation (OTOC) functions in a weakly interacting Fermi gas, which is confined in a spin-dependent harmonic trap. I will show that by employing an inverse Abel-transform method, one can extract an energy-dependent spin vector $\mathbf{S}(E)$ from the spatial profile of the spin density $\mathbf{S}(x)$, providing a new platform for the study of information scrambling in large many-body systems.

4.1 Out-Of-Time-Order Correlation Function

Recently, it has been shown that measurements of certain out-of-time-order correlation (OTOC) functions [Schleier-Smith, 2017, Marino and Rey, 2019, Swingle and Yao, 2017] can serve as entanglement witnesses to quantify coherence and information scrambling in quantum many-body systems [Gärttner et al., 2017, Gärttner et al., 2018].

In this dissertation, "scrambling" denotes the spread of quantum information over the many-body degrees of freedom, which becomes inaccessible to local probes. OTOC measurements have been performed by reversing the time evolution of the many-body state, which is achieved by reversing the sign of the Hamiltonian. Such protocols were first implemented in nuclear magnetic resonance experiments at high temperatures, where the initial state is described by a density operator and high order quantum coherence has been observed [Baum et al., 1985].

New OTOC studies have been performed in trapped ion systems in a Penning trap containing relatively small numbers of atoms, where the individual sites are nearly equivalent, and the initial state is pure [Gärttner et al., 2017]. Related methods have been developed for systems containing up to 100 atoms [Lewis-Swan et al., 2019], but the application to very large numbers remains a challenge.

OTOC measurements in trapped, weakly interacting Fermi gases offer new prospects for understanding information spreading in large quantum systems containing $N \simeq 10^5$ atoms with a tunable, reversible Hamiltonian [Du et al., 2009, Smale et al., 2019]. Here, I will explain out-of-time-order correlation functions and their application to study higher order quantum coherence and information scrambling in the many-body system of ultracold fermions.

For a pure initial state $|\psi_0\rangle$, the utility of the OTOC can be simply understood as following [Schleier-Smith, 2017, Gärttner et al., 2017, Lewis-Swan et al., 2019]. Let $\hat{W}$ and $\hat{V}$ be two, generally time-dependent, operators. Then, consider the two states $|\psi_1\rangle = \hat{W}\hat{V}|\psi_0\rangle$ and $|\psi_2\rangle = \hat{V}\hat{W}|\psi_0\rangle$, where the operators are applied in reverse order on the initial pure state. The overlap between these two states is

$$\mathcal{F} \equiv \langle\psi_2|\psi_1\rangle = \langle\psi_0|\hat{W}^\dagger\hat{V}^\dagger\hat{W}\hat{V}|\psi_0\rangle, \tag{4.1}$$

which is of the OTOC form.

Given two, quantum operators $\hat{W}$ and $\hat{V}$, one imagines comparing two processes: (i) apply V, evolve forward in time, apply $\hat{W}$, and evolve backward in time, (ii) Evolve the system forward in time, apply $\hat{W}$, evolve backward in time, and apply $\hat{V}$; as shown in Fig. 4.1.

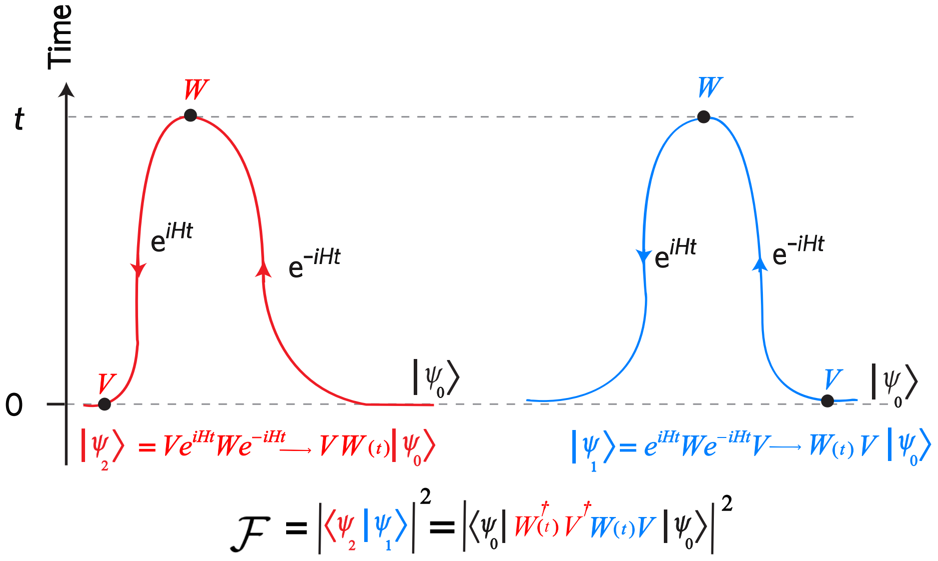

Figure 4.1: In the left diagram, the system first evolves forward in time, then, W operator followed by backward in time evolution, and finally V operator is applied on the state. In the right diagram, operator V is applied. Then, the system evolves forward in time followed by W operator, and finally the system evolves backward in time. $\mathcal{F}$ is the out-of-time-order correlation function, which quantifies the overlap between $|\psi_2\rangle$ and $|\psi_1\rangle$ [Schleier-Smith, 2017].

What does this comparison tell us? Drawing on an analogy to classical chaos, one interpretation is that comparing the two processes reveals the sensitivity of a measurement of V to a perturbation W, a kick from an external field that happened some time in the past. If the measurement is very sensitive to the perturbation, we have a quantum version of the classical butterfly effect, in which a small initial perturbation eventually has a major effect. Taking the analogy further, a quantum system in which information becomes scrambled can be viewed as a quantum chaotic system, and the OTOC provides a measure of the scrambling [Swingle and Yao, 2017, Schleier-Smith, 2017]. In the following, we will look more closely at Eq. 4.1.

Suppose that $\hat{W}$ and $\hat{V}$ commute at time $t = 0$. Then from Eq. 4.1, $\mathcal{F}(0) = 1$ only for the unitary $\hat{W}$ and $\hat{V}$ operators. Using $2\,Re\{\mathcal{F}\} = \mathcal{F} + \mathcal{F}^*$, we get

$$2\,Re\{\mathcal{F}\} = \langle\psi_0|\hat{W}^\dagger\hat{V}^\dagger\hat{W}\hat{V}|\psi_0\rangle + \langle\psi_0|\hat{V}^\dagger\hat{W}^\dagger\hat{V}\hat{W}|\psi_0\rangle, \tag{4.2}$$

which can be written as

$$\begin{aligned} 2\,Re\{\mathcal{F}\} &= \langle\psi_0|\,[\hat{W}^\dagger,\hat{V}^\dagger]\;[\hat{W},\hat{V}]\,|\psi_0\rangle + \langle\psi_0|\hat{V}^\dagger\hat{W}^\dagger\hat{W}\hat{V}|\psi_0\rangle + \langle\psi_0|\hat{W}^\dagger\hat{V}^\dagger\hat{V}\hat{W}|\psi_0\rangle \\ & [\hat{W}^\dagger,\hat{V}^\dagger] = -[\hat{W},\hat{V}]. \end{aligned} \tag{4.3}$$

As shown in Fig 4.1, $|\psi_1\rangle = \hat{W}\hat{V}\,|\psi_0\rangle$ and $|\psi_2\rangle = \hat{V}\hat{W}\,|\psi_0\rangle$, where the subscription of $\hat{W}$ operator is eliminated. By simplifying above commuting relations, it is straightforward to obtain

$$2\,Re\{\mathcal{F}\} \;=\; \langle\psi_0|\hat{V}^\dagger\hat{W}^\dagger\hat{W}\hat{V}|\psi_0\rangle + \langle\psi_0|\hat{W}^\dagger\hat{V}^\dagger\hat{V}\hat{W}|\psi_0\rangle - \langle\psi_0||[\hat{W},\hat{V}]|^2|\psi_0\rangle. \tag{4.4}$$

For the unitary $\hat{W}$ and $\hat{V}$, $\langle\psi_1\mid\psi_1\rangle = 1$ and $\langle\psi_2\mid\psi_2\rangle = 1$ for all t, thus we obtain an important relation between OTOC function as

$$\frac{1}{2}\langle\psi_0||[\hat{W},\hat{V}]|^2|\psi_0\rangle = 1 - Re\{\mathcal{F}\}. \tag{4.5}$$

From Eq. 4.5, we see that if the operators $\hat{W}$ and $\hat{V}$ do not commute for $t > 0$, then $Re\{\mathcal{F}(t)\} < 1$. Thus, a measurement of $Re\{\mathcal{F}\}$ determines how two initially commuting operators, $Re\{\mathcal{F}(0)\} = 1$, fail to commute at a later time in a many-body system, providing a measure of information scrambling [Gärttner et al., 2017, Lewis-Swan et al., 2019]. In Ch. 6, I will present an experimental protocol in which $\hat{W}$ applies a controllable rotation to the total interacting spin system in between the forward and time-reversed evolutions, using radio-frequency pulses. The operator $\hat{V}$ performs a measurement to diagnose the effects of the rotation on the spins of energy E_i, i.e., at “site” i in energy space, as shown in Fig. 5.2.

As described in the previous chapter, the Hamiltonian for a weakly interacting Fermi gas, confined in a cigar-shaped optical trap along the x-axis, takes the form of a spin “lattice” in energy space, Eq. 3.7, with

$$H(a) = -\sum_i \Omega_i \, s_{zi} + a \sum_{i,j \neq i} g_{ij} \, \mathbf{s}_i \cdot \mathbf{s}_j \tag{4.6}$$

in units of s^{-1}. Here, $\mathbf{s}(E_i) \equiv \mathbf{s}_i$ is the dimensionless collective spin vector for atoms of energy E_i, the energy of the i^{th} axial harmonic oscillator state, which plays the role of the "site" i. The site-to-site interaction is governed by the tunable s-wave scattering length a and by $g_{ij} \propto \int dx \, |\phi_{E_i}(x)|^2 \, |\phi_{E_j}(x)|^2$, the overlap of the probability densities for colliding atoms of energies E_i and E_j, which produces an effective long range interaction $\propto 1/\sqrt{|E_i - E_j|}$ [Pegahan et al., 2019].

The effective Zeeman interaction is site-dependent, $\Omega(E_i) \equiv \Omega_i = \Omega' \, (E_i - \bar{E}) + \Delta$, which is identical to the Zeeman frequency of Ch. 3. Here, $\Omega' \, (E_i - \bar{E})$ scales linearly with energy, and arises from the curvature of the bias magnetic field, which produces a difference between the harmonic oscillation frequencies of the $\uparrow_z$ and $\downarrow_z$ states in the net, weakly confining axial potential. Δ is a global radio-frequency detuning, where $\Delta = 0$ corresponds to resonance for atoms of mean energy $\bar{E}$. As the bias field curvature has a negligible effect on the tight transverse, (y, z), confining potential, the system is effectively one-dimensional.

In the following, I will talk about the OTOC function for the subset of spins in the energy-space. This provides building blocks for the experimental study of information scrambling in Ch. 6.

4.1.1 Extracting OTOC for Individual Spins in Energy-Space

Now that we are familiar with the OTOC measurement, I will apply Eq. 4.5 to a system of spins in the energy space. In the many-body system of spins, we define $\hat{W}(t)$ shown in the Fig. 4.1, as the following,

$$\hat{W}(\tau) = e^{iH\tau} e^{-i\phi \, S_x} e^{-iH\tau}. \tag{4.7}$$

This operator applies a rotation to the total interacting spin system in between the forward and time-reversed evolutions. In Eq. 4.7, $S_x = \sum_{j=1}^{N} \hat{s}_{xj}$ is the x-component of the total spin vector. For the operator $\hat{V}$, we choose $\hat{V} = 2 \, \hat{s}_{xi} = \hat{\sigma}_{xi}$, i.e., the x-Pauli matrix for the i^{th} spin. With this choice, $\hat{V}^\dagger = \hat{V}$ and $\hat{V}^\dagger \hat{V} = \hat{\sigma}_x^2 = \hat{1}$. Further, with an initial σ_x-eigenstate as $\hat{V}|\psi_0\rangle = |\psi_0\rangle$, OTOC for i^{th} spin in energy lattice is

$$\mathcal{F}^{\,i} \equiv 2 \, \langle \psi_0 | \hat{W}^\dagger \hat{\sigma}_x^i \hat{W} \hat{\sigma}_x^i | \psi_0 \rangle = \langle \psi_0 | \hat{W}^\dagger \hat{\sigma}_x^i \hat{W} | \psi_0 \rangle. \tag{4.8}$$

$\mathcal{F}^{\,i}$ here is a real quantity. The right hand side of this equation leads to a relation very similar to Eq. 4.5. Therefore, OTOC for i^{th} spin can be written as the square of commuting operators at $t > 0$

$$\mathcal{F}^{\,i} = 1 - \frac{1}{2}\langle\psi_0||[\hat{W}, \hat{\sigma}_x^i]|^2|\psi_0\rangle. \tag{4.9}$$

In the next section, we will extend the results of Eq. 4.9 to a system with an ensemble of spins at different energy. In Ch. 6, we will use these results to model the energy-resolved OTOC functions.

4.1.2 Extracting OTOC for a Subset of Spins in Energy-Space

The system that we study, contains thousands of spins in different energy space partitions. Therefore, if we consider a system with N-spins, for a subset of N$_s$ spins with nearly the same energy, the average OTOC can be written as

$$\bar{\mathcal{F}}(\tau) \equiv \frac{1}{N_S}\sum_{i=1}^{N_S}\bar{\mathcal{F}}^{\,i}(\tau). \tag{4.10}$$

The average of OTOC for the system of spins using Eq. 4.8 and $\sigma_{xi} = 2s_x^i$, will be

$$\bar{\mathcal{F}}(\tau) = \frac{2}{N_S}\sum_{i=1}^{N_S}\langle\psi_0|\hat{W}^\dagger(\tau)\hat{s}_x^i\hat{W}(\tau)|\psi_0\rangle. \tag{4.11}$$

For this system, if we want to find the commutator relation similar to Eq. 4.9, we can show that Eq. 4.11 is

$$\begin{aligned}
\bar{F}(\tau) &= \frac{2}{N_S}\sum_{i=1}^{N_S}\langle\psi_0|\hat{W}^\dagger(\tau)\hat{s}_x^i\hat{W}(\tau)|\psi_0\rangle \\
&= \frac{1}{N_S}\sum_{i=1}^{N_S}\Big(\, 1 - \frac{4}{2}\langle\psi_0||[\hat{W}(\tau), \hat{s}_x^i]|^2|\psi_0\rangle\Big) \\
&= 1 - \frac{2}{N_S}\sum_{i=1}^{N_S}\langle\psi_0||[\hat{W}(\tau), \hat{s}_x^i]|^2|\psi_0\rangle.
\end{aligned} \tag{4.12}$$

by rearranging this relation, we can find spin-averaged mean-square commutator as

$$\frac{1}{N_S}\sum_{i=1}^{N_S}\langle\psi_0||[\hat{W}, \hat{s}_x^i]|^2|\psi_0\rangle = \frac{1}{2} - \frac{1}{N_S}\sum_{i=1}^{N_S}\langle\psi_0|\hat{W}^\dagger\hat{s}_x^i\hat{W}|\psi_0\rangle, \tag{4.13}$$

which is similar to Eq. 4.5. Eq. 4.13 provides a valuable measure of information scrambling in the subset of spins in the many-body system and can be extended to the whole system by considering all range of energies (up to E_F in the degenerate regime). If the left hand side of this relation is non-zero, we can conclude that for the subset of N_S spins with the same energy, scrambling has happened due to perturbation from $\hat{W}$, coherence has spread throughout the many-body system of spins.

Eq. 4.13 provides the OTOC for a many-body system of spins with nearly the same energy. It is important to understand how to transform the collective spin density vector from the spatial coordinate to energy space, using an inverse-Abel transform. In Ch. 3, we assumed that there is no energy-space coherence i.e., for each spin state

$$n_\sigma(x,\phi) = \sum\nolimits_E |\phi_E(x)|^2 n_\sigma(E,\phi). \tag{4.14}$$

For a harmonic trap, the $|\phi_E(x)|^2$ are the harmonic states, and $n_\sigma(x,\phi)$ in a continuous limit, corresponds to an integral Abel-transform that can be inverted. Thus, we find the energy dependent spin density $n_\sigma(E,\phi)$ through an inverse able transform from Eq. 4.14. Measured collective spatial spin vector will be shown in Ch. 5, and inverse-Abel transform of measured spin density will be discussed for OTOC functions in Ch. 6.

4.2 Inverse Abel-Transform Method

To employ an inverse Abel-transform method as discussed above, we assume that the measured axial spin density profiles are given in the continuum limit,

$$\mathbf{S}(x,t) = \int dE\, |\phi_E(x)|^2\, \mathbf{S}(E,t), \tag{4.15}$$

which is defined so that $\int dx\, \mathbf{S}(x,t) = \int dE\, \mathbf{S}(E,t)$ is the total collective spin vector. As I mentioned earlier, an important feature of Eq. 4.15 is the assumption that there is no coherence between states of different energy, which is justified in the energy-conserving regime of a very weakly interacting Fermi gas. Physically, each atom remains on its respective energy "site," E_i. This assumption in Ch. 5 yields to predictions in very good agreement with the small scale spatial structure observed in the spin density $S_z(x)$ for single pulse experiments. In the continuum limit, where the harmonic oscillator energy level spacing is small compared to the energy scale, the harmonic oscillator wave functions can be evaluated in using a WKB approximation similar to approximations in Ch. 3. In this case, the probability densities take the simple form,

$$|\phi_E(x)|^2 = \frac{\bar{\omega}_x}{\pi} \int_0^\infty dp_x\, \delta\left(E - \frac{p_x^2}{2m} - \frac{m\bar{\omega}_x^2}{2}x^2\right). \tag{4.16}$$

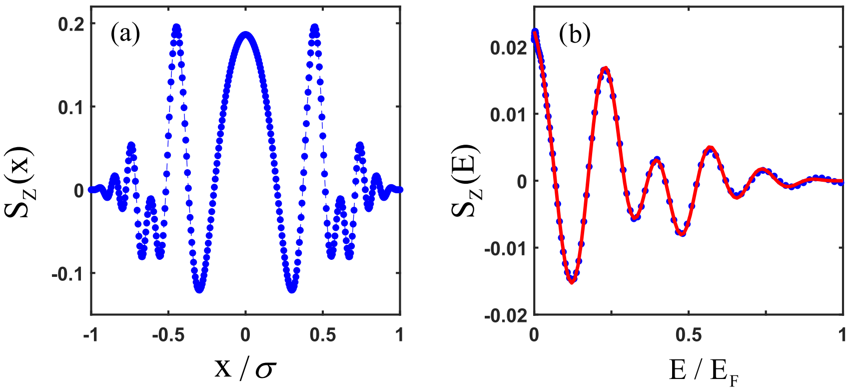

Figure 4.2: Testing the inverse Abel-transform method. Using a mean field model, spin density "data" (a) for $S_z(x, \phi = \pi)$ are generated for the protocol of Fig. 1 of the main paper, with the same x-spacing as the actual data. Inverse Abel-transformation (right) yields $S_z(E, \phi = \pi)$ (b), which closely matches the input $S_z(E, \phi = \pi)$ (red curve) from the mean field model, which was used to generate the model data for the spin density spatial profile.

Then with Eq. 4.15, the spin density is

$$\mathbf{S}(x,t) = \frac{\bar{\omega}_x}{\pi} \int_0^\infty dp_x \, \mathbf{S}\left(\frac{p_x^2}{2m} + \frac{m\bar{\omega}_x^2}{2} x^2, t\right). \tag{4.17}$$

This is an Abel-transform, i.e., the y-integral of a function of $x^2 + y^2$. Hence, an inverse Abel-transform enables a determination of the energy-dependent collective spin component $S_z(E,t)$ from the measured spatial profile $S_z(x,t)$. To extract $S_z(E)$ from the data, the measured spatial profile is first symmetrized by folding about $x = 0$ and then an inverse Abel-transform is implemented without employing derivatives by using the method described in [Pretzier, 1991]. For this method, the unknown radial distribution is expanded in a series of cosine-functions, the amplitudes of which are calculated by least-squares-fitting of the Abel-transformed series to the measured data. In our analysis, we use up to 20 cosine terms.

To test the inversion method, we generate "data" using the mean field model for $S_z(x, \phi = \pi)$, shown in Fig. 4.2, with the same x spacing as the real data, the single-shot spin density profiles taken after the many-body spin protocol, shown in Fig. 4.3 (details in Ch. 6). We see that $S_z(E)$ appears smooth compared to the single shot spin density $S_z(x)$, which requires averaging over several shots to obtain a smooth profile.

Inverting the "data" for $S_z(x, \phi = \pi)$, we find the result shown as the blue curve of Fig. 4.2 (b). We start with a small number of cosine terms and increase the number until the agreement with the exact mean-field input $\mathbf{S}(E, \phi = \pi)$ (red curve) shows no further improvement. Using 20 cosine terms, we find that the $S_z(E, \phi = \pi)$ obtained from the spatial

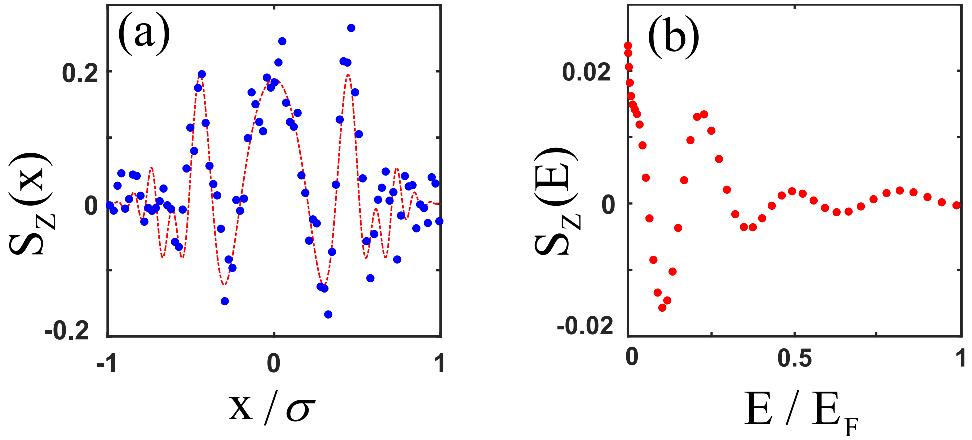

Figure 4.3: Energy-resolved out-of-time-order correlation measurement. (a) “single-shot” spin density profile $S_z(x)$ (blue dots). The red dashed curve is shown to guide the eye; (b) An inverse-Abel transform of the spatial profile (blue dots) is used to extract the single-shot energy-resolved spin density $S_z(E)$ (red dots). The scattering length is measured at $a = 4.24\,a_0$.

profile by inversion (blue) is in close agreement with the exact input from the mean field model (red curve) that was used to generate the spatial profile.

Next, we apply the Abel-transform method to find the energy-dependent spin component $S_z(E, \phi)$ from the measured spin density $S_z(x, \phi)$, Fig. 4.4 (a). We check the consistency of the

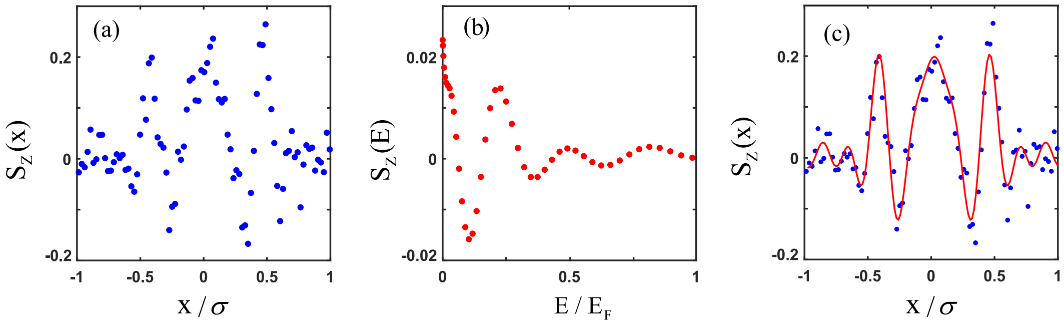

Figure 4.4: Extracting the energy-dependent collective spin component $S_z(E, \phi = \pi)$ for a single shot. (a) Measured single-shot spin density $S_z(x, \phi = \pi)$ for the protocol of Fig. 4.3 with $a = 4.24\,a_0$ and $\phi = \pi$. (b) Inverse Abel-transformation of (a) yields $S_z(E, \phi = \pi)$ (red dots). (c) $S_z(x, \phi = \pi)$ (red curve) generated from the extracted $S_z(E, \phi = \pi)$ is consistent with the input spin density data (blue dots).

extracted $S_z(E, \phi)$ by Abel-transformation, which generates $S_z(x, \phi = \pi)$ for comparison to the input data Fig. 4.4(c).

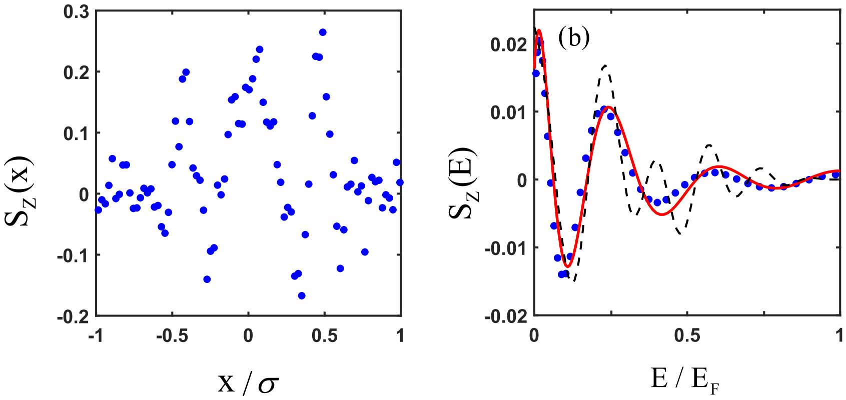

Figure 4.5: Comparison of the extracted energy-dependent collective spin component $S_z(E, \phi = \pi)$ for a single shot with the mean field model. (a) Measured single-shot spin density $S_z(x, \phi = \pi)$ with $a = 4.24\, a_0$ and $\phi = \pi$. (b) Inverse Abel-transformation of (a) with 8 cosine terms yields $S_z(E, \phi = \pi)$ (blue dots). The red curve is the $S_z(E, \phi = \pi)$ obtained with an 8-term inverse-Abel transform of $S_z(x, \phi = \pi)$. The black-dashed curve shows the $S_z(E, \phi = \pi)$ that is obtained directly from the mean field model, i.e., without inverse-Abel transform of the predicted spatial profile. Scattering length $a_{fit} = 2.35 \times 4.24\, a_0$ and a global detuning $\Delta = 2\pi \times 0.27$ rad/s.

Fig. 4.5, shows a comparison between the $S_z(E, \phi = \pi)$ curves extracted using an 8-term inverse-Abel transform of the single shot data $S_z(x, \phi = \pi)$ and by an 8-term inverse-Abel transform of the spatial profile predicted by the mean field model. We find that the predicted and measured shapes are in good agreement. However, the mean field model requires a scattering length that is 2.35 times the measured value, suggesting that a more complete treatment is needed.

In Ch. 6, I will extract the out-of-order-correlation function from 4.13, and compare the simulated model for the ensemble of spins with the experimental observation; I reveal a rich coherence structure that is hidden in measurements of the total collective spin vector.

Chapter 5

Measurement of Spin-Energy Correlation in Fermi Gases

In this chapter, I will present experimental measurements of time-dependent spin-density profiles for coherently prepared two-state Fermi gases of ^{6}Li, confined in a spin-dependent harmonic potential. This measurements provide a precise quantitative test of the underlying energy-space spin-lattice model and energy-dependent long-range couplings, discussed in Ch. 3. I will show this system allows implementing the most precise measurements of the zero crossings for ^{6}Li atoms and the scattering length tuning with a magnetic field near the zero crossing.

5.1 Preparation of a Degenerate Fermi Gas

The evolution of the spin density in weakly interacting Fermi gases has been described by mean field models employing phase-space representations [Piéchon et al., 2009, Du et al., 2008] and energy representation [Du et al., 2009]. However, the initial implementation by control of the energy-dependent collective spin-rotation model yielded only semi-quantitative agreement with the observed spin-density profiles and the time-dependent amplitude, which were measured at high temperatures, suggesting that the model was incomplete.

Using the collective spin-rotation model from Ch. 3, we show that our model, without additional simplifying approximations, quantitatively predicts the observed spin-density profiles. At high temperatures and small scattering lengths $a < 1$ Bohr, we observe additional features in the spin-density profiles, which we will explain by including the energy dependence of the scattering length in our model.

In the next section, I will explain the experimental sequence for preparing the degenerate sample, and following that, I will show the measured spin density profiles versus the mean-field model.

5.1.1 Experimental Sequence

As described in Sec.2.5.1, once the atoms are loaded into the FORT, further cooling is achieved using a two-stage evaporative process, namely, free evaporation and forced evaporation. In the free evaporation cooling stage, a high bias magnetic field is applied, 832.2 G, so that the atoms' collision rate increases drastically. Experimentally, the evaporative cooling cycle takes approximately 8 s, as shown in Fig. 5.1. Atoms inside the FORT are attracted to the high intensity region. At the focus of the dipole trap the intensity is $2 \times 10^6\, W/\text{cm}^2$, with stronger confinement in the radial direction and weaker confinement in the axial direction.

After the free evaporation process, the $CO2$ trap potential is lowered adiabatically (denoted as the solid black curve in Fig. 5.1) to about 0.2% from its peak value at the same high bias magnetic field. The optical trap is then reraised to 2% of the maximum $CO2$ power. The final trap depth provides radial confinement. Even though atoms are tightly confined radially, they can oscillate freely along the axial direction as the confinement is much weaker than a radial direction. In the following, I will show how different confinement leads to two harmonic trapping potentials in a weakly interacting regime.

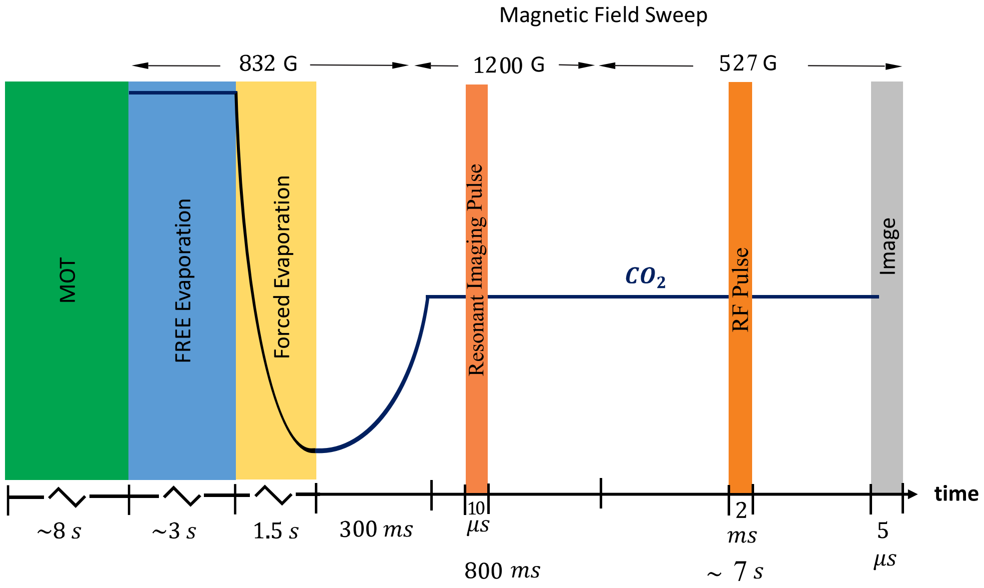

Figure 5.1: Timing sequence for preparing a coherent atomic sample. The solid black curve shows the variation of the potential depth of the CO2 laser beam. The bias magnetic field first tunes from 832.2 G to the weakly interacting regime near 1200 G. After removing state $|1\rangle$ from the trap, the magnetic field is ramped to 527 G, near the zero crossing of scattering length for $|1\rangle - |2\rangle$ mixture. 2 ms radio frequency (RF) pulse is applied to create a coherent superposition of $|1\rangle - |2\rangle$. A 5 μs resonance optical pulse shines on an atomic cloud for detecting the atom number in a different hyperfine state.

At the end of the forced evaporation process, an atomic cloud comprising a 50-50 incoherent mixture of the two lowest hyperfine states, denoted $|1\rangle$ and $|2\rangle$, are cooled to degeneracy with $T/T_F = 0.35$. As previously shown in [Du et al., 2008, Du et al., 2009, Pegahan et al., 2019] and in Sec. 5.2, we need to prepare a coherent sample of atoms to study spin-dependent effects in the presence of a magnetic field gradient, shown in Fig. 3.6.

Thus, we ramp the magnetic field from 832.2 G to the weakly interacting regime near 1200 G, shown in Fig. 2.6. In this field, the $|1\rangle$ spin component is eliminated by means of a resonant optical pulse that we use for imaging $|1\rangle$ state. Now that we have only state $|2\rangle$ present in the trap, we can tune the magnetic field near 527 G. At this magnetic field, the s-wave scattering length a is adjusted to nearly vanish. Finally, a 2 ms radio-frequency $\pi/2$ pulse, which is resonant with the transition from state $|2\rangle$ to $|1\rangle$, creates the coherent mixture of these two states.

The coherent states in a $|1\rangle - |2\rangle$ interact via s-wave contact interaction. Since the direct collision between atoms are negligible, the long-range interaction play a crucial role in the spin density dynamics, as shown in Fig. 5.2. At this regime, if we consider the s-wave scattering length to be $a = 4.24\ a_0$, the corresponding collision rate yields,

$$\gamma_c = \frac{N_\downarrow m_{^6Li}(\omega_\perp^2 \omega_x) 4\pi a_s^2}{4\pi^2 k_B T_F} \simeq 0.002. \tag{5.1}$$

Since s-wave scattering in Fermi gases is allowed only for antisymmetric spin states, two-component clouds exhibit an effective exchange interaction, enabling simulations of a variety of spin-lattice models where that single atom energies are conserved [Piéchon et al., 2009, Natu and Mueller, 2009, Deutsch et al., 2010, Wall, 2020] over the time scale set by the mean field frequency $\propto |a|$ in Eq. 3.51, which can be in order of 1 sec or more.

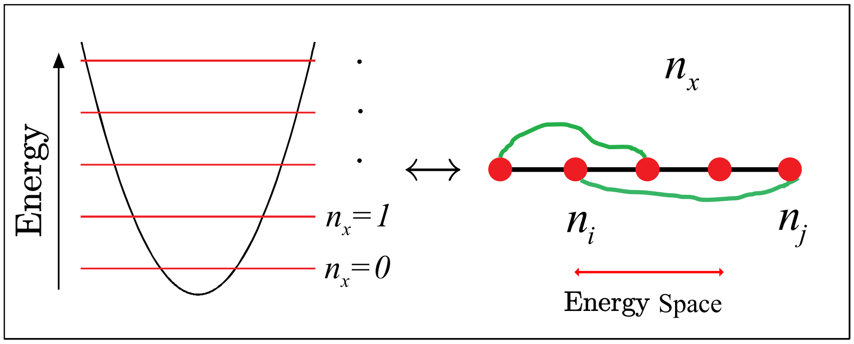

Figure 5.2: 1-Dimensional energy lattice. The green lines shows the long range interaction between spins in the "lattice" site in energy space, where scale with $1/\sqrt{n_i - n_j}$.

Similarly, for studying the zero crossing for 2−3 mixture, the bias field ramped to 589 G, close to their corresponding zero crossing. Then, the superposition state is prepared by employing an rf transition from state $|2\rangle$ to state $|3\rangle$ at 589 G.

To create $|1\rangle - |3\rangle$ superposition state, we again prepare a single $|2\rangle$ spin component at 1200 G. The magnetic field is then ramped down to the value of interest around 568 G, near the zero crossing of the $|1\rangle - |3\rangle$ scattering length. Then, atoms are excited by a 2 ms radio-frequency $\pi/2$ pulse, which is resonant with the transition from state $|2\rangle$ to state $|1\rangle$, creating a balanced $|1\rangle - |2\rangle$ superposition state. A 4 ms radio-frequency π pulse is applied, which is resonant with the transition from state $|2\rangle$ to state $|3\rangle$, to create a balanced $|1\rangle - |3\rangle$ superposition state.

After preparation of each coherent samples, we obtain degenerate cloud with a typical total atom number of $N = N_\uparrow + N_\downarrow \simeq 7.0 \times 10^4$ and an ideal gas Fermi temperature of $k_B T_F = \hbar(6N\bar{\omega}_x\omega_\perp^2)^{1/3} = k_B \times 0.70\,\mu$K for our trap frequencies. To determine the temperature T, the measured one dimensional total density versus x is fitted with a finite temperature Thomas-Fermi profile for a noninteracting gas, Fig. 1.8, which is appropriate for our weakly interacting gas. Using the calculated Thomas-Fermi radius $\sigma_{TF} = \sqrt{2\,k_B T_F/(m\bar{\omega}_x^2)} = 340\,\mu$m, we find $T = 0.28\,T_F$.

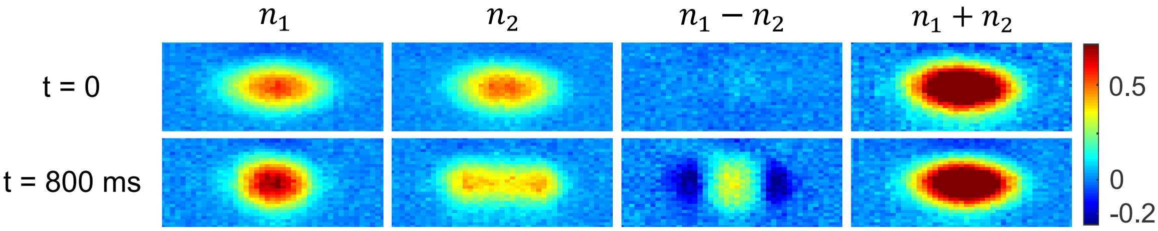

Figure 5.3: Spin-energy correlation produces spin segregation in a degenerate Fermi gas with the s-wave scattering length of 5.2 bohr. The palettes are $50 \times 950\,\mu$m. Left to right: n_1, n_2, $n_1 - n_2$, and $n_1 + n_2$ in units of $(n_1 + n_2)_{max}$ at $t = 0$ (upper) and $t = 800$ ms (lower) after coherent excitation of a $|1\rangle - |2\rangle$ superposition state. Note that $n_1 - n_2$ evolves in time while $n_1 + n_2$ remains constant, due to single particle energy conservation.

Due to the bias field curvature, we see the macroscopic spin evolution, Fig. 5.3, which lasts for $\sim 2\ s$. The coherent time scale in our system, however, can surpass this time and reach near $5\ s$. The first row of Fig. 5.3, shows the coherent superposition of $|1\rangle - |2\rangle$ states at $t = 0$. Due to forward s-wave scattering, see Sec. 3.1.1, spins in $|1\rangle$ state moves inward in the trap, and atoms at $|2\rangle$ state move outward. This behavior can be exchange simply by changing the sign of the s-wave scattering length from positive to negative.

By subtracting the two absorption images at different times, we can see a distinct pattern known as spin segregation. However, when we add the absorption images of two spins, the results are identical, shown in the last column in Fig. 5.3. This is proof that we are actually working in the weakly interacting regimes, with a negligible single particle collision, and the summation of two spins species leads to a degenerate Thomas Fermi cloud. One of the reasons that we employ degenerate quantum samples is to minimize energy shifts of the scattering length that become significant at higher temperatures. Moreover, degenerate Fermi gas allows for precise comparison of mean field model with measured spin-density profiles, which vary from relatively smooth for short time scales to exhibiting complex structure over short length scales.

In the following section, I will talk about the evolution of coherent spin states and will provide the quantitative agreement between the mean-field model and the measured spin density.

5.2 Spin Density Evolution as a Function of Time and Scattering Length

The subsequent evolution of the observed spin densities, Fig. 5.3, can be understood using a Bloch vector picture [Du et al., 2009]. In a frame rotating about the z-axis at the resonant hyperfine frequency, spin vectors for atoms in the n^{th} axial harmonic oscillator state precess about the z-axis, Fig. 3.2. First, as the magnetic moments of the two spin states are not identical, the finite curvature of the bias magnetic field, $B_z(x)$, creates a significant spin-dependent harmonic potential on the axial direction of the spin states, with negligible effects in the narrow transverse directions, as shown in Fig. 3.6. Hence the axial oscillation frequencies for the two spin states differ by $\delta\omega_x = \omega_{x2} - \omega_{x1} = -2\pi \times 14.9 \times 10^{-3}$ Hz. The small difference in the axial frequencies leads to $\Omega(E) = -n(E)\,\delta\omega_x$, which is an energy-dependent Zeeman precession about the z-axis, and $n(E) \simeq E/\hbar\bar{\omega}_x$, with $\bar{\omega}_x = (\omega_{x2} + \omega_{x1})/2 = 2\pi \times 23.0$ Hz. For typical conditions of experiment, $E_F = 0.70\,\mu$K, the detuning for the average x-energy, $\bar{E} = E_F/4$, is $\Omega(\bar{E}) \simeq -2\pi \times 2.0$ Hz. The $\Omega(E)$ causes the spin vectors for atoms of different energies to fan out in the $x - y$ plane, shown in Fig. 3.2.

Second, forward s-wave scattering, which is not Pauli-blocked in degenerate samples, occurs between two atoms with different energies and corresponding spin vectors, producing a rotation about the total spin vector [Du et al., 2009]. This s-wave scattering creates a mean field rotation of the collective spin with an energy-dependent z-component, which maps collective spin vector into a spatially varying spin density in the harmonic trap, as shown in Fig. 5.3. The evolution occurs on a time scale set by the mean field frequency, $\Omega_{MF} \simeq 2\pi \times 1.0$ Hz with $a = 5\ a_0$. As we discussed in Ch. 3, for the degenerate gas, the average of the mean field frequency from Eq. 3.48, is $< g(n,n') >=< \frac{\tilde{\Omega}}{\sqrt{s}} \frac{EllipicK(n,n')}{\sqrt{n-n'}} >= 3.78\,\Omega_{MF}$, and for the Boltzman gas

$< g(n,n') >= 1.97\,\Omega_{MF}$. Thus, the average mean-field frequency in the degenerate gas is close to 4 s for $a = 5\ a_0$. The trap parameters for our experiments are: $\omega_{\rm mag}^2 = (2\pi\times 20.5\,{\rm Hz})^2\,{\rm B(G)}/834$; $\bar{\omega}_x = 2\pi\times 23$ Hz, $\omega_\perp = 2\pi\times 625$ Hz, for the degenerate gas, and $\bar{\omega}_x = 2\pi\times 174$ Hz, $\omega_\perp = 2\pi\times 5.77$ kHz, for the high temperature gas. The calibration methods for extracting these parameters are described in Sec. 5.5.

Using the above measured parameters for the mean-field model of Ch. 3, we can capture the spin density profile shown in Fig. 5.4. These profiles are one dimensional spin densities

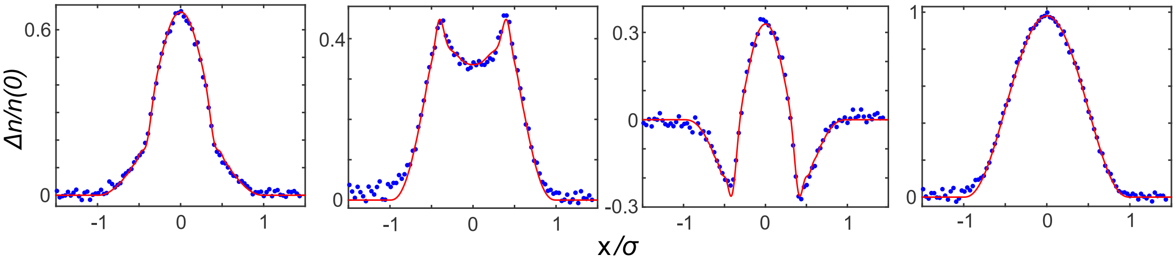

Figure 5.4: Spin-density profiles for a degenerate ($T/T_F = 0.28$) Fermi gas at $t = 800$ ms relative to coherent excitation. Data (blue dots) versus prediction (red curves) showing quantitative agreement. Left to right: n_1, n_2, $n_1 - n_2$, $n_1 + n_2$ in units of the peak total density. Each solid curve is the mean field model with a fixed scattering length of $a = 3.04$ bohr ($B = 528.147$ G) and a fitted cloud size $\sigma_{Fx} \equiv \sigma = 329\,\mu$m, obtained by fitting the total density $n_1 + n_2$ to a 1D Thomas-Fermi profile, Eq. 3.46.

integrated along the vertical (radial) direction of absorption images. These profile shown in Fig. 5.3 are captured at 800 ms after coherent excitation, for a degenerate $|1\rangle - |2\rangle$ cloud with $a = 3.04\,a_0$. Note when we subtracted the first two profiles, $n_1 - n_2$ evolves in time while $n_1 + n_2$ remains constant as shown in Fig. 5.5. This is due to single-particle energy conservation during the collective spin evolution. This provides evidence of energy conservation.

Next section, I will talk about the relation between s-wave scattering and the bias magnetic field. We use this relation to describe tunability and interaction strength between atoms as a function of the Bias field.

5.2.1 s-wave Scattering Tuning with a Magnetic Field

The most precise measurements of the universal thermodynamic properties and the universal hydrodynamic properties rely on the accurate location of the ^{6}Li broad Feshbach resonance near 832.2 G, which is constrained by the zero crossings [Zürn et al., 2013, Ku et al., 2012, Elliott et al., 2014]. Using the theory of spin-density evolution, I will show how to determine the zero crossings and magnetic field tuning rates for the s-wave scattering lengths of the three lowest

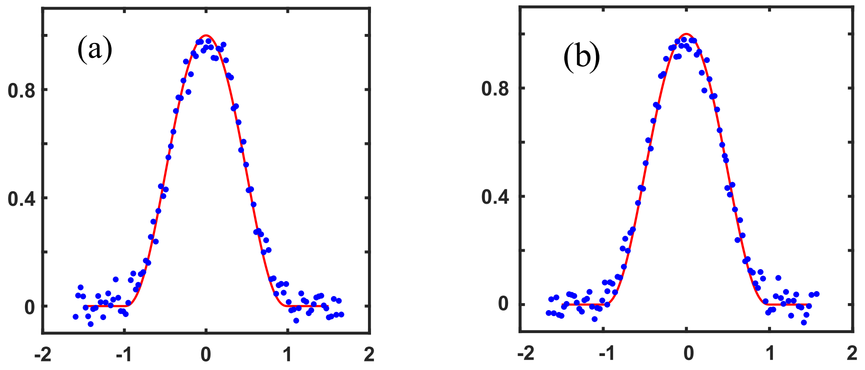

Figure 5.5: Single particle energy conservation. (a) Shows total spin density $n_1 + n_2$ at t=0. (b) Demonstrates total spin density $n_1 + n_2$ at $t = \ 800\ ms$. The solid red curve is from zero temperature Thomas Fermi fit which provide evidence of degenerate regime.

hyperfine states of ^{6}Li. These measurements provide new constraints on the $^6\text{Li}_2$ molecular potentials that determine the precise shapes of the Feshbach resonances [Bartenstein et al., 2005], which have been widely used in studies of strongly interacting Fermi gases [O'Hara et al., 2002].

We fit the mean field model to the spacial spin density profile of Fig. 5.8 in the following way. First, we plot the dimensionless spin density $(n_1 - n_2)/(n_1 + n_2)$ at the center $(x = 0)$ as a function of time, Fig. 5.6, for each value of the magnetic field. Second, we fit the model to the data of Fig. 5.6 to find the scattering length that gives the best fits (red curves). The fits to the spatial density profiles are then obtained by fixing the scattering length at each field to the value obtained from Fig. 5.6 and adjusting the Thomas-Fermi radius by a few percent to fit the measured profile at each time. The mean of the measured radii is found to be 322.0(1.5) μm and magnetic field stability is better than 5 mG, limited by measurement precision. The absolute value of the field is calibrated using radio frequency spectroscopy (see Sec. 5.5) of the hyperfine transitions.

As a result of fits to central spin density, we can find the small-a region, where

$$a(B) = a'\,(B - B_0). \tag{5.2}$$

In this region, the mean field model precisely fits the data. This region, shown in Fig. 5.7 enables measurement of the tuning rate a' (in bohr per gauss) of the scattering length near the zero crossing field B_0.

Here, we assume that the energy shift is negligible for the degenerate sample, in contrast to the hot sample discussed below. Using the data in Fig. 5.6, the fitted $|1\rangle - |2\rangle$ scattering length

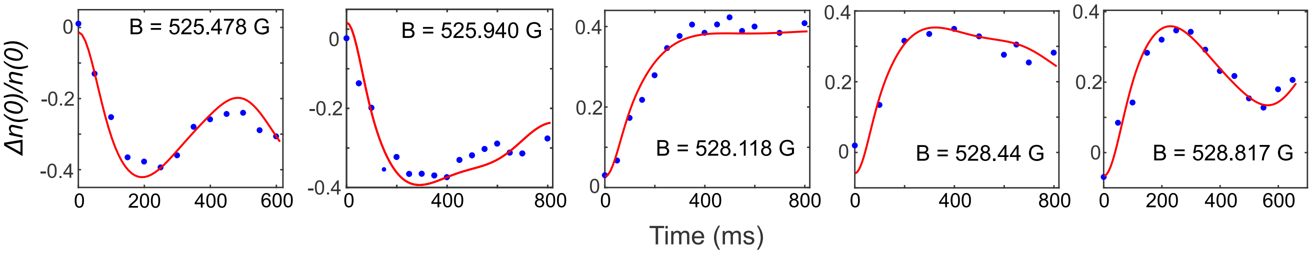

Figure 5.6: Central spin density versus evolution time for various magnetic fields near the zero crossing of the $|1\rangle - |2\rangle$ scattering length. $\Delta n(0) = n_1(0,t) - n_2(0,t)$ is given in units of $n_1(0) + n_2(0)$. Solid curves show the mean-field model with the scattering length a as a fit parameter. The fitted values of a are plotted in Fig. 5.7.

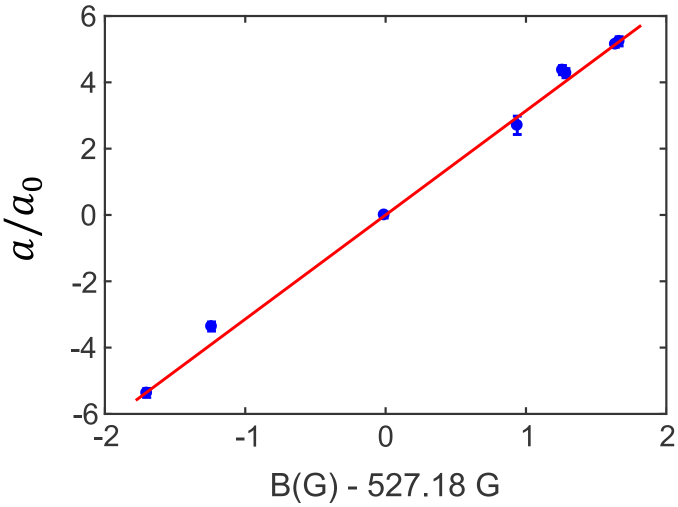

Figure 5.7: Fitted scattering length a versus measured magnetic field for a $|1\rangle - |2\rangle$ mixture ($a_0 = 1$ bohr). Error bars denote one standard deviation, obtained for each χ^2 fit of Fig. 5.6.

for each magnetic field is plotted in Fig. 5.7. The corresponding plot for $|2\rangle - |3\rangle$ scattering will be discussed in Sec. 5.3. The slopes of the linear fits to the data yield the tuning rates a', Table. 5.1.

Finally, Fig. 5.8 shows the difference of the transversely integrated spin densities $n_1(x,t) - n_2(x,t) \equiv 2S_z(x,t)$ at selected times t after excitation, for scattering lengths of larger magnitude, $\simeq \pm 5\, a_0$. For these fits, we keep the s-wave scattering constant and the only free parameter was Thomas Fermi radius, which varies within 5%.

5.2.2 Fit to Spatial Spin Density Profiles at Different Times

As we showed in Eq. 3.29, a thermal average of the Heisenberg equations for the collective spin vector $\tilde{\mathbf{S}}(E,t)$ yields,

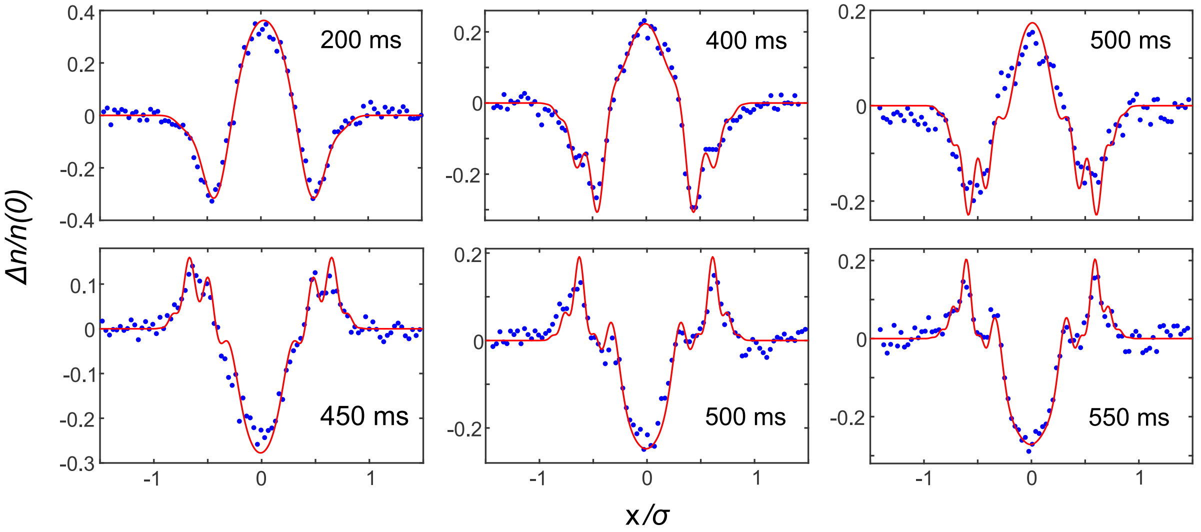

Figure 5.8: Spin-density profiles in a degenerate sample $T/T_F = 0.35$ at selected times relative to coherent excitation. $\Delta n(0) = n_1(0,t) - n_2(0,t)$ is given in units of $n_1(0) + n_2(0)$. Solid curves: Mean field model with the same scattering length for each time and a fitted cloud size within a few percent of the measured average value, $\sigma = 322.0(1.5)\,\mu$m. Top three panels: $B = 528.817$ G, $a = 5.17\,a_0$. Bottom three panels: $B = 525.478$ G, $a = -5.39\,a_0$. Note that the spin density inverts when the scattering length changes sign.

$$\partial_t \tilde{\mathbf{S}}(E) = \mathbf{\Omega}(E) \times \tilde{\mathbf{S}}(E) + \int dE' \tilde{g}(E', E)\, \tilde{\mathbf{S}}(E') \times \tilde{\mathbf{S}}(E), \tag{5.3}$$

For the low temperature, degenerate gas, we find that Eq. 5.3 is in excellent quantitative agreement with the spin-density profiles of Fig. 5.4 and captures very well the fine features of the data shown in Fig. 5.8, as well as the time dependence of the spin-density profiles shown in Fig. 5.9 for a fixed scattering length. The data are quite sensitive to the evolution time and exhibit a complex structure, which is very well fit by the collective spin rotation model.

Fig. 5.9 shows the measurements and predictions for the time evolution of $(n_1 - n_2)$ between $t = 0$ and 800 ms, relative to coherent excitation, for a fixed scattering length of $a = 5.23\ a0$ at $B = 528.844\ G$. The fits to these figures correspond to the evolution of the central spin density shown in Fig. 5.6, and the linear slope for the scattering length in Fig. 5.7. Here, $(n_1 - n_2)$ is given in units of the total central density $n_1(0) - n_2(0)$.

For the high temperature sample, the total atom number is $\sim 4.5 \times 10^5$, and the measured gaussian $1/e$ radius is $\sigma_x = \sqrt{2k_BT/(m\bar{\omega}_x^2)} = 325\,\mu$m, which determines $T = 45.7\,\mu$K. In this regime, we observe a noticeable difference in spin density evolution. In the measurement of zero crossing, I will explain it in more detail in Sec. 5.4.

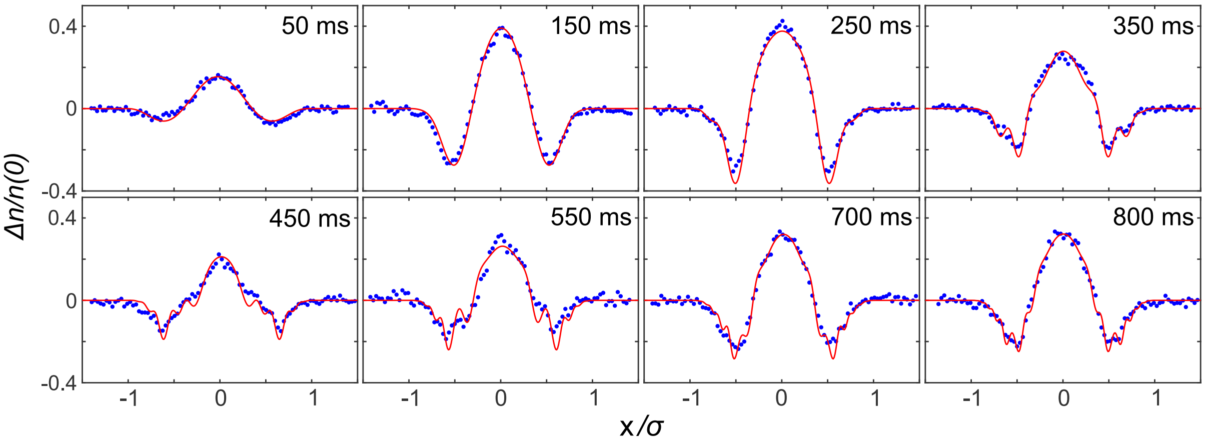

Figure 5.9: Spin density profiles (blue dots) for a degenerate sample $T/T_F = 0.28$ versus evolution time relative to coherent excitation. Each data profile is the average of 5 runs, taking in random time order. Each solid red curve is the mean field model with a fixed scattering length of $a = 5.23$ bohr ($B = 528.844$ G) and a fitted cloud size within a few percent of the average value $\sigma = 329\,\mu$m.

Table 5.1: Zero-Crossing and s-wave Scattering Tuning Rate.

States	T(μK)	B_0(G)	$B1_0$(G)	$B2_0$(G)	$a'(a_0/G)$	$a1'(a_0/G)$	$a2'(a_0/G)$
1-2	0.2	527.18(2)	534.15	527.32(25)	3.14(8)	4.12	3.49
1-2	45.7	527.42(1)	-	-	-	-	-
2-3	0.2	588.68(1)	588.92	588.75	4.52 (23)	6.11	5.82
1-3	0.2	567.98(1)	568.13	568.02	-	13.87	13.29

5.3 Measurement of Zero-Crossings

By using the spin evolution, shown in Fig. 5.3, as a sensitive probe, we can measure the magnetic field B_0 at which the scattering length vanishes. The profiles of the individual spin components remain unchanged at the zero crossing in the degenerate regime. Fig. 5.10 shows the change in axial size for each spin profile between $t = 0$ and $t = 800$ ms, as a function of magnetic field. In addition, we show the difference between the sizes of the state 1 and state 2 profiles at $t = 800$ ms. Each method gives a field value B_0 for the zero crossing. We report the mean in Table 5.1. The corresponding uncertainties are estimated as one half of the difference between the maximum and the minimum of B_0. The zero crossing for a_{12}, 527.18(2) G, is smaller than the value 527.5(2) G obtained by the same method at high temperature [Du et al., 2008], and is consistent with the calculated value 527.32(25), based on the most recent $^6\text{Li}_2$ molecular potentials determined from 1D dimer spectra [Zürn et al., 2013]. The zero crossings for a_{13},

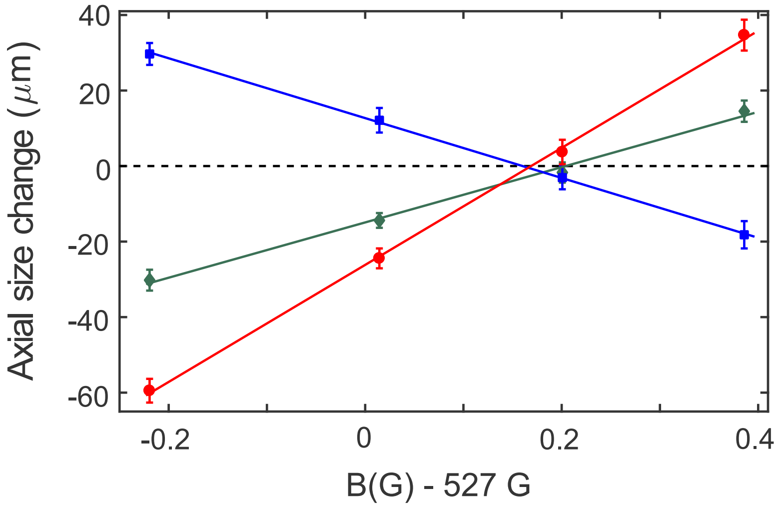

Figure 5.10: Measurement of the zero crossing field for a degenerate ^{6}Li $|1\rangle - |2\rangle$ mixture. The plots show the change in cloud size between $t = 0$ and $t = 800$ ms for state 1 (squares), state 2 (diamonds), and the difference in the cloud sizes of the two spin states at $t = 800$ ms (circles). Solid lines are corresponding linear fits, crossing zero (dashed line) when $a = 0$. Error bars denote the standard deviation of the mean of five runs.

567.98(01) G and for a_{23}, 588.68(01), listed Table 5.1, are in reasonable agreement with the values 568.07 G and 588.80 G estimated from the Feshbach resonance data of Ref. [Zürn et al., 2013], which differ only slightly from Ref. [Bartenstein et al., 2005].

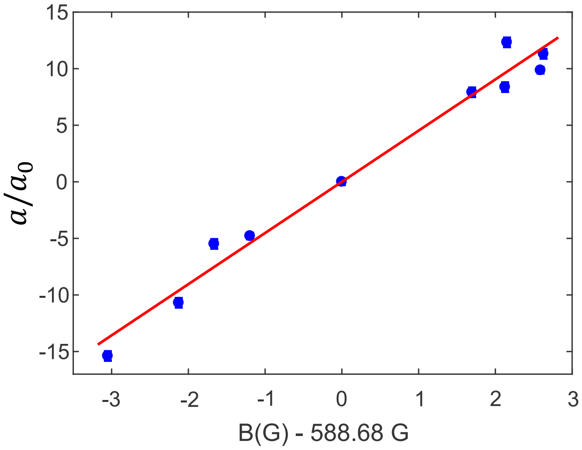

Figure 5.11: Tuning rate of the scattering length a of a $|2\rangle - |3\rangle$ mixture versus measured magnetic field ($a_0 = 1$ bohr) Error bars denote one standard deviation, obtained for each χ^2 fit to the time dependent central amplitude for the given B.

Table 5.1 compares that the tuning rates $a'_{12} = 3.14\, a_0/\mathrm{G}$ and $a'_{23} = 4.52\, a_0/\mathrm{G}$, which we obtain from the fitted scattering length versus magnetic field in the present work. Using the profiles of Ref. [Bartenstein et al., 2005], we find $a'_{12} = 4.12\, a_0/\mathrm{G}$ and $a'_{23} = 6.11\, a_0/\mathrm{G}$. These slopes are 50% larger than those estimated in the present work, but the ratios, $4.52/3.14 = 1.44$ and $6.11/4.12 = 1.48$, are in good agreement. This suggests that the discrepancy may be explained by an overall scale factor in our estimate of the transverse averaged 3D density n_{3D} (see Eq. 3.21), which determines the scattering lengths from the mean field frequencies $a \propto \Omega_{MF}$ to fit Fig. 5.6. However, using the Feshbach resonance parameters of Ref. [Zürn et al., 2013,Jul,], we estimate the tuning rate $a'_{12} = 3.51\, a_0/\mathrm{G}$, which only 11% larger than the tuning rate obtained from our experiments, and $a'_{23} = 5.82\, a_0/\mathrm{G}$, which is 29% larger.

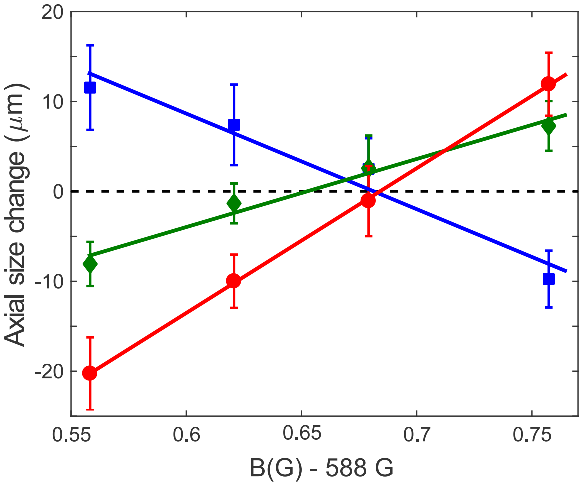

Figure 5.12: Measurement of the zero crossing field for a degenerate ^{6}Li $|2\rangle - |3\rangle$ mixture. The plots show the change in cloud size between $t = 0$ and $t = 800$ ms for state 3 (squares), state 2 (diamonds), and the difference in the cloud sizes of the two spin states at $t = 800$ ms (circles). Solid lines are corresponding linear fits, crossing zero (dashed line) when $a = 0$. Error bars denote the standard deviation of the mean of five runs.

As I mentioned earlier, we measured the zero crossing field of the scattering length for ^{6}Li for $|2\rangle - |3\rangle$, and $|1\rangle - |3\rangle$ mixtures and their corresponding tuning rate of the scattering length. Fig. 5.11 shows the data that was used to obtain the tuning rate for the $|2\rangle - |3\rangle$ mixture.

Figs. 5.12 and 5.13 similar to Figs. 5.10, show the data that was used to obtain the zero crossings fields for the $|2\rangle - |3\rangle$, and $|1\rangle - |3\rangle$ mixtures. In Fig. 5.10, Fig. 5.12, and for Fig. 5.13 we take into account cloud size variations arising from small changes in the atom number. Each data point represents an average of 5 experimental runs. For each run i, we extract the atom number N_i and the axial cloud size σ_i for each spin component. The cloud sizes scale as $N_i^{1/6}$

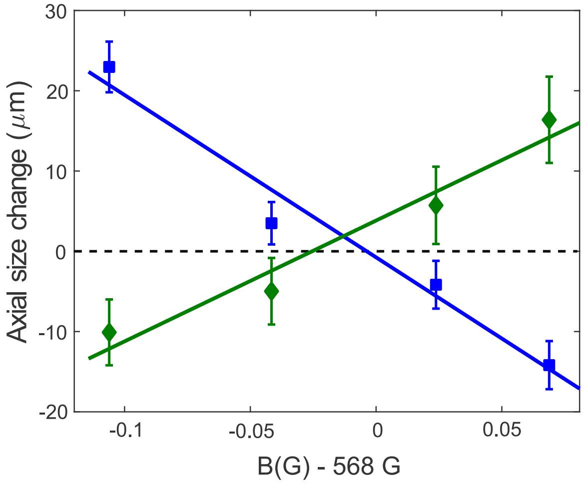

Figure 5.13: Measurement of the zero crossing field for a degenerate ^{6}Li $|1\rangle - |3\rangle$ mixture. The plots show the change in cloud size between $t = 0$ and $t = 800$ ms for state 3 (squares), state 1 (diamonds). Solid lines are corresponding linear fits, crossing zero (dashed line) when $a = 0$. Error bars denote the standard deviation of the mean of five runs.

for zero temperature Thomas-Fermi profiles. Therefore, to correct for the varying atom number, we calculate the reduced size $\sigma_i/N_i^{1/6}$ for each run and use $\left\langle \sigma_i/N_i^{1/6} \right\rangle \left\langle N_i^{1/6} \right\rangle$ as the effective mean cloud size for each bias magnetic field.

5.4 Experimental Energy Dependent shift of Zero Crossings

As discussed in Sec. 3.4, we observe the energy dependent shift in the zero crossing, by preparing a $|1\rangle - |2\rangle$ superposition at a high temperature of $T = 45.7\,\mu$K. There, we measure a shift of 0.22 G relative to the degenerate sample. This yields an energy tuning rate of 4.7 mG/μK from Eq. 3.64, confirming that the energy dependent shift is negligible for the degenerate samples, compared to the precision of the magnetic field measurement. To directly illustrate the energy dependence, we measure the spin density at $45.7\,\mu$K for $B = 527.466$ G. We see that the high temperature spin density profile crosses the zero axis four times Fig. 5.14, in contrast to the low temperature data of Fig. 5.8, which only crosses twice. The modification of the spin-density profile at high temperature is not likely to arise from the $|1\rangle - |2\rangle$ p-wave resonance in ^{6}Li, which is located near 186.2(6) G and has a width of 0.5 G [Zhang et al., 2004].

To understand this profile and the energy shift, as explained in Ch. 3, we include the energy dependence of the scattering length and of the average magnetic field, by replacing a in $\tilde{g}(E', E)$ of Eq. 3.38 with $a(E', E) = a'[B_{\rm eff}(E', E) - B_0]$, with $B_{\rm eff}(E', E)$ the effective magnetic field. Then, for small positive $B - B_0$, atoms with small energies E, E' have $B_{\rm eff} - B_0 > 0$ and

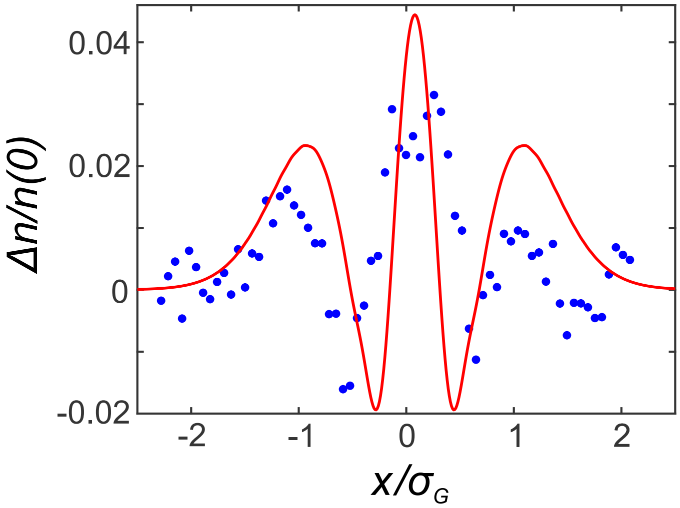

Figure 5.14: High temperature spin density profile of a $|1\rangle - |2\rangle$ mixture for $t = 400$ ms. $T = 45.7\,\mu$K and $B = 527.466$ G, where the zero-energy s-wave scattering length is 0.90 bohr. Here $\sigma_G = 323\,\mu$m is the gaussian $1/e$ radius of the total density profile.

a positive scattering length, while atoms with high energies E, E', have $B_{\rm eff} - B_0 < 0$ and a negative scattering length. These two contributions result in the extra crossings. The solid red curve of Fig. 5.14 includes the average transverse kinetic energy, which shifts the effective field from the applied value of $0.28\ G = 527.466\ G - 527.18\ G$ above the zero crossing to $0.08\ G = 0.28\ G - 0.20\ G$ above, where $a = 0.25\,a_0$ for atoms with $E = E' = 0$.

5.4.1 Spin-Density Evolution at a High Scattering Length

Increasing the scattering length to $a = -14.9\,a_0$, we measure the amplitude of the spin density at the cloud center for a degenerate sample as a function of time relative to coherent excitation, Fig. 5.15. Although the collision rate $\simeq 0.04\,s^{-1}$ is still negligible, we observe decay of the amplitude that is not predicted. We believe that the decay arises from the variation of the atom density over several runs, which are averaged to determine each data point. The average of the predictions (red curve) of Fig. 5.15 yields the observed decay, because the sensitivity to the mean field frequency, and hence to the atom density variation, increases with increasing time, resulting in a decreasing amplitude for the average.

The corresponding spatial profiles are shown in Fig. 5.16, where predicted curves, using Eq. 3.64, are obtained for a fixed scattering length of $-14.9\,a_0$, and fitting the Fermi width, within a few percent of the mean. For the larger scattering lengths, the data are sensitive to the evolution time and exhibit a complex structure. The agreement of the experimental spin density profiles with their mean-field model predictions is noticeable.

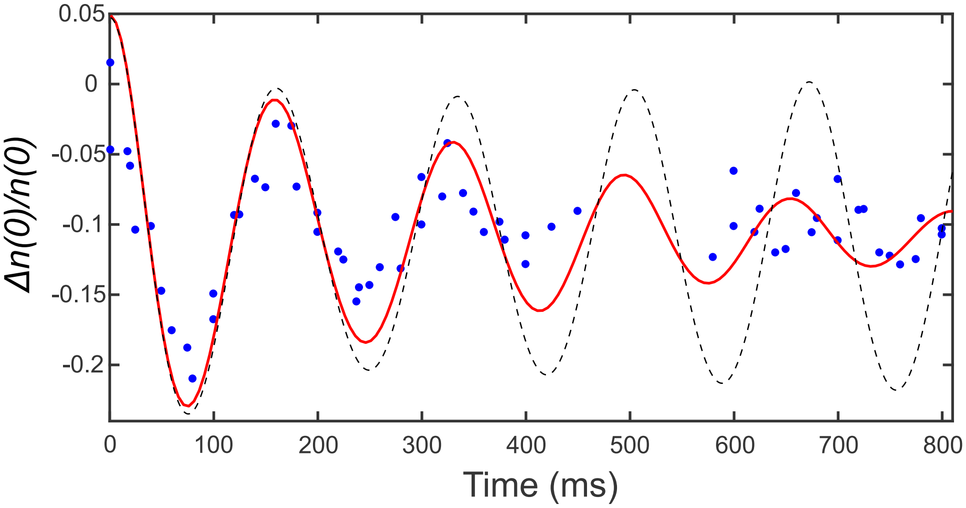

Figure 5.15: Decay of the amplitude of the central spin density versus time for $a = -14.9\,a_0$. The dashed curve shows the predicted amplitude for the average density. The red curve shows the the average of the predictions based on the measured atom numbers and cloud widths for each shot.

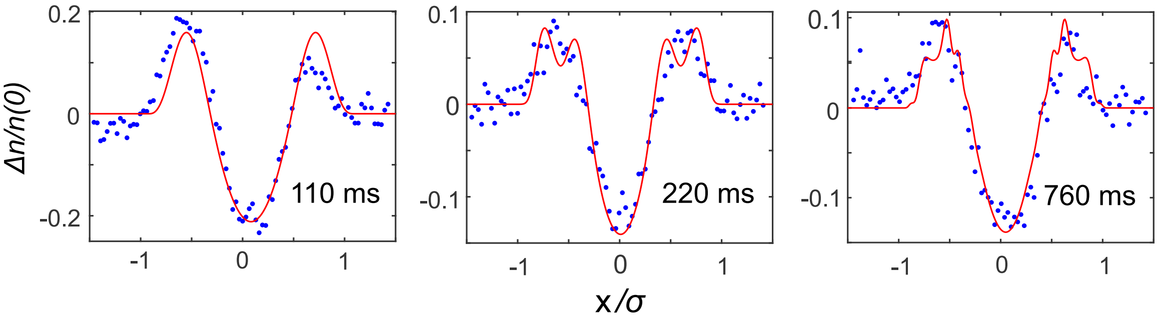

Figure 5.16: Spin density profiles versus time for $a = -14.9\,a_0$ versus predictions (red curves) with the same scattering length for each time and a fitted cloud size within a few percent of the measured average value, $\sigma = 330.6\,\mu$m.

As I mentioned earlier, to creating a coherent mixture of spins, we need a Radio-Frequency transition frequency for the magnetic field of interest. I will talk about the bias magnetic field calibration and other experimental techniques for measuring the experimental parameters in the following section.

5.5 Magnetic field Calibration

Our experiments employ mixtures of the ground Zeeman-hyperfine states of ^{6}Li, which are denoted by $|1\rangle$ to $|6\rangle$ that was introduced in Ch. 2. As shown in Fig. 5.17, the differences between Zeeman-hyperfine energy levels change in the range of magnetic fields that we employ (500 G to 1200 G). The energy differences between different states correspond to the resonance frequencies of a radio frequency (RF) pulse for the corresponding atomic transition. Since there is one to one correspondence between the magnetic field and the atomic transition frequency, we can use this property to calibrate the magnetic field in the system. As shown in Fig. 5.17, we set the radiofrequency detuning close to resonance at the field of interest, we initially find the resonance frequency for the radiofrequency pulses, by observing the transfer of atoms from state 2 to state 1 using a single 70 ms pulse. The observed linewidth is 8 Hz, half-width at half maximum (HWHM) enabling an approximate determination of the $\Delta = 0$ frequency within 5 Hz/mG of the bias field stability.

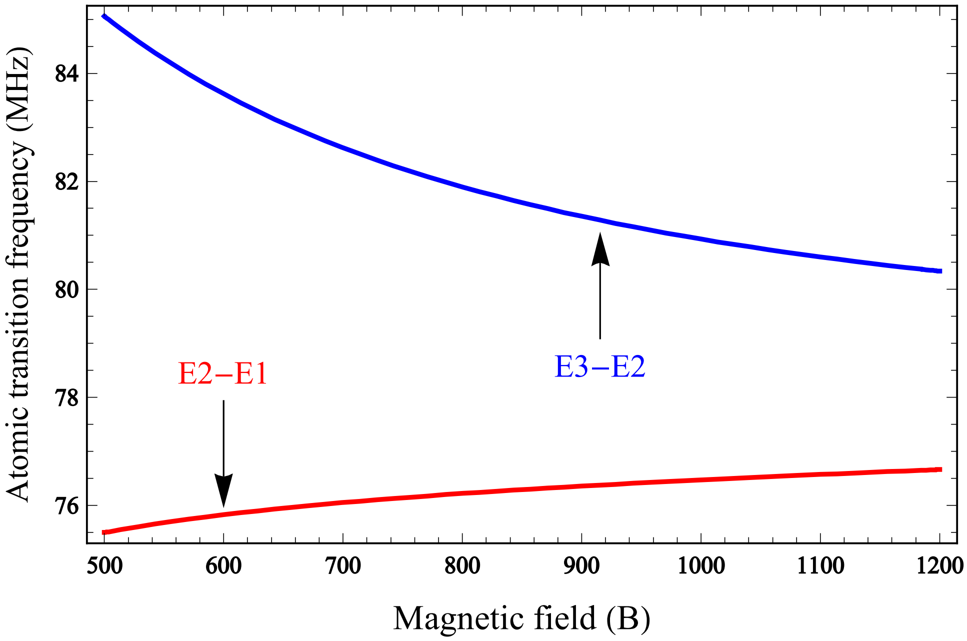

Figure 5.17: Atomic transition frequencies of ^{6}Li versus magnetic field for transition between $|1\rangle$ and $|2\rangle$, and transition between $|2\rangle$ and $|3\rangle$.

In all of experiments in this dissertation, atoms are prepared initially in the lowest two hyperfine states, $|1\rangle$ and $|2\rangle$. The energy difference between the hyperfine levels is in the 76 MHz radio frequency range. Thus, by applying an RF signal to the antenna present inside the vacuum chamber, Fig. 5.19, the atom population in the hyperfine states of ^{6}Li can be transferred. The RF antenna is primarily used for the following purposes,

(i) to create a 50-50 mixture of atoms in the two lowest hyperfine states $|1\rangle$ and $|2\rangle$.

(ii) to perform RF spectroscopy by making transitions between the hyperfine states $|1\rangle$, $|2\rangle$, and $|3\rangle$.

Fig. 5.19 shows the electronics setup used in our RF experiments. In order to create a balanced spin mixture of states $|1\rangle$ and $|2\rangle$, a noisy sine wave of frequency 9.4 MHz at 10 G is applied through an Agilent 33210A signal generator for 100 ms. In order to perform RF-spectroscopy, a Keysight N9310A RF generator produces the RF signal for atom transfer between two hyperfine states. The signals from both the Agilent and Keysight generators are sent to an RF mixer (Mini-Circuits ZX80-DR230-S+ SPDT), which selects the input based on the experiment. The output of the switch is then amplified by an RF amplifier (RSR HY3020E) and the amplified signal is sent to the antenna inside the vacuum chamber.

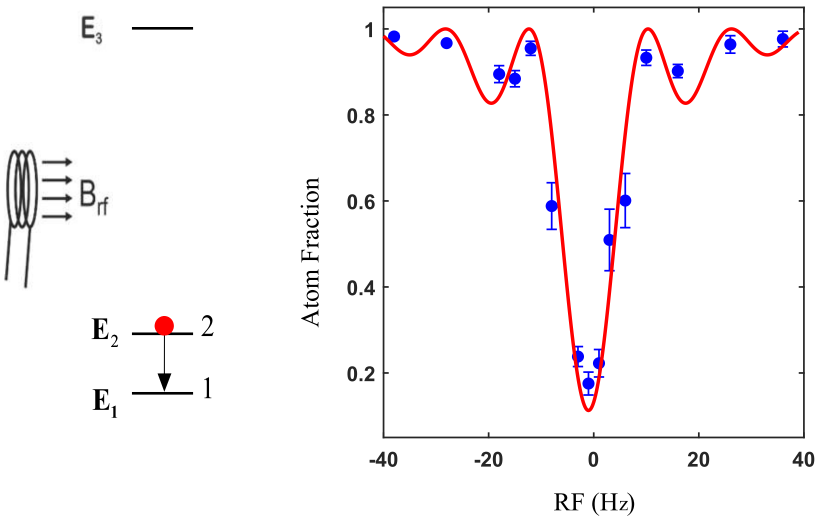

Figure 5.18: Radiofrequency spectra to measure the magnetic field stability. The red curve in the right figure is the fit from coherent excitation theory [Zhang, 2013], and blue error bars show the fraction of atoms that leaves the state $|2\rangle$, due to on resonant frequency of RF transition. The observed linewidth is 8 Hz half-width at half maximum, which is equivalent to 2 mG in terms of the magnetic field.

For the high temperature gas, we calibrated the frequencies using a parametric resonance technique in an optical dipole trap. For more information, I suggest the reader look at the previous theses in our group [Elliott, 2014, Ong, 2015]. For the degenerate case, which has been the main focus of this thesis, I created an attractive potential using an infrared beam with $\lambda = 1064$ nm [Mudiyanselage, 2019]. By releasing the atoms from the infrared attractive

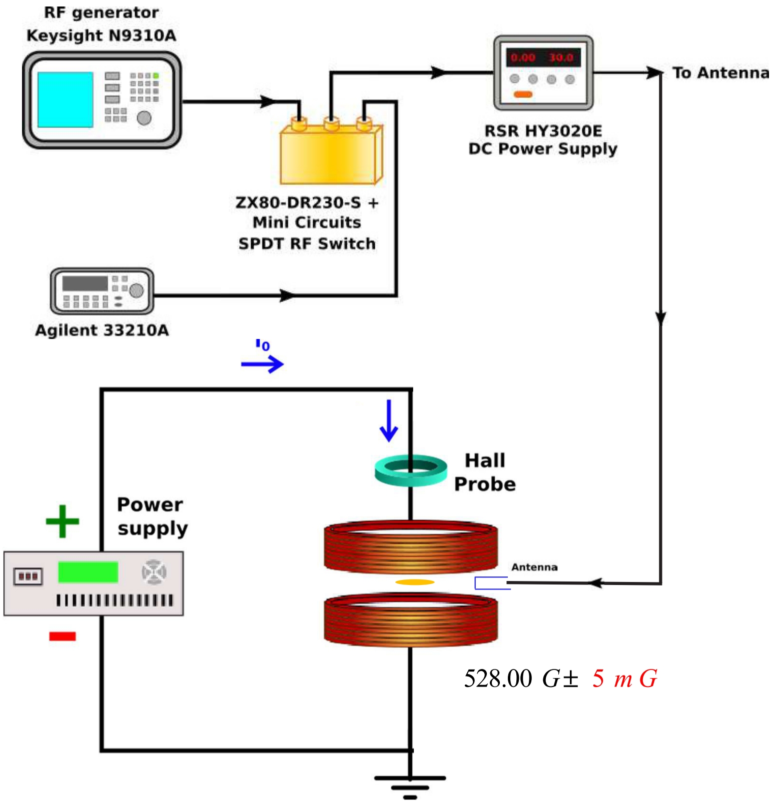

Figure 5.19: Schematic of electronics setup for the radio frequency antenna and bias magnetic field.

potential, to the $CO2$ dipole trap combined with the magnetic bowl trap, we can monitor the axial size width change versus the time that the infrared potential is off. As shown in the Fig. 5.20, the frequency along the x-axis for 2 % $CO2$ trap depth (axial frequency) is 23 Hz ± 0.25. The transverse frequency at this trap depth is 625 Hz is measured by the parametric resonance method.

The geometry of our magnets (Fig. 3.6) allows for the measurement of single oscillation frequency to describe the magnetic potential in all three directions. The large size of the magnet coils relative to the atomic cloud creates a harmonic potential for the confined atoms. From elementary magnetostatics, we can relate the oscillation frequency along the single direction (axial) to the remaining two (radial) as following

$$\omega_{mag}^2 = \omega_{z\ \mathrm{mag}}^2 = \omega_{y\ \mathrm{mag}}^2 = \frac{1}{2}\omega_{x\ \mathrm{mag}}^2. \tag{5.4}$$

For the magnetic bowl frequency, I used the attractive potential again in presence of the $CO2$ dipole trap at $B = 832.2\ G$. Assuming U_{mag} is linear in applied B and quadratic in ω_{mag},

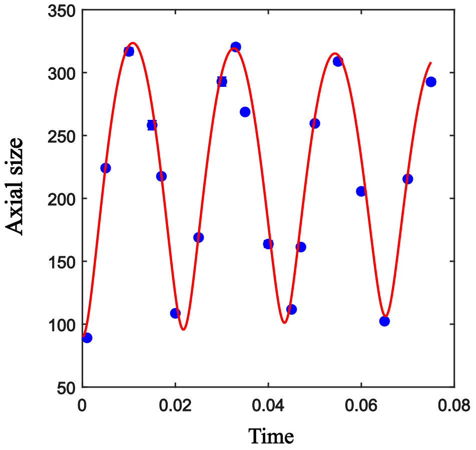

Figure 5.20: Axial cloud size change in μm as a function of the released time from the infrared potential. The oscillation frequency shown by the red curve is 23 Hz ± 0.25 Hz.

we write ω_{mag} at an arbitrary magnetic field as

$$\omega_{\text{ mag}} = \omega_{\text{ mag } 832.2}\sqrt{\frac{B(G)}{832.2}} = 20.5 \times 2\pi\sqrt{\frac{B(G)}{832.2}} \tag{5.5}$$

For the weakly-interacting regime in 1-2 mixture, that we use in our system, the magnetic bowl frequency is 16.3 Hz.

In summary, we have shown that a mean field collective spin rotation model, including the full energy-dependent coupling matrix, quantitatively describes the spin density evolution in the collisionless regime, precisely testing the underlying energy-space spin-lattice model. The measurements provide an essential benchmark for future work on collective spin evolution with designer energy landscapes in the weakly interacting regime.

Chapter 6

Measurement of Energy-Resolved Information Scrambling

In this chapter, I demonstrate a new protocol for measuring the information scrambling in a large many-body system. Using the out-of-time-order correlation (OTOC) functions in Ch. 3, I extract energy-resolved out-of-time-order correlation functions and many-body coherence from the spatial profiles of the spin density using an inverse Abel-transform method. From this study, we reveal a coherence structure that is hidden in measurements of the total collective spin vector.

6.1 Experimental Many-body Spin Protocol

The experimental protocol that we apply for measuring OTOC functions, is shown in Fig. 6.1. With this protocol, we define a rotation operator $\hat{W}$ and a measurement operator $\hat{V}$ operator in a large system, see Sec. 4.1. To remind the reader, $\hat{W}$ applies a rotation to the total interacting spin system in between the forward and time-reversed evolutions. The operator $\hat{V}$ performs a measurement to diagnose the effects of the rotation on the spins of energy E_i, i.e., at "site" i in energy space.

We employ a degenerate, weakly interacting cloud of ^{6}Li with the total atom number of $N = 6.5 \times 10^4$, in a bias magnetic field near 527.18 G (zero-crossing of $1-2$ mixture), where the s-wave scattering length a vanishes. The optical trap that we use for this experiment, has the same oscillation frequency parameters as mentioned in Sec. 5.5. By fitting a finite temperature Thomas-Fermi profile to the measured total spatial density, we find that $T/T_F = 0.32$, where the Fermi temperature for our trap parameters is $T_F = 0.70\,\mu$K and the corresponding Thomas-Fermi radius, which is calculated through $h(6N\nu_x\nu_r^2)^{1/3} = \frac{1}{2}m\omega_x^2\sigma_{TF}^2$, yields $\sigma_{TF} = 305\,\mu$m. By fitting a zero-temperature spatial profile to the measured total spatial density, we find an effective Thomas-Fermi radius, $\sigma = 345\,\mu$m, which is used in the mean field model of Ch. 3, [Pegahan et al., 2019]. The scattering length is determined by measured tuning rate of $3.14\,a_0/G$ of Sec. 5.3 and the bias magnetic field, which is precisely measured by rf spectroscopy, as explained in Sec. 5.5.

To implement the many-body echo protocol shown in Fig. 6.1, we prepare a z-polarized initial state $|1\rangle \equiv |\uparrow_z\rangle$ and $|2\rangle \equiv |\downarrow_z\rangle$ in a cloud of ^{6}Li with all atoms in the spin-down hyperfine state $|2\rangle$. Similar to the previous chapter, we prepare fully polarized state from a 50-50 mixture of the two lowest hyperfine states, denoted as $|1\rangle$ and $|2\rangle$, which is evaporatively cooled to degeneracy near the $|1\rangle - |2\rangle$ Feshbach resonance at 832.2 G. The magnetic field is then ramped to the weakly interacting regime near 1200 G, and the $|1\rangle$ spin component is eliminated by means of a resonant optical pulse. Then the bias magnetic field is ramped near 527.18 G, where the s-wave scattering length vanishes. We start with the fully z-polarized state $|\downarrow_{z1}\downarrow_{z2}\dots\downarrow_{zN}\rangle \equiv |\psi_{z0}\rangle$ in a bias magnetic field $B_1 = 528.53$ G, which selects an initial scattering length $a_1 \equiv a = 4.24\,a_0$.

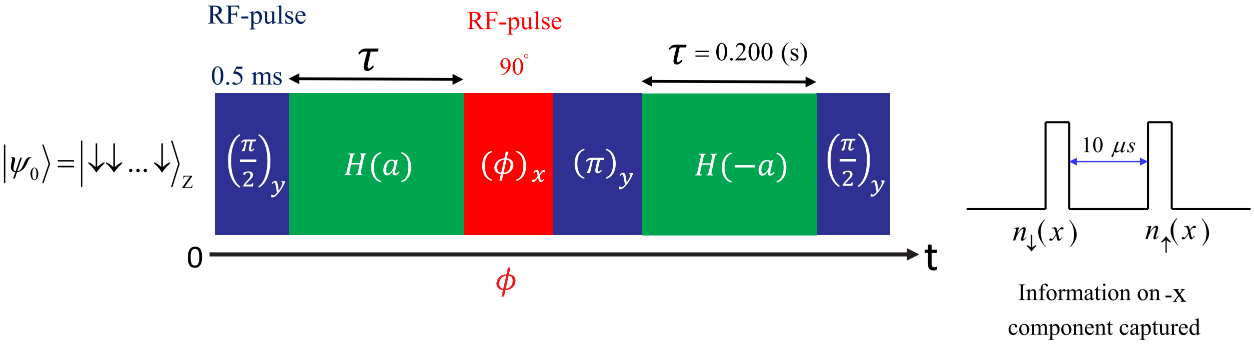

Figure 6.1: Energy-resolved out-of-time-order correlation measurement. The system is initially prepared in a pure state, with the spins for atoms of energy $E_1, E_2, \dots E_N$ polarized along the $-z$ axis. After the pulse sequence, we measure the spatial profiles of the $|\uparrow_z\rangle$ and $|\downarrow_z\rangle$, lowest two hyperfine states ^{6}Li, with 10 μs delay for each spin by an absorption imaging method; "single-shot" spin density profile $S_z(x) = n_{\downarrow_z}(x) - n_{\uparrow_z}(x)$. For this measurement, $\phi = \pi$, $a = 4.24\,a_0$, and $\sigma = 345\,\mu$m.

In the ideal case, where detuning $\Delta = 0$, we apply a 0.5 ms radio-frequency $(\pi/2)_y$ pulse (defined to be about the y-axis), which is resonant with the $|\downarrow_z\rangle \rightarrow |\uparrow_z\rangle$ transition. Thus, at the bias field B_1, we produce an initial x-polarized N-atom state as

$$|\psi_0\rangle = e^{-i\frac{\pi}{2}S_y}|\psi_{z0}\rangle = |\uparrow_{x1}\uparrow_{x2}\dots\uparrow_{xN}\rangle. \tag{6.1}$$

We discuss the effect of finite detuning in Sec. 6.3.1. After preparing the initial state, the system evolves for a time $\tau = 200$ ms at the initial bias magnetic field $B_1 = 528.53$ G. Then, a resonant radio-frequency pulse $(\phi)_x$, shifted in phase (see Sec. 6.4) from the first pulse by $\pi/2$, rotates the N-atom state about the x-axis by a chosen angle ϕ. Immediately following this rotation, we reverse the sign of the Hamiltonian by applying a $(\pi)_y$ pulse and tuning the bias magnetic field to a value $B_2 = 525.83$ G, where the scattering length $a_2 = -a$. After an additional $\tau = 200$ ms, the bias magnetic field is swept back to its original value B_1 over 5 ms and a final $\pi/2$ rotation about the negative y-axis is applied. The density profiles of both spin components are then immediately measured for a single cloud, using two camera resonance pulses separated by $10\,\mu$s Fig. 6.1. This defines a *single-shot* measurement. Subtracting the integrated consecutive shots yields the single-shot z-component of the collective spin vector density $S_z(x)$, which in the ideal case, corresponds to the x-component just prior to the final $(\pi/2)_y$ pulse.

Magnetic field sweep from B_1 to B_2 is accomplished using a set of low inductance coils, wound concentric with the primary bias field coils in Fig. 6.2.

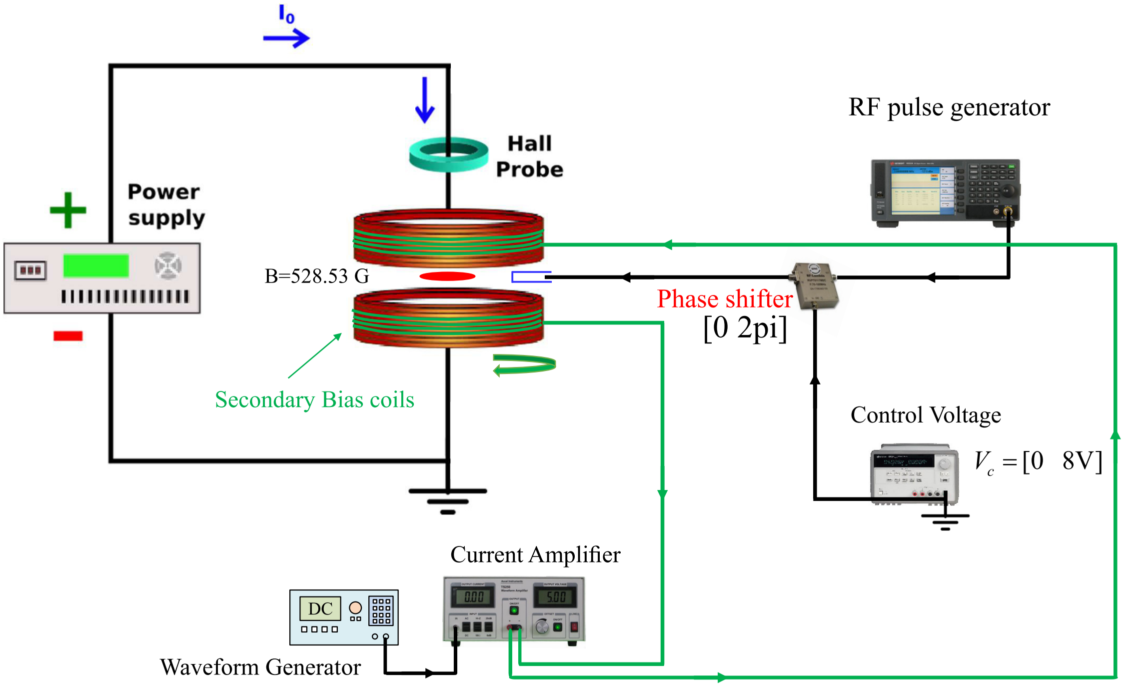

Figure 6.2: Schematic of the phase shifter and secondary bias coil for a small change of magnetic field.

6.1.1 Reversing the Sign of the Hamiltonian

Here, I will explain how the sign of Hamiltonian in this system can be inverted by reversing the sign of s-wave scattering length followed by a π pulse. The Hamiltonian for the system of spins in the energy space is

$$H(\pm\, a) = -\sum_{i} \Omega_{z\mathrm{i}} s_{z\mathrm{i}} \pm a \sum_{i\ j\neq i} g_{\mathrm{ij}}\ \vec{s}_{\mathrm{i}}.\vec{s}_{\mathrm{j}}\ . \tag{6.2}$$

The final state of the N-atom system after the pulse sequence of Fig. 6.1(a) can be written as

$$|\psi_f\rangle \;=\; e^{-i\frac{\pi}{2}S_y} e^{-iH(-a)\tau} e^{-i\pi S_y} e^{-i\phi S_x} e^{-iH(+a)\tau} e^{-i\frac{\pi}{2}S_y} \left|\psi_z\right\rangle, \tag{6.3}$$

where $S_x = \sum_{j,\alpha_j}^{N} s_{xj}$ is the x-component of the *total* spin vector and $|\psi_0\rangle$ the fully x-polarized state. As shown above, with the last $\frac{\pi}{2}$ pulse, we rotate the total spin vector along the y-direction. Next, from $\hat{1} = e^{-i\pi s_y} e^{i\pi s_y}$, Eq. 6.3 leads to

$$\begin{aligned} |\psi_f\rangle \;&=\; e^{-i\frac{\pi}{2}S_y} e^{-i\pi S_y} e^{i\pi S_y} e^{-iH(-a)\tau} e^{-i\pi S_y} e^{-i\phi S_x} e^{-iH(+a)\tau} \left|\psi_0\right\rangle \\ |\psi_f\rangle &= \tilde{O}\ e^{-i\phi S_x} e^{-iH(+a)\tau} \left|\psi_0\right\rangle \\ \tilde{O} &= e^{-i\frac{3\pi}{2}S_y} e^{i\pi S_y} e^{-iH(-a)\tau} e^{-i\pi S_y}. \end{aligned} \tag{6.4}$$

Now that we have the new form of the final state, I will show what happens to the Hamiltonian with a revered s-wave scattering length and a rotation about the y-axis by an angle θ. From Eq. 6.2, the second term on the right hand side commutes with $e^{-i\theta S_y}$ since $[S_y, \vec{s}_i.\vec{s}_j] = 0$. Thus the Hamiltonian under a rotation about the y-axis will be

$$\hat{O} = e^{i\theta S_y} H(-a) e^{-i\theta S_y} = -\sum_{i} \Omega_{zi}\ e^{i\theta S_y} s_{zi}\ e^{-i\theta S_y} - g_{\mathrm{ij}}\ \vec{s}_{\mathrm{i}}.\vec{s}_{\mathrm{j}}\ = s_{zi}(\theta). \tag{6.5}$$

We need to simplify the first term on the right hand side of Eq. 6.5. From the Heisenberg equation of motion, we have

$$\begin{aligned} &\mathrm{d}\hat{O}/d\theta = ie^{i\theta S_y}[S_y, s_{zi}]e^{-i\theta S_y} = -s_{xi}(\theta) \\ &\mathrm{d}^2\hat{O}/d\theta^2 = -ie^{i\theta S_y}[S_y, s_{xi}]e^{-i\theta S_y} = -s_{zi}(\theta). \end{aligned} \tag{6.6}$$

Therefore, we have the second-order differential equation as

$$\mathrm{d}^2\hat{O}/d\theta^2 + \hat{O} = 0, \tag{6.7}$$

with initial conditions of

$$\begin{aligned}\hat{O}(0) &= s_{zi} \\ \mathrm{d}\hat{O}/d\theta(0) &= -s_{xi}. \end{aligned} \tag{6.8}$$

By solving Eq. 6.7, we have the following relation for spin operator under the rotation θ

$$s_{zi}(\theta) = s_{zi}\cos(\theta) - s_{xi}\sin(\theta). \tag{6.9}$$

Now if $\theta = \pi$, as the case for our protocol, $s_{z\,i}(\theta) = -s_{zi}(\theta)$. If we substitute Eq. 6.9 in Eq. 6.5,

$$e^{i\pi S_y} H(-a) e^{-i\pi S_y} = +\sum_i \Omega_{zi}\; s_{zi} \; - g_{ij}\; \vec{s}_{\mathrm{i}}.\vec{s}_{\mathrm{j}} \tag{6.10}$$

and therefore, the sign of Hamiltonian is inverted

$$e^{i\pi S_y} H(-a) e^{-i\pi S_y} = -H(+a) \tag{6.11}$$

through applying a π pulse accompanied with changing the sign of the scattering length from $a = 4.24\; a_0$ to $a = -4.24\; a_0$. We implement this fast change of scattering length (bias magnetic field) through the secondary bias coil, shown in Fig. 6.2. As the result of Eq. 6.11, the final state $|\psi_f\rangle$ state in Eq. 6.4 can be simplified with

$$e^{i\pi\,\mathrm{S}_y} e^{-iH(-a)\,\tau} e^{-i\pi\,\mathrm{S}_y} = e^{+iH(+a)\,\tau}, \tag{6.12}$$

which leads to

$$|\psi_f\rangle = e^{-i\frac{3\pi}{2}S_y} W_\phi(\tau)|\psi_0\rangle. \tag{6.13}$$

Here the W-operator is defined by

$$W_\phi(\tau) = e^{iH(+a)\tau} e^{-i\phi\, S_x} e^{-iH(+a)\tau}. \tag{6.14}$$

This operator, similar to the general operator W in

$$\frac{1}{2}\langle\psi_0||[W,V]|^2|\psi_0\rangle = 1 - Re\{\mathcal{F}\}, \tag{6.15}$$

applies the rotation to the ensemble of spins in between forward and the backward time evolution. In the experiments, we determine $\mathcal{F}$ by measuring the sum of z-components of the spin for a selected group of atoms with the same energy. We define $s_{z\alpha_i}$ as the z-component for a single atom. Here α_i comprises the 3-D vibrational quantum numbers (n_i, n_y, n_z) of a single state, with $n_i + 1/2 = E_i/h\nu_x$ specified for x-direction.

The measurement process, to diagnose the effect of the rotation, is done as the following. After the pulse sequence, the spin densities $n_{\uparrow z}(x)$ and $n_{\downarrow z}(x)$ are measured for a single cloud using two resonant absorption images, separated in time by 10 μs. The measured z-component of a single spin in state α_i, shown in Fig. 4.3, is $\langle\psi_f|s_{z\alpha i}|\psi_f\rangle = \langle\psi_0|W_\phi^\dagger(\tau)s_{x\alpha i}W_\phi(\tau)|\psi_0\rangle$ resulted from Eq. 6.13 and Eq. 6.9,

$$e^{i\frac{3\pi}{2}S_y}\,s_{z\alpha i}\,e^{-i\frac{3\pi}{2}S_y} = s_{x\alpha i}. \tag{6.16}$$

Here s_{xi} acts as the V operator in Eq. 6.15, see Ch. 4 for more detail. If we choose $V = 2\,\hat{s}_{x\alpha i} = \hat{\sigma}_{x\alpha i}$, i.e., the x-Pauli matrix for the single spin, commutes with S_x and hence with $W_\phi(0)$. With this choice, $V^\dagger = V$ and $V^\dagger V = \sigma_x^2 = \hat{1}$ as required from Eq. 6.15. Thus, we can conclude that $\langle\psi_f|\hat{s}_{z\alpha i}|\psi_f\rangle$ is of the same form as out-of-time-order correlation function. Furthermore, since $(V = \sigma_x)|\psi_0\rangle = |\psi_0\rangle$,

$$\mathcal{F}_{\alpha i} \equiv 2\,\langle\psi_0|W_\phi^\dagger(\tau)s_{x\alpha i}W_\phi(\tau)|\psi_0\rangle = 2\langle\psi_f|s_{z\alpha i}|\psi_f\rangle, \tag{6.17}$$

where $\mathcal{F}_{\alpha i}$ is OTOC function for a single spin in state α_i. In Sec. 6.2, we will use Eq. 6.17 and Eq. 4.11 from Ch. 4, to compare the experimental OTOC for information scrambling with theoretical predictions in the many-body system of spins.

6.2 Energy-Resolved OTOC Measurement

Experimentally, we measure $\mathcal{F}_{\alpha i}$ with αi summed over a subset N_s spins with nearly the same energy. This quantity determines the ϕ-dependent, energy-resolved, mean-square commutator using 4.13 and 4.11 as,

$$\frac{1}{N_s}\sum_{\alpha i=1}^{N_s}\langle\psi_0|[\hat{W}_\phi(\tau),\hat{s}_{x\alpha i}]|^2|\psi_0\rangle = \frac{1}{2} - \frac{1}{N_s}\sum_{i=1}^{N_s}\langle\psi_f|\hat{s}_{z\alpha i}|\psi_f\rangle. \tag{6.18}$$

Restricting the OTOC measurement to atoms with energies within ΔE of a chosen energy E, the second term on the righthand side of Eq. 6.18, $S_z(E)\,\Delta E/[n(E)\,\Delta E]$, will be

$$\mathcal{F}(E,\phi) \equiv \frac{1}{2}\,\frac{n_{\uparrow_z}(E,\phi) - n_{\downarrow_z}(E,\phi)}{n_{\uparrow_z}(E,\phi) + n_{\downarrow_z}(E,\phi)}, \tag{6.19}$$

where $\mathcal{F}(E,0) = 1/2$. $n(E) = n_{\uparrow_z}(E,\phi) + n_{\downarrow_z}(E,\phi)$ in the denominator is independent of ϕ, and comes from inverse-Abel transform of spin densities in x-space as

$$n(x,t) = \frac{\bar{\omega}_x}{\pi}\int_0^\infty dp_x\, n\left(\frac{p_x^2}{2m} + \frac{m\bar{\omega}_x^2}{2}x^2, t\right). \tag{6.20}$$

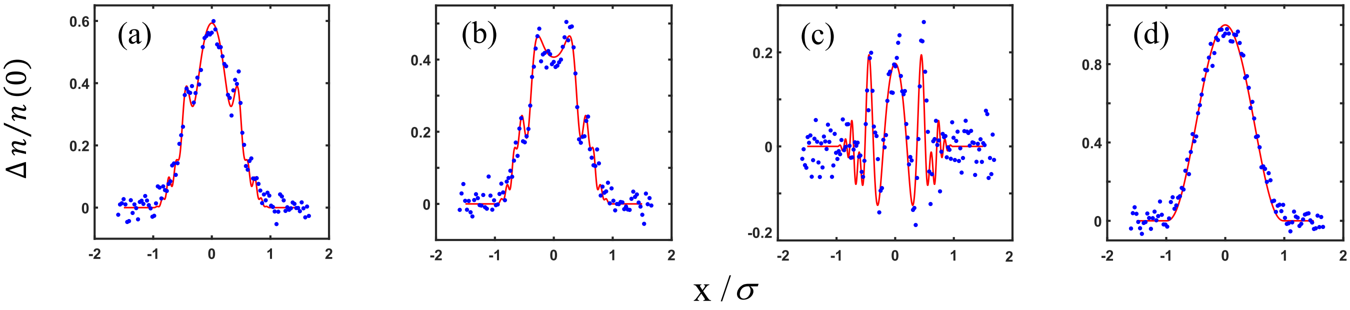

Figure 6.3: Spin density profiles measured for a single shot with $a = 4.24\,a_0$ and $\phi = \pi$ (blue dots) in units of the central density $n(0)$. (a) $n_\uparrow(x, \phi = \pi)$; (b) $n_\downarrow(x, \phi = \pi)$; (c) Difference of the density profiles $S_z(x, \phi = \pi) = \frac{1}{2}[n_\uparrow(x, \phi = \pi) - n_\downarrow(x, \phi = \pi)]/n(0)$; (d) Total density $n(x) = n_\uparrow(x, \pi) + n_\downarrow(x, \pi)$ in units of the central density $n(0)$. Despite the complex spatial structure in the individual spin density profiles, the total density remains thermal. The red curves show the predictions of the mean field model of Ref. [Pegahan et al., 2019] using a scattering length 2.35 times the measured value of $4.24\,a_0$ and a global detuning of 0.27 Hz, i.e., $\Delta = 2\pi \times 0.27$ rad/s.

To illustrate these ideas, Fig. 6.3 shows the single-shot spin density profiles taken after the full OTOC pulse sequence of Fig. 6.1 with $a = 4.24\,a_0$ and $\phi = \pi$ (blue dots). Despite the complex structure observed in the spatial profiles for the individual spin densities (a) and (b), which arises from spin coherence, the total density, shown on the right hand side, remains in a thermal distribution. Similar to Ch. 5, the thermal distribution is consistent with the assumption of no energy-space coherence between harmonic states with different energies.

We capture the spin-densities from absorption imaging method after each cycle of the pulse sequence with a chosen rotation angle ϕ, to determine the spatial profiles $n_{\uparrow z}(x, \phi)$ and $n_{\downarrow z}(x, \phi)$ of single clouds. In Sec. 6.4, I will explain in detail how we control the ϕ from 0 to 2π.

To reveal the corresponding profiles in energy space, as needed to measure $\mathcal{F}(E, \phi)$, we again assume that there is no energy-space coherence, i.e., the average z-component of the c-number spin density is given by,

$$S_z(x) \equiv \langle \hat{S}_z(x) \rangle = \sum_E |\phi_E(x)|^2 \langle \hat{S}_z(E) \rangle. \tag{6.21}$$

For a harmonic trap, the $\phi_E(x)$ are harmonic oscillator states, and the equation for $S_z(E)$, in a continuous limit, corresponds to an integral Abel-transform that can be inverted, as shown in Eq. 6.20. This method is based on the principle of Fourier-analysis (the unknown function, such as $S_z(E)$, is expanded in a series of cosine-functions) similar to Fourier series.

In the next sections, I will explain how to extract information about out-of-time order correlation functions for a microscopic ensemble of spins with the same energy that summed over all energies.

6.2.1 Measuring OTOC for Collective Spin Vectors in Energy-Space

We can extract information about the many-body coherence from Eq. 6.18, by writing the sum on the right-hand side as

$$\frac{1}{N_s}\sum_{i=1}^{N_s}\langle\psi_0|\hat{W}^{\dagger}_{\phi}(\tau)\hat{s}_{xi}\hat{W}_{\phi}(\tau)|\psi_0\rangle = \sum_m e^{im\phi}\,B_m. \tag{6.22}$$

Non-vanishing coefficients B_m correspond to coherence between states for which the x-component S_x of the total angular momentum differs by m [Gärttner et al., 2018, Sup,], as explained in more detail in the next section. Since the right side of Eq. 6.22 is real, $B_{-m} = B_m^*$, we can expand Eq. 6.19 for the measured, energy-selected average in the form of

$$\mathcal{F}(E,\phi) = B_0 + \sum_{m\geq 1} 2|B_m|\cos(m\phi + \varphi_m). \tag{6.23}$$

In fitting the data with Eq. 6.23, we restrict the range of m to 4. We find that the fits are not improved by further increase of m, consistent with the limited number of ϕ values measured in the experiments.

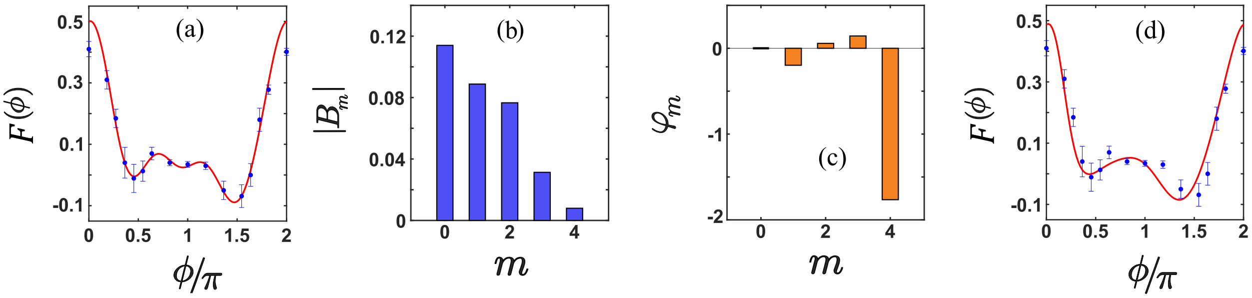

Figure 6.4: Total collective spin projection S_z versus rotation angle ϕ without energy restriction. (a) $F(\phi) = \frac{1}{2}(N_\uparrow - N_\downarrow)/(N_\uparrow + N_\downarrow)$ (blue dots) for a scattering length $a = 4.24\,a_0$. The red curve is the fit of Eq. 6.23, which determines the magnitudes of the coherence coefficients $|B_m|$ (b) and corresponding phases φ_m (c); (d) Fit (red curve) of the mean field model of Ref. [Pegahan et al., 2019] to the data (blue dots), using a scattering length 2.63 times the measured value and a global detuning $\Delta = 0$.

Fig. 6.4(a) shows $F(\phi) = \frac{2}{N}\langle\psi_0| W_\phi^\dagger(\tau) S_x W_\phi(\tau) |\psi_0\rangle$ for the total number of atoms, measured without energy resolution. In this case, Eq. 6.19 yields

$$\mathcal{F}(E,\phi) \to F(\phi) \equiv \frac{1}{2}\,[N_\uparrow(\phi) - N_\downarrow(\phi)]/[N_\uparrow(\phi) + N_\downarrow(\phi)], \tag{6.24}$$

with $N_\uparrow$ and $N_\downarrow$ the total atom numbers in each spin state. The data (blue dots) are an average of 6 repetitions of the entire ϕ sequence, with a fixed scattering length $a = 4.24\,a_0$. Fig. 6.4(a) (red curve) shows the fit of Eq. 6.23 to the measured $F(\phi)$, which determines the magnitude (b) and phase (c) of the coherence coefficients $B(m)$.

We can compare the ϕ-dependent data of Fig. 6.4 to the mean field model of Ch. 3, which predicts the red curve shown in Fig. 6.4(d). For the mean field model, we take the global detuning $\Delta = 0$. However, the model requires a scattering length that is 2.63 times larger than the measured value to fit the observed ϕ dependence. If we keep the scattering length at the measured values, the mean-field model, as shows in Fig. 6.5, can not capture the energy ϕ-dependent data.

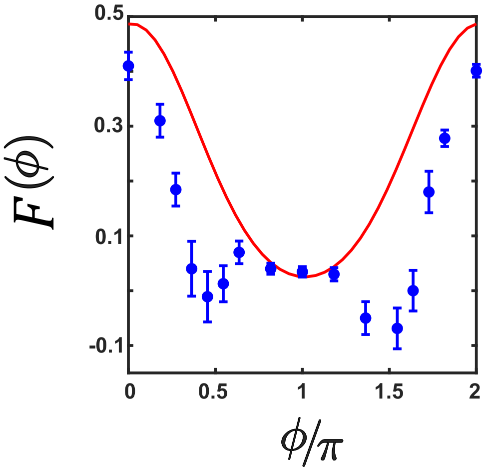

Figure 6.5: Total collective spin projection S_z versus rotation angle ϕ without energy restriction. The red curve shows the fit of the mean-field model for the measured scattering length of $a = 4.24\,a_0$.

The reason that the blue data points do not reach to the maximum value of 0.5 is that, the RF-resonance frequency at the final magnetic field $B_1 = 528.53$ G, see Sec. 6.1, detuned by few Hz during the forward and backward time evolution. Thus, we transfer about 90 % atoms back to their original state $|1\rangle$.

6.2.2 Measuring OTOC functions for a Subset of Spins in Energy-Space

Using the same data as the previous section, we measure the energy-resolved OTOC $\mathcal{F}(E, \phi)$, as shown in Fig. 6.6, for an ensemble of spins with a same axial energy E_x. The top row of Fig. 6.6 shows the ϕ dependence for several different energies E. The shapes of the profiles vary significantly with axial energy, which is in E_F unit, changing in symmetry and structure as the energy is varied from $E = 0$ to $E = 0.7\,E_F$. The red curves in the first row show the fit of Eq. 6.23, which yields the magnitudes of the coherence coefficients $|B_m|$ shown in the second row and the corresponding phases φ_m shown in the third row. In the last row, we again compare the data to the predictions of the mean field model of Ref. [Pegahan et al., 2019]. Using the detuning as a free parameter, the mean field model is able to capture the complex ϕ-dependent shapes of the data. However, to fit the observed ϕ dependence, the model requires a scattering length $a_{eff} \equiv 2.63\,a$, i.e., 2.63 times larger than the measured value $a = 4.24\,a_0$.

6.3 Effect of the Detuning on the Mean-Field model

The ideal implementation of the protocol of Fig. 6.1, as described above, assumes a global detuning $\Delta = 0$. In the actual experiments, the global detuning Δ is near resonance at the initial bias magnetic field B_1, but changes by several kHz when, as shown in Fig. 6.2, the bias magnetic field is tuned to B_2 for 200 ms. This results in a large, but reproducible phase shift. To compensate, we choose the time for the final $\pi/2$ pulse to be delayed by a time τ_f of several ms after we begin the sweep of the magnetic field from B_2 back toward its original value B_1 as the detuning becomes small $\simeq$ 100 Hz, well within the pulse bandwidth, but nonzero.

This provides adequate time for the frequency detuning to return to a nonzero value well-within the pulse bandwidth. In this final low frequency detuning region, we find that a delay of $\tau_f = 10$ ms produces a stable net phase shift of 180^o (modulo 2π) and a maximum transfer of atoms from the initially populated state 2 to the initially unpopulated state 1 for $\phi = 0$, i.e., a $-\pi/2$ pulse about the y-axis as noted above. The negative sign is taken into account in the data analysis.

To set the radiofrequency detuning close to resonance at the field B_1, we initially find the resonance frequency for the radiofrequency pulses, by observing the transfer of atoms from state 2 to state 1 using a single 50 ms pulse. The observed linewidth is 8 Hz half width at half maximum, enabling an approximate determination of the $\Delta = 0$ frequency within 1 Hz. To keep the rf frequency nominally on resonance as data is collected, for each choice of ϕ, we consistently check that the $\phi = 0$ configuration produces maximum transfer of atoms from state 2 to state 1 at the end of the 400 ms total sequence. If not, the rf frequency is slightly changed to compensate for magnetic field drift, which changes the resonance frequency by $\simeq$ 3.6 Hz/mG.

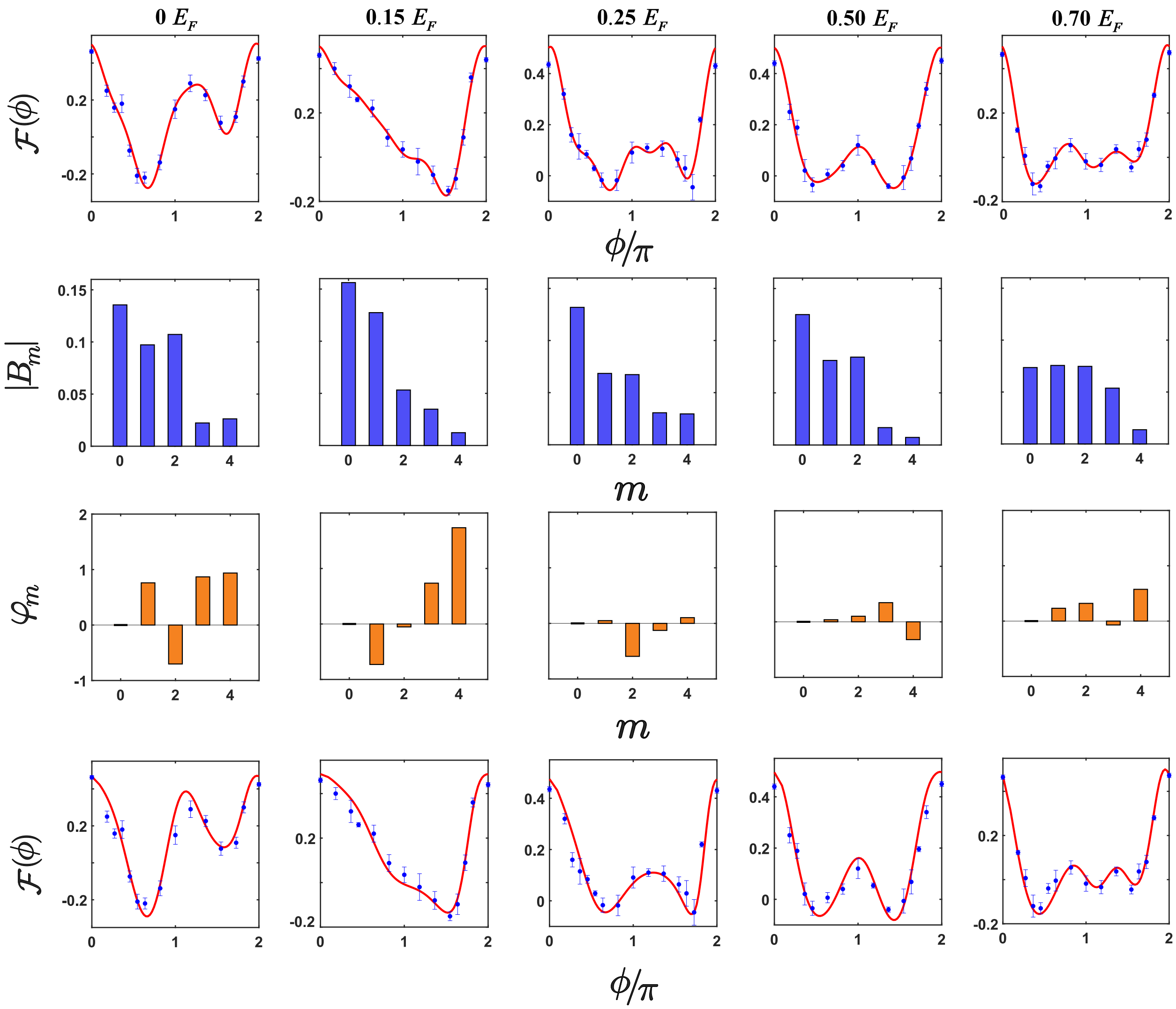

Figure 6.6: Energy-resolved collective spin projection $S_z(E)$ versus rotation angle ϕ for spins of selected energies (left to right) $E/E_F = 0, 0.15, 0.25, 0.5, 0.7$. Here, $\mathcal{F}(\phi) = \frac{1}{2}[n_\uparrow(E) - n_\downarrow(E)]/[n_\uparrow(E) + n_\downarrow(E)]$. The top row shows the data (blue dots) for a measured scattering length $a = 4.24\,a_0$. The red curve is the fit of Eq. 6.23, which determines the magnitudes of the coherence coefficients $|B_m|$ (second row) and corresponding phases φ_m (third row); The bottom row shows the predictions (red curves) of the mean field model of Ref. [Pegahan et al., 2019] to the data (blue dots), using a scattering length 2.63 times the measured value and global detunings, ordered in energy, of $\Delta(\text{Hz}) = 0,\ 0.8,\ 0.65,\ -0.8$, and 0.15.

However, it is not possible to control the detuning at the Hz or sub-Hz level.

6.3.1 Sensitivity of the Mean-Field Model to Detuning

For the data used in the measurements, we estimate the effective detuning from resonance for single shots at several values of ϕ by fitting our mean field model, from Ch. 3, to the spatial profiles, as shown in Fig. 6.7.

Fig. 6.8 shows the sensitivity of the fits to Δ for $\phi = \pi$. Fortunately, drifts in the radiofrequency detuning Δ are partially mitigated by the π pulse at the center of the protocol of Fig. 6.1, which reverses the net accumulated phase at time τ for a fixed detuning. If the detuning is stable over the 400 ms duration of the sequence, this accumulated phase is cancelled. Further, we compensate for the phase shift arising from the magnetic field sweep between B_1 and B_2, as discussed above.

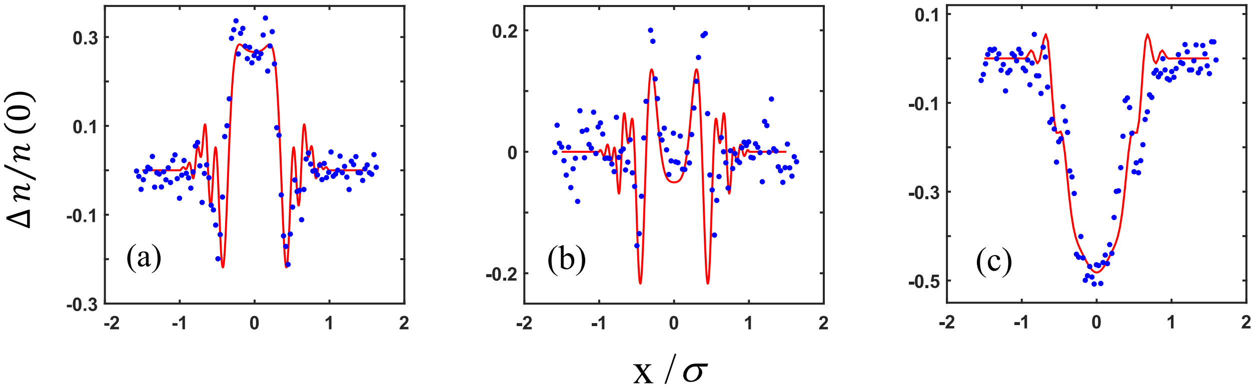

Figure 6.7: Estimating the radiofrequency detuning from the measured single-shot spin density profiles. Here, the spin density $\Delta n = n_\uparrow(x) - n_\downarrow(x)$ is given in units of the central density $n(0)$ and the measured scattering length is $a_{\text{meas}} = 4.24\, a_0$. The single shot data (blue dots) are fit with the mean field model [Pegahan et al., 2019] (red curves), using the detuning Δ as a fit parameter. (a) $\phi = 0.64\,\pi$, $a_{\text{fit}} = 2.35\, a_{\text{meas}}$, $\Delta_{\text{fit}} = 0 \times 2\pi$ rad/s; (b) $\phi = 1.18\,\pi$, $a_{\text{fit}} = 2.5\, a_{\text{meas}}$, $\Delta = 0.1 \times 2\pi$ rad/s; (c) $\phi = 1.63\,\pi$, $a = 2.4\, a_{\text{meas}}$, $\Delta = 0.1 \times 2\pi$ rad/s. Note that the model requires a scattering length that is nominally 2.4 times the measured value to fit the data.

In the following, we discuss the effect of the remaining detuning on the determination of the coherence coefficients from the ϕ-dependent spin density. To understand the effect of finite global detuning Δ on the coherence coefficients, consider the measurement of the z-projection of a single spin $s_{z\alpha i}$ after the pulse sequence, where αi denotes an atom of axial energy E_{xi}. As shown in the Fig. 6.6, for the final state $|\psi_f\rangle$, the OTOC protocol led to

$$\mathcal{F}_{\alpha i}(\phi) \equiv 2\langle\psi_f|s_{z\alpha i}|\psi_f\rangle = 2\,\langle\psi_0|W^\dagger_\phi(\tau)s_{x\alpha i}W_\phi(\tau)|\psi_0\rangle. \tag{6.25}$$

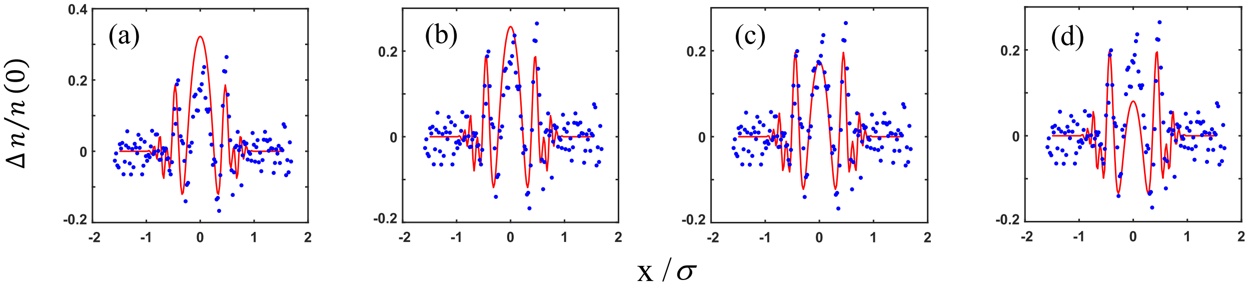

Figure 6.8: Sensitivity of the mean field model to detuning Δ. The blue dots denote data for $\phi = \pi$ and $a_{\text{meas}} = 4.24\,a_0$. The mean field model is evaluated for $\phi = \pi$ and $a_{12} = 2.4\,a_{\text{meas}}$. The detuning in the mean field model (red curves) is varied from 0.17 to 0.47 Hz. (a) $\Delta = 0.17 \times 2\pi$ rad/s; (b) $\Delta = 0.27 \times\ 2\pi$ rad/s; (c) $\Delta = 0.37 \times\ 2\pi$ rad/s; (d) $\Delta = 0.47 \times\ 2\pi$ rad/s.

On the righthand side, $|\psi_0\rangle$ is the fully x-polarized state, obtained after the first $\pi/2$ pulse and W, defined by Eq. 6.14, is

$$W_\phi(\tau) = e^{iH(a)\tau} e^{-i\phi\, S_x} e^{-iH(a)\tau}. \tag{6.26}$$

To explicitly display the detuning dependence of measurement, we write the Zeeman term in Eq. 6.2 as $\Omega_{zi} \rightarrow \Omega_{zi} + \Delta$. Thus, the Hamiltonian in Eq. 6.2 will be

$$H(a,\Delta) \equiv H(a,0) - \Delta\, S_z, \tag{6.27}$$

where $S_z = \sum_{j,\alpha j}^{N} \hat{s}_{z\alpha j}$ is the z-component of the total spin vector. Then, since $[H(a,0), S_z] = 0$, we have

$$W_\phi(\tau) = e^{iH(a,0)\tau}\, e^{-i\Delta\tau\, S_z} e^{-i\phi\, S_x} e^{i\Delta\tau\, S_z} e^{-iH(a,0)\tau} = e^{iH(a,0)\tau} e^{-i\phi\, S_{x'}} e^{-iH(a,0)\tau}. \tag{6.28}$$

Here, the phase shift $\Delta\tau$ is accumulated during the time τ between the first $\pi/2$ pulse and the ϕ rotation in Fig. 6.1. We see that a nonzero detuning changes the axis for the ϕ rotation from x to x', with

$$S_{x'} \equiv e^{-i\Delta\tau S_z} S_x e^{i\Delta\tau S_z} = S_x\, \cos(\Delta\tau) + S_y\, \sin(\Delta\tau). \tag{6.29}$$

Note that the angle between the x' and x axes for a typical single-shot with $\Delta = 0.4$ Hz and $\tau = 0.2$ s is $\Delta\tau \simeq 0.5$ rad.

For each detuning Δ, we can expand Eq. 6.28 for $W_\phi(\tau)$ in a total angular momentum eigenstate basis $|J, M\rangle_{x'}$, with $S_{x'}|J, M\rangle_{x'} = M\,|J, M\rangle_{x'}$, where we suppress all other quantum numbers that define the states, such as intermediate angular momenta. Then, Eq. 6.25, similar to Eq. 6.23, for a single spin in the state α_i can be written as

$$\mathcal{F}_{\alpha_i}(\phi) = 2\sum_m B_m^{(\alpha_i)}\, e^{im\,\phi}, \tag{6.30}$$

where the integer $m = M' - M$ is the difference of the total angular momentum projections along the x' axis, and

$$B_m^{(\alpha_i)} = \sum_{J,J',M} {}_{x'}\langle JM|\hat{\rho}(\tau)|J'M+m\rangle_{x'}\, {}_{x'}\langle J'M+m|s_{x\alpha_i}(\tau)|JM\rangle_{x'}. \tag{6.31}$$

Here, $\hat{\rho}(\tau) = e^{-iH(a,0)\tau}|\psi_0\rangle\langle\psi_0|e^{iH(a,0)\tau}$ is the density operator at time τ and

$$s_{x\alpha_i}(\tau) \equiv e^{-iH(a,0)\tau}\, s_{x\alpha_i}\, e^{iH(a,0)\tau}. \tag{6.32}$$

For $\phi = 0$, using the completeness of the total angular momentum states, we have $2\sum_m B_m^{(\alpha_i)} = 2\,\langle\psi_0|s_{x\alpha_i}|\psi_0\rangle = 1$. Further, $B_{-m}^{(0)} = B_m^{(0)*}$, as required for real $\mathcal{F}_{\alpha_i}(\phi)$.

As shown in figure 6.5, without interactions, $a = 0$, the Hamiltonian reduces to an energy-dependent rotation about the $z-$axis. In this regime, $\hat{s}_{xi}$ is a rank one operator with $m = 0, \pm 1$ only, corresponding to the ϕ-dependent projection of each spin along the x-axis. However, for the interacting system, $a \neq 0$, collisions create coherence between spins with different energies, and hence between states with $|m| = |M' - M| > 1$.

In the experiments, we measure the sum of Eq. 6.30 over atoms with an energy near E, given by Eq. 6.22 and Eq. 6.23, which contain the coefficient

$$B_m = \frac{1}{N_s}\sum_{\alpha_i=1}^{N_s} B_m^{(\alpha_i)}. \tag{6.33}$$

For an average of several shots with varying detunings, as utilized in the experiments to measure the ϕ dependence of the spin density, the expansion coefficients $B_m^{(\alpha_i)}$ of Eq. 6.31 are simply averaged over a range of rotation axes x'. This axis averaging, and the sum over a small range of spin energies near E in Eq. 6.33, will not change the general ϕ-dependent structure of $\mathcal{F}_{\alpha_i}(\phi)$, which enables measurements of the average coherence coefficients, as shown in the Fig. 6.6 and Fig. 6.4.

In summary, energy-resolved measurements of OTOC's in a spin-dependent harmonic trap reveal a coherence structure that is hidden in measurements of the total collective spin vector. Remarkably, the measured ϕ-dependent structure of the energy-dependent collective spin vector is consistent with the predictions of the mean field model of Ch. 3, using the scattering length and the detuning as free parameters. However, we find that the ϕ-dependence predicted using the measured scattering length is much too smooth as shown in Fig. 6.5. In contrast, using the measured scattering length without adjustment, the same model is in close agreement with the complex spatial structure of the spin density profiles $S_z(x)$ observed in single pulse experiments in Ch. 5, which are independent of the detuning. These results suggest that a beyond mean field treatment is needed to correctly predict the observed OTOC measurements. For the measurements presented here, the OTOC was measured as a function of rotation angle ϕ at a fixed time $\tau = 200$ ms. By performing the same measurements for fixed ϕ as a function of τ, it will be possible in future work to study the dynamics of information scrambling by mapping out the OTOC as a function of τ.

The new methods pave the way for microscopic measurements of time-dependent information propagation via observing the build-up of correlations between two particle operators, $V = s_{z\alpha i}\, s_{z\alpha j}$, which I will explain in more detail in Ch. 7.

6.4 Phase-Controlled Radio-Frequency Pulse Calibration

To apply controllable radio-frequency pulses, ϕ_x in the protocol of Fig. 6.1, we use a voltage-controlled phase shifter (RVPT0117MBC as shown in Fig, 6.10), to implement phase shifted RF pulse. This type of phase shifter provides wideband frequency ranging from $70 - 100$ MHz, which matches the range of frequency that we employ for resonant rf transition on the lowest two hyperfine states of ^{6}Li. We calibrated the phase shifter through an RF-mixer circuit, as shown in Fig. 6.9. We filter the higher-order frequency in the mixer's output through a low pass filter and monitor the dependence of applied voltages and phase shift as Fig. 6.10.

As the control voltage of phase shifter changes, 0 to 8 volts, we can extract phase of output signal, 0 to 2π, shifted with respect to the original phase.

To test this calibration method experimentally, one can apply two consecutive $\pi/2$ pulses only to spin $|2\rangle$ of the hyperfine states– in the absence of any spin mixture. If two pulses are phase shifted by 90°, $V = 1.2\ V$ as shown in Fig. 6.9, a balanced population of $|2\rangle$ and $|1\rangle$ should be observed after the second rf pulse. Otherwise, two consecutive $\pi/2$ pulses along the same axes led to a π pulse.

After the calibration, we send a constant voltage of $1.2\ V$ to the phase shifter for the experimental protocol and produce a 90° phase shift, which is ϕ_x pulse for the protocol. We hold the voltage applied to the phase shifter constant throughout the experimental cycles. To cover the whole range of 2π rotation, we change the time duration of ϕ_x from 0, as 0 phase shift, to 2.2 ms, as 2π.

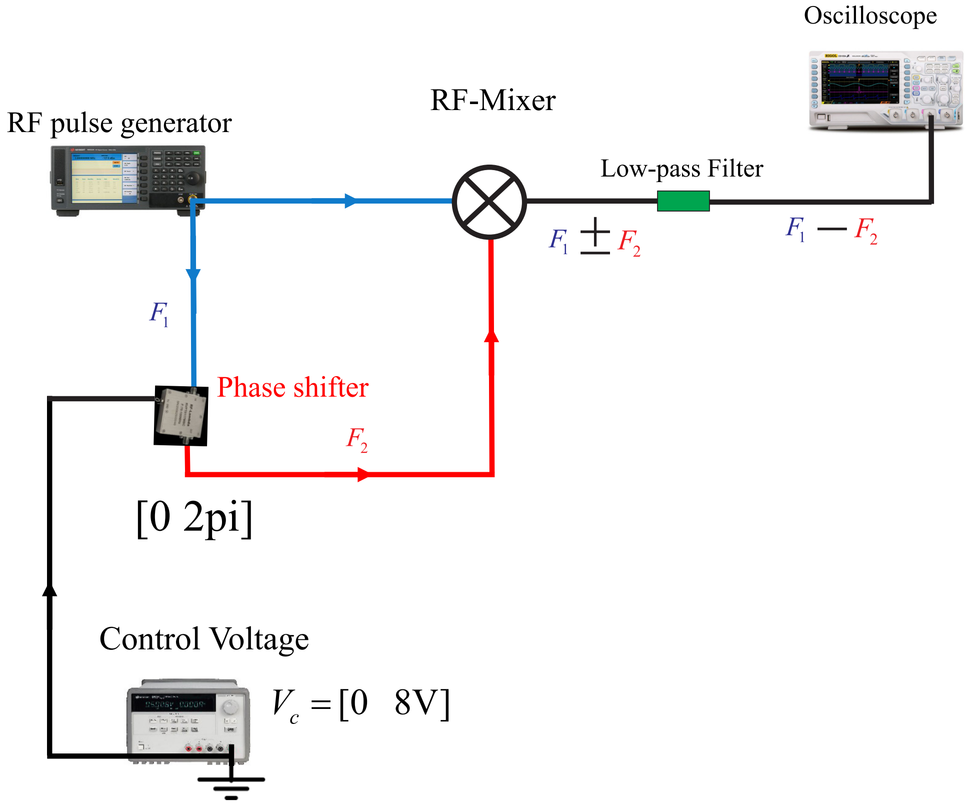

Figure 6.9: Schematic of a radio-frequency mixing circuit. Dashed line shows for what voltages the output signal is shifted by 90°.

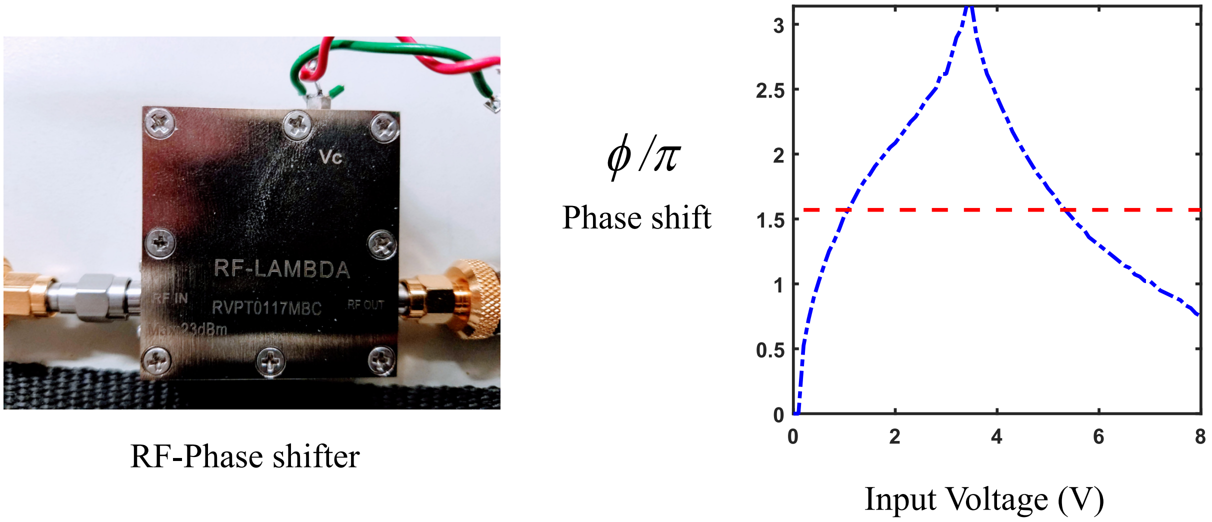

Figure 6.10: (Left) Voltage control phase shifter (RVPT0117MBC) 70 – 100 MHz. (Right) Dependence of phase applied voltage to the phase shifter.

Chapter 7

Conclusion

7.1 Summary of the Dissertation

This dissertation primarily contains two experiments studying spatial spin density, $n_\uparrow(x)$ and $n_\downarrow(x)$, in weakly interacting Fermi gases. First, I provided the detailed derivation of the mean-field model to describe the time evolution of spin-density profiles for coherently prepared two-state Fermi gas of ^{6}Li, confined in a spin-dependent harmonic trap potential, in the collisionless regime. I showed that a one-dimensional mean-field model, without additional simplifying approximations, quantitatively predicts the measured spatial profile structure. These results demonstrated that weakly interacting Fermi gas with conserved single-particle energies enables a simulation of spin-lattice models in energy-space. Using the mean-field model, I determined the zero crossings and magnetic field tuning rates for the s-wave scattering lengths of the three lowest hyperfine states. At high temperatures and small scattering lengths $a < 1$ Bohr, I explained additional features in the spin-density profiles, as shown Fig. 5.14, which was explained by including the energy dependence of the scattering length in our model.

For the second experiment, I demonstrated a general method for performing energy-resolved measurements of a many-body system of trapped atoms in a harmonically trapped weakly-interacting Fermi gas. As previous measurements in this system were limited to the spatial profiles of the collective spin density, I could not observe a higher order spin coherence from the total number of atoms. However, I showed that through an inverse Abel-transformation of the spin density profiles, one can determine the collective energy-resolved spin coherence, enabling general many-body echo protocols. The experimental protocol applies a global rotation, ϕ, to the total interacting spin system in between forward and time-reversed evolution, and measures certain out-of-time order correlation to diagnose the effect of the rotation on spins. I observed quantum coherence and information scrambling through energy-resolved OTOC functions in selected energy partitions. Through these observations, I measured multiple quantum coherence for selected energy partitions.

7.2 Outook

The spin-energy correlation measurements provide an essential benchmark for future work on collective spin evolution with designer energy landscapes in the weakly interacting regime. The experiment pave the way for studies of beyond mean-field physics, measurement of spatially correlated spin fluctuations [Koller et al., 2016], and measurement of correlated spin currents [Bender et al., 2019].

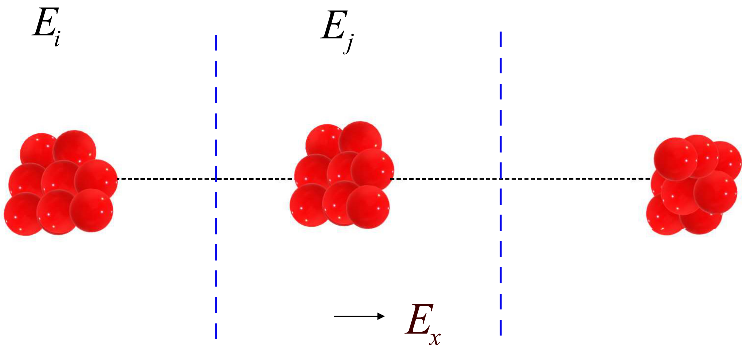

Figure 7.1: One dimensional energy-space lattice. Each energy sector demonstrates atoms in the i^{th} harmonic oscillator state. The range of the energy partitions varies from $E = 0$ to $E = E_F$. Each ensemble contains atoms with similar energy.

The ability to access the energy-resolved OTOCs will motivate new cold atom approaches to simulate "out-of-equilibrium" dynamics in spin-lattice systems [Eisert et al., 2015], information propagation by site-resolved measurements [Joshi et al., 2020], and "fast scrambling" [Bentsen et al., 2019]. For example, the energy-resolved method presented in this dissertation enables observation of time-dependent correlations between collective atoms in different energy-space sectors, as shown in Fig. 7.1,

$$\langle s_{zi} s_{zj} \rangle - \langle s_{zi} \rangle \langle s_{zj} \rangle . \tag{7.1}$$

Eq. 7.1 is an extension of the demonstrated OTOC protocol of Ch. 6, to two-particle operators $s_{zi} s_{zj}$. We plan to measure the correlation between atoms with different energies and possibly measure time-dependent decay of out-of-time-order correlation function, which provides useful information about the effective loss of quantum information [Swingle, 2018], i.e., the scrambling time. We can extend our experiment to a two-dimensional pancake harmonic oscillator potentials and study time-dependent growth of OTOC functions in the energy-lattice.

REFERENCES

[Jul,] P. S. Julienne, private communication.

[Sup,] See Supplemental Material at http://link.aps.org/supplemental/ for details on lattice calibrations, theoretical model of dimer binding in a superlattice, and its numerical implementation, which includes Refs. [Jo et al., 2012].

[Abramowitz et al., 1988] Abramowitz, M., Stegun, I. A., and Romer, R. H. (1988). Handbook of mathematical functions with formulas, graphs, and mathematical tables.

[Bartenstein et al., 2005] Bartenstein, M., Altmeyer, A., Riedl, S., Geursen, R., Jochim, S., Chin, C., Denschlag, J. H., Grimm, R., Simoni, A., Tiesinga, E., et al. (2005). Precise determination of li 6 cold collision parameters by radio-frequency spectroscopy on weakly bound molecules. *Physical review letters*, 94(10):103201.

[Baum et al., 1985] Baum, J., Munowitz, M., Garroway, A. N., and Pines, A. (1985). Multiple-quantum dynamics in solid state NMR. *The Journal of Chemical Physics*, 83(5):2015–2025.

[Bender et al., 2019] Bender, S. A., Kamra, A., Belzig, W., and Duine, R. A. (2019). Spin current cross-correlations as a probe of magnon coherence. *Phys. Rev. Lett.*, 122:187701.

[Bentsen et al., 2019] Bentsen, G., Hashizume, T., Buyskikh, A. S., Davis, E. J., Daley, A. J., Gubser, S. S., and Schleier-Smith, M. (2019). Treelike interactions and fast scrambling with cold atoms. *Phys. Rev. Lett.*, 123:130601.

[Berger, 1996] Berger, L. (1996). Emission of spin waves by a magnetic multilayer traversed by a current. *Physical Review B*, 54(13):9353.

[Bloch, 2012] Bloch, I., D. J. . N. S. (2012). Quantum simulations with ultracold quantum gases. *Nature Physics*, 8(4):267–276.

[Deutsch et al., 2010] Deutsch, C., Ramirez-Martinez, F., Lacroûte, C., Reinhard, F., Schneider, T., Fuchs, J. N., Piéchon, F., Laloë, F., Reichel, J., and Rosenbusch, P. (2010). Spin self-rephasing and very long coherence times in a trapped atomic ensemble. *Phys. Rev. Lett.*, 105:020401.

[Du et al., 2008] Du, X., Luo, L., Clancy, B., and Thomas, J. (2008). Observation of anomalous spin segregation in a trapped fermi gas. *Physical review letters*, 101(15):150401.

[Du et al., 2009] Du, X., Zhang, Y., Petricka, J., and Thomas, J. (2009). Controlling spin current in a trapped fermi gas. *Physical review letters*, 103(1):010401.

[Eisert et al., 2015] Eisert, J., Friesdorf, M., and Gogolin, C. (2015). Quantum many-body systems out of equilibrium. *Nature Physics*, 11(2):124–130.

[Elliott et al., 2014] Elliott, E., Joseph, J. A., and Thomas, J. E. (2014). Anomalous minimum in the shear viscosity of a Fermi gas. *Phys. Rev. Lett.*, 113:020406.

[Elliott, 2014] Elliott, E. R. (2014). *Quantum Transport and Scale Invariance inExpanding Fermi Gases*. PhD thesis, Duke.

[Gärttner et al., 2017] Gärttner, M., Bohnet, J. G., Safavi-Naini, A., Wall, M. L., Bollinger, J. J., and Rey, A. M. (2017). Measuring out-of-time-order correlations and multiple quantum spectra in a trapped-ion quantum magnet. *Nature Physics*, 13:781.

[Gärttner et al., 2018] Gärttner, M., Hauke, P., and Rey, A. M. (2018). Relating out-of-time-order correlations to entanglement via multiple-quantum coherences. *Phys. Rev. Lett.*, 120:040402.

[Gehm, 2003] Gehm, M. E. (2003). *Preparation of an Optically-trapped Degenerate Fermi gas of* ^{6}*Li: Finding the Route to Degeneracy*. PhD thesis, Duke University.

[Gehm et al., 2003] Gehm, M. E., Hemmer, S. L., O'Hara, K. M., and Thomas, J. E. (2003). Unitarity-limited elastic collision rate in a harmonically trapped Fermi gas. *Phys. Rev. A*, 68:011603.

[Griffths, 2005] Griffths, D. J. (2005). *Introduction to Quantum Mechanics.* Pearson Prentice Hall, UpperSaddle River, NJ, 2nd edition.

[Jo et al., 2012] Jo, G.-B., Guzman, J., Thomas, C. K., Hosur, P., Vishwanath, A., and Stamper-Kurn, D. M. (2012). Ultracold atoms in a tunable optical kagome lattice. *Phys. Rev. Lett.*, 108:045305.

[Joshi et al., 2020] Joshi, M. K., Elben, A., Vermersch, B., Brydges, T., Maier, C., Zoller, P., Blatt, R., and Roos, C. F. (2020). Quantum information scrambling in a trapped-ion quantum simulator with tunable range interactions. *Phys. Rev. Lett.*, 124:240505.

[Kinast, 2006] Kinast, J. M. (2006). *Thermodynamics and superfluidity of astrongly interacting fermi gas.* PhD thesis, Duke.

[Köhl et al., 2005] Köhl, M., Moritz, H., Stöferle, T., Günter, K., and Esslinger, T. (2005). Fermionic atoms in a three dimensional optical lattice: Observing fermi surfaces, dynamics, and interactions. *Physical review letters*, 94(8):080403.

[Koller et al., 2016] Koller, A. P., Wall, M. L., Mundinger, J., and Rey, A. M. (2016). Dynamics of interacting fermions in spin-dependent potentials. *Physical Review Letters*, 117(19):195302.

[Ku et al., 2012] Ku, M., Sommer, A. T., Cheuk, L. W., and Zwierlein, M. W. (2012). Revealing the superfluid lambda transition in the universal thermodynamics of a unitary Fermi gas. *Science*, 335:563.

[Landsman et al., 2019] Landsman, K. A., Figgatt, C., Schuster, T., Linke, N. M., Yoshida, B., Yao, N. Y., and Monroe, C. (2019). Verified quantum information scrambling. *Nature*, 567(7746):61–65.

[Lewandowski et al., 2002] Lewandowski, H., Harber, D., Whitaker, D., and Cornell, E. A. (2002). Observation of anomalous spin-state segregation in a trapped ultracold vapor. *Physical review letters*, 88(7):070403.

[Lewis-Swan et al., 2019] Lewis-Swan, R. J., Safavi-Naini, A., Bollinger, J. J., and Rey, A. M. (2019). Unifying scrambling, thermalization and entanglement through measurement of fidelity out-of-time-order correlators in the Dicke model. *Nature Communications*, 10:5007.

[Luo, 2008] Luo, L. (2008). *Entropy and superfluid critical parametersof a strongly interacting fermi gas.* PhD thesis, Duke.

[Marino and Rey, 2019] Marino, J. and Rey, A. M. (2019). Cavity-qed simulator of slow and fast scrambling. *Phys. Rev. A*, 99.

[Mudiyanselage, 2019] Mudiyanselage, J. C. B. K. (2019). *Atom Pairing in Optical Superlattices.* North Carolina State University.

[Natu and Mueller, 2009] Natu, S. S. and Mueller, E. J. (2009). Anomalous spin segregation in a weakly interacting two-component Fermi gas. *Phys. Rev. A*, 79:051601.

[O'Hara et al., 2002] O'Hara, K. M., Hemmer, S. L., Gehm, M. E., Granade, S. R., and Thomas, J. E. (2002). Observation of a strongly interacting degenerate Fermi gas of atoms. *Science*, 298:2179.

[Ong, 2015] Ong, W. C. (2015). *Spin Imbalanced Quasi-Two Dimensional Fermi Gases.* PhD thesis, Duke University.

[Pegahan et al., 2020] Pegahan, S., Arakelyan, I., and Thomas, J. (2020). Energy-resolved information scrambling in a weakly-interacting fermi gas. *arXiv preprint arXiv:2009.02361.*

[Pegahan et al., 2019] Pegahan, S., Kangara, J., Arakelyan, I., and Thomas, J. E. (2019). Spin-energy correlation in degenerate weakly interacting fermi gases. *Physical Review A*, 99(6):063620.

[Piéchon et al., 2009] Piéchon, F., Fuchs, J. N., and Laloë, F. (2009). Cumulative identical spin rotation effects in collisionless trapped atomic gases. *Phys. Rev. Lett.*, page 215301.

[Pretzier, 1991] Pretzier, G. (1991). A new method for numerical Abel-inversion. *Zeitschrift fÃ¼r Naturforschung A*, 46(7):639 – 641.

[Sakurai, 1994] Sakurai, J. J. (1994). *Modern Quantum Mechanics.* Addison-Wesley, New York.

[Schleier-Smith, 2017] Schleier-Smith, M. (2017). Probing information scrambling. *Nature Physics*, 13:724–726.

[Slonczewski et al., 1996] Slonczewski, J. C. et al. (1996). Current-driven excitation of magnetic multilayers. *Journal of Magnetism and Magnetic Materials*, 159(1):L1.

[Smale et al., 2019] Smale, S., He, P., Olsen, B. A., Jackson, K. G., Sharum, H., Trotzky, S., Marino, J., Rey, A. M., and Thywissen, J. H. (2019). Observation of a transition between dynamical phases in a quantum degenerate Fermi gas. *Science Advances*, 5(8). elocation-id: eaax1568.

[Swingle, 2018] Swingle, B. (2018). Unscrambling the physics of out-of-time-order correlators. *Nature Physics*, 14(10):988–990.

[Swingle and Yao, 2017] Swingle, B. and Yao, N. Y. (2017). Seeing scrambled spins. *Physics*, 10:82.

[Wall, 2020] Wall, M. L. (2020). Simulating fermions in spin-dependent potentials with spin models on an energy lattice. *arXiv preprint arXiv:2001.04615.*

[Wiese et al., 1966] Wiese, W. L., Smith, M. W., Glennon, and M., B. (1966). *Atomic Transition Probabilities, National Standard Reference Data Series.* National Bureau of Standards 4.

[Zettili, 2009] Zettili, N. (2009). *Quantum mechanics: concepts and applications.* Wiley, Chichester, U.K, 2nd edition.

[Zhang et al., 2004] Zhang, J., van Kempen, E. G. M., Bourdel, T., Khaykovich, L., Cubizolles, J., Chevy, F., Teichmann, M., Tarruell, L., Kokkelmans, S. J. J. M. F., and Salomon, C. (2004). $p-$wave Feshbach resonances of ultracold ^{6}Li. *Phys. Rev. A*, 70:030702.

[Zhang, 2013] Zhang, Y. (2013). *Radio Frequency Spectroscopy Of a Quasi-Two-Dimensional Fermi Gas*. PhD thesis, Citeseer.

[Zürn et al., 2013] Zürn, G., Lompe, T., Wenz, A. N., Jochim, S., Julienne, P. S., and Hutson, J. M. (2013). Precise Characterization of 6Li Feshbach Resonances Using Trap-Sideband-Resolved RF Spectroscopy of Weakly Bound Molecules. *Phys. Rev. Lett.*, 110(13):135301.

[Zürn et al., 2013] Zürn, G., Lompe, T., Wenz, A. N., Jochim, S., Julienne, P. S., and Hutson, J. M. (2013). Precise characterization of ^{6}Li Feshbach resonances using trap-sideband-resolved rf spectroscopy of weakly bound molecules. *Phys. Rev. Lett.*, 110:135301.

[Zwierlein et al., 2005] Zwierlein, M. W., Abo-Shaeer, J. R., Schirotzek, A., Schunck, C. H., and Ketterle, W. (2005). Vortices and superfluidity in a strongly interacting fermi gas. *Nature*, 435(7045):1047–1051.

ProQuest LLC
789 East Eisenhower Parkway
P.O. Box 1346
Ann Arbor, MI 48106 - 1346